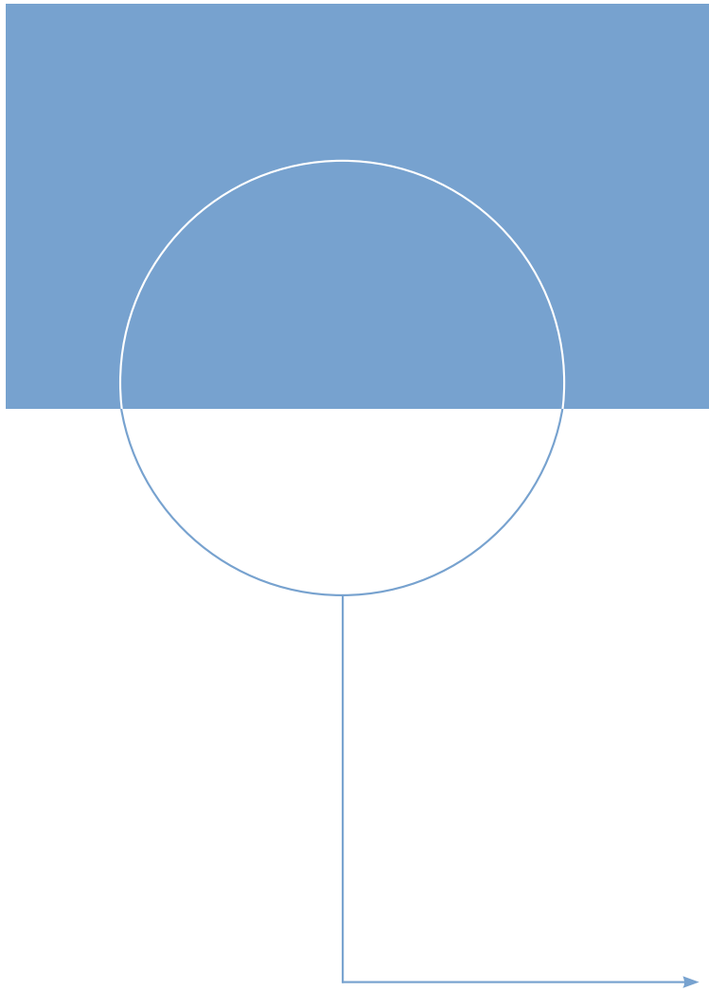

Master's thesis

2019

August Jaros

NTNU
Norwegian University of
Science and Technology
Faculty of Information Technology and Electrical
Engineering
Department of Electric Power Engineering

August Jaros

Parameter identification of Synchronous generator using Standstill Frequency Response (SSFR) test

July 2019

NTNU
Norwegian University of
Science and Technology

NTNU
Norwegian University of
Science and Technology

NTNU

Norwegian University of
Science and Technology

Parameter identification of Synchronous generator using Standstill Frequency Response (SSFR) test

August Jaros

Energy and Environmental Engineering
Submission date: July 2019
Supervisor: Trond Leiv Toftevaag

Norwegian University of Science and Technology
Department of Electric Power Engineering

Problem formulation

This Master's thesis project serves as the starting point for parameter identification of a synchronous machine at the Department of Electrical Power Engineering at NTNU, Trondheim, and acquiring experience in use of Standstill Frequency Response (SSFR) test for identification of synchronous machine parameters. The work is planned to cover tests on the Siemens-Schuckert synchronous machine at the National Smart Grid laboratory at NTNU, and synchronous machines with already known parameter values. The main motivation is connected to planned research activities in the new Research council FME project HydroCen and at Norwegian Hydro-power Centre, and is related to topics like stability studies, synthetic inertia and converter fed operation of synchronous machines.

Due to the Siemens-Schuckert machine's age, it is questioned that conventional testing might risk the safety of the machine. The Standstill Frequency Response (SSFR) test has therefore been chosen as the method to be used in parameter identification of the machine. Validation of the test should first be performed on a synchronous machine with parameters already known. The SSFR-test has as per January 2019 not yet been performed at the Department of Electrical Power Engineering.

Abstract

This Master's thesis serves as the starting point in the work with parameter identification of the Siemens-Schuckert machine at the National Smart Grid laboratory at NTNU in Trondheim, and acquiring experience in use of Standstill Frequency Response (SSFR) test for identification of synchronous machine parameters. The motivation is future collaboration studies between NTNU, HydroCen and SINTEF Energy Research regarding the development of hydropower technology.

The Siemens-Schuckert synchronous machine was tested with the Open-Circuit Characteristic (OCC) test and Short-Circuit Characteristics (SCC) tests. The machine's SCC and OCC was constructed. A retardation test was also conducted to determine the machine's inertia. The inertial time constant was calculated to be $H = 2.67s$.

The Rudolf-Dietze synchronous machine was tested using the SSFR-test in order to validate the test as an alternative to the traditional, but more demanding, sudden short-circuit tests. The SSFR-test attempts to obtain the *operational parameters* of the machine. The operational parameters can be expressed as rational functions in the frequency domain which are related to the *fundamental parameters* that describe the electrical characteristics of the machine. The machine is tested in order to construct the different parameters' frequency responses. Using curve-fitting tools, the rational form operational parameter functions can be obtained. The SSFR-test is the main focus of this thesis.

A laboratory set-up and method of measurement for the SSFR-tests was developed based on available laboratory-instruments. The frequency response of the operational parameters $L_d(s)$, $L_q(s)$ and $G(s)$ was constructed from the SSFR test-results. The oscilloscope used for the measurements was not able to conduct measurements for the required frequency range of 1mHz-1kHz, and measurements below 0.1Hz was omitted from the tests. An estimation method based on the MATLAB System Identification Toolbox was used to estimate the operational parameter expressions. However, due to incomplete test-data, the estimates obtained should be regarded as approximate at best. In order to accurately estimate the complete set of the machine's parameters with this method, accurate SSFR-measurements for the whole range of frequencies are required. Thus, for future SSFR-studies, measurements should be conducted with instruments enabling accurate measurements for the complete frequency range.

Sammendrag

Denne Masteroppgaven utgjør oppstarten av arbeidet med å parameteridentifisere Siemens-Schuckert-synkronmaskinen ved det Nasjonale Smartgridlaboratoriet ved NTNU i Trondheim, samt å øke kompetansen på feltet Stillstands Frekvensresponstesting (SSFR) som verktøy for å identifisere synkronmaskinparametre. Bakgrunnen for oppgaven er samarbeidsstudier mellom NTNU, HydroCen og SINTEF Energi der målet er viderutvikling av vannkraftsteknologi.

Siemens-Schuckert-synkronmaskinen ble testet for å identifisere åpen-klemme-karakteristikken og kortslutningskarakteristikken til maskinen. I tillegg ble det foretatt en utløpstest for å bestemme treghetsmomentet til maskinens rotor. Treghetskonstanten til maskinen ble beregnet til $H = 2.67s$.

Rudolf-Dietze-synkronmaskinen ble SSFR-testet for å validere SSFR-metoden som et tryggere alternativ til den mer tradisjonelle kortslutningstesten. Målet med SSFR-testen er å etablere maskinens *operasjonelle parametre*. Disse kan uttrykkes som rasjonelle funksjoner i frekvensplanet, og er tett knyttet til maskinens *fundamentalparametre*, som er med på å beskrive maskinens elektriske karakteristikker og egenskaper. Maskinen blir testet på en måte som gjør det mulig å konstruere frekvensresponsen til de ulike operasjonelle parameterne. Ved bruk av kurvetilpasningsverktøy kan de rasjonelle utrykkene til maskinens operasjonelle parametrte bestemmes. Denne oppgavens hovedfokus ligger på SSFR-testen.

Et laboratorieoppsett og en målemetode for SSFR-testen ble utviklet med tilgjengelig laboratorieutstyr. Frekvensresponsen til de operasjonelle parameterne $L_d(s)$, $L_q(s)$ og $G(s)$ ble konstruert basert på resultatene fra SSFR-testen. Oscilloskopet brukt for målingene evnet ikke å gjøre målinger for hele det nødvendige frekvensområdet mellom 1mHz-1kHz, og målinger under omtrent 0.1Hz ble derfor utelatt. En kurveestimeringsmetode basert på verktøy i MATLAB sin System Identification Toolbox ble brukt til å estimere de rasjonelle uttrykkene til de operasjonelle parameterne, men grunnet ufullstendige måleresultater må resultatene antas unøyaktige. Mer nøyaktige SSFR-målinger for hele det aktuelle frekvensområdet er nødvendig for mer presis estimering av maskinens parametrte. For fremtidige SSFR-studier bør målingene gjøres med instrumenter som evner nøyaktige målinger over hele det nødvendige frekvensområdet.

Preface

This Master's Thesis is submitted to the Department of Electric Power Engineering at the Norwegian University of Science and Technology (NTNU) and concludes my Master of Science (MSc) degree in Energy and Environmental Engineering.

This Master's thesis project serves as the starting point for parameter identification of a synchronous machine at the Department of Electrical Power Engineering at NTNU, Trondheim, and acquiring experience in use of Standstill Frequency Response (SSFR) test for identification of synchronous machine parameters. The main motivation is connected to planned research activities in the new Research council FME project HydroCen and at Norwegian Hydro-power Centre, and is related to topics like stability studies, synthetic inertia and converter fed operation of synchronous machines.

I wish to thank my supervisor, Trond Leiv Toftevaag, for helpful advice and the occasional nudge in the right direction. I would also like to convey my appreciation to Trond for letting me pursue what I found to be an interesting topic.

A special thanks to staff engineers Bård Almås, Svein Erling Norum and especially senior engineer Vladimir Klubicka for helping me with experiments and to find my way around the laboratory. I also wish to direct my sincere gratitude towards staff engineer Aksel Andreas Reitan Hanssen for helping me, though unsuccessfully, in finding satisfactory measurement tools. You made me realize that my set-up was 'good enough'. A special thanks also goes to Kjell Ljøkelsøy at SINTEF Energy Research for help with operating the big red synchronous machine and for being available at such short notice.

Trondheim, July 2019
August Jaros

Contents

List of symbols

δ	Rotor angle
ω_m	Mechanical rotational speed
ω_r	Rotational speed
Ψ	Air-gap flux
ψ_a, ψ_b, ψ_c	Stator flux-linkages
ψ_d, ψ_q, ψ_0	dq-axis flux-linkages
$\psi_{fd}, \psi_{kd}, \psi_{kq}$	Field-circuit flux-linkages
τ	Time constant
τ_m, τ_e	Mechanical and electromagnetic torques
θ	Rotor position
D_d	Damping torque coefficient
E_a	Internal generated voltage
E_b	Brush voltage drop
e_a, e_b, e_c	Stator phase voltages
e_d, e_q	dq-axis stator voltages
e_{fd}	Field voltage
$G(s)$	Armature-to-field transfer function
H	Inertia constant
I_a	Armature current

i_{1d}, i_{fd} d-axis rotor currents

i_{1q}, i_{2q} q-axis damper winding currents

i_a, i_b, i_c Stator phase currents

i_d, i_q dq-axis stator currents

i_{fd} Field current

i_{kd} d-axis damper winding current

i_{kd} q-axis damper winding current

J Rotor inertia

L_{1d}, L_{fd} d-axis rotor inductances

L_{1q}, L_{2q} q-axis rotor inductances

l_{aa}, l_{bb}, l_{cc} Self-inductances of stator windings

l_{ab}, l_{bc}, l_{ca} Mutual inductances between stator windings

$L_{afd}, L_{akd}, L_{akq}$ Constant mutual-inductances between stator and rotor windings

$l_{afd}, l_{akd}, l_{akq}$ Mutual inductances between stator and rotor windings

L_{al} Leakage inductance

L'_d, L''_d d-axis transient and subtransient inductances

$L_d(s)$ d-axis operational inductance

L_d, L_q dq-axis synchronous reactances

$L_{ffd}, L_{kkd}, L_{kkq}$ Constant self-inductances of rotor windings

$l_{ffd}, l_{kkd}, l_{kkq}$ Self-inductances of rotor windings

L_l Leakage inductance

L'_q, L''_q q-axis transient and subtransient inductances

$L_q(s)$ q-axis operational inductance

P_m, P_e Shaft power and air-gap power

R_{1d}, R_{fd} d-axis rotor resistances

R_{1q}, R_{2q} q-axis rotor resistances

R_a Per phase armature winding resistance

R_{fd} Field winding resistance

R_{kd}, R_{kq} Damper windinq resistances

S Apparent power

T Net torque

T_0 Idling torque

T'_{d0} d-axis open-circuit transient time-constant

T''_{d0} d-axis open-circuit subtransient time-constant

T'_d d-axis short-circuit transient time-constant

T''_d d-axis short-circuit subtransient time-constant

T_{ind} Induced torque

T'_{q0} q-axis open-circuit transient time-constant

T''_{q0} q-axis open-circuit subtransient time-constant

T'_q q-axis short-circuit transient time-constant

T''_q q-axis short-circuit subtransient time-constant

V_a Terminal voltage

$Z_{afo}(s)$ Armature-to-field transfer impedance

$Z_d(s)$ d-axis operational impedance

$Z_q(s)$ q-axis operational impedance

Acronyms

d-axis Direct axis.

EMT Electromagnetic Transients.

MUT Machine Under Test.

OCC Open-Circuit Characteristic.

q-axis Quadrature axis.

SCC Short-Circuit Characteristic.

SSFR Standstill Frequency Response.

Chapter 1

Introduction

In recent years, the development of intermittent renewable technologies such as wind and solar power, has seen a considerable increase as the world's energy system undergoes a transition towards a greener and more sustainable energy future [1, 2]. This development introduces new challenges for the electric grids around the world. Traditionally large synchronous machines were the main drivers of the electric grid, contributing to a predictable and reliable generation of power. However, with the rapidly increasing penetration of renewables in the grid, and the relatively unpredictable nature of its power generation, new requirements for already existing energy services are set [2]. Increased fluctuations in the power supply will require more flexible energy sources and storage solutions, and technology that provides the necessary stability requirements for safe and reliable grid operation [1, 2, 3]. One such technology is hydropower [2].

Today, hydropower is regarded as an enabling technology for the increased penetration of renewables in the grid, its potential role as a supplier of both flexible power generation and storage, in addition to grid stability support being the main arguments [2]. As one of the leading hydropower nations in the world, Norway is therefore in a unique position to contribute to the transition towards more renewable energy production and a greener, more sustainable future [2]. As part of the Research Council of Norway's FME-package, the Norwegian Research Centre for Hydropower Technology (HydroCen), together with NTNU and SINTEF Energy Research, forms a research platform from which to develop hydropower technology further and strengthen Norway's position as a hydropower nation [4].

In the National Smart Grid Laboratory at NTNU in Trondheim, a Siemens-Schuckert motor-generator set exists which is to be used be used in collaboration studies between NTNU, HydroCen and SINTEF Energy Research with regards to development of hydropower technologies. Research objectives include stability studies, synthetic inertia and converter fed operation of synchronous machines [5, 6]. As of January 2019, a complete electric model of the 75kVA Siemens-Schuckert synchronous machine does not exist however. Parameter identification of this machine, in the context of enabling the machine to be used in further studies, is the main motivation for this thesis.

1.1 Objectives

Traditionally, the sudden short-circuit test has been the main form of machine testing, both providing a way of validating a machine's ability to withstand the mechanical stresses that arise during short-circuiting, in addition to determining both synchronous and transient machine characteristics [7]. The machine in question is old however, and together with laboratory personnel, supervisor and representatives from Karsten Moholt AS, the company that performed maintenance on the machine in 2016, it was discussed whether the machine might be able to withstand the stresses associated with conventional short circuit testing or not [8, 9]. In order to ensure the structural integrity of the machine, it was decided that another method of testing would be needed in order to fully determine the machine parameters. One such method is the Standstill Frequency Response (SSFR) test [7], and is the main topic of this thesis.

The SSFR-test aims to obtain the *operational parameters* of the Machine Under Test (MUT)[10, 7]. The operational parameters $L_d(s)$, $L_q(s)$ and $G(s)$ are transfer functions that help describe a two-port representation of the MUT [10]. The parameters can both be related to the observable behaviour of the machine, as viewed from its terminals under appropriate test conditions, and to the *fundamental parameters* of the machine, i.e the parameters the completely describe the electrical characteristics of the machine [10]. The parameters thus serve as a link between testing the machine and obtaining the electrical characteristics that describe its behaviour.

As of January 2019, SSFR-tests have not yet been performed at the Department of Electric Power Engineering [8]. In order to gain practical experience with the tests, and to validate the test methods, it was decided that the tests should be performed on a synchronous machine with parameters already known. The 8kVA Rudulf-Dietze machine, which was tested and parameter-identified in a master's thesis from 2017 [11], is such a machine, and was chosen as the machine to be tested with SSFR-tests in this thesis.

The objectives of this thesis can thus be summarized as follows:

- Initiate parameter identification of the 75kVA Siemens-Shuckert machine by conducting basic synchronous machine tests.
- Parameter identification using SSFR-tests on a synchronous machine with known parameters. The synchronous machine in question is the 8kVA Rudolf-Dietze machine which was parameter identified in a master's thesis from 2017. This is considered as the thesis' main objective, and most of the pages in this thesis are dedicated to the study of these tests.
- Provide a foundation from which to strengthen the competence of SSFR-testing at the Department of Electrical Power Engineering.

1.2 Scope of work

Based on the objective stated above, the scope of this thesis include the following:

- Literature study of synchronous machines and synchronous machine testing, including SSFR-testing.
- Conducting basic tests on the Siemens-Schuckert synchronous machine. This includes tests to obtain the Open-Circuit Characteristic (OCC), the Short-Circuit Characteristic (SCC) in addition to determining the inherent rotational inertia of the machine's rotor.
- Development of a laboratory test set-up for the SSFR-tests with available laboratory instruments.
- Development of SSFR-test procedure.
- Conducting SSFR-tests on the Rudolf-Dietze machine with the goal of identifying the operational parameters of the machine.

1.3 Limitations

This thesis is limited to consider only the test results from the relevant tests. No subsequent actions are taken on behalf of the obtained test results, i.e no further attempt at using the obtained test results in calculations for further parameter identification is made. For the SSFR-tests for example, this includes not using the operational parameters to derive the fundamental parameters of the machine. In addition, acquirement of any equipment needed was not considered due to the time allotted for the thesis work. This means that available equipment already at NTNU had to be used for the tests conducted in this thesis.

1.4 Software

The software tools used in this thesis are all based on toolboxes from the MATLAB product range. The toolboxes used are the System Identification Toolbox, for estimating transfer functions based on SSFR-measurement data, and the Curve Fitting Toolbox. Also, a custom made function from the Mathworks community File Exchange was used to create asymptotic approximations of bode plots [12].

1.5 Report structure

The structure of this thesis diverge somewhat from what is usually seen in theses containing laboratory work. Generally, the structure used for the such theses include chapters that

separately contain information about laboratory equipment used, measurement methodology, results and discussion. In this thesis however, all this information is compiled in such a way as to compress relevant information together, and is meant to create a structure that is easily digestible for the reader. The complete report structure is summarized below:

Part I - Theoretical foundations

Chapter 1 - *Introduction*: Provides background and motivation for the thesis work and an overview of objectives, limitations, software used and report structure.

Chapter 2 - *Synchronous machine modelling*: Outlines the fundamental modelling of salient pole synchronous machines and describes the set of parameters that completely describe the electrical characteristics of such machines, termed *fundamental parameters*.

Chapter 3 - *Machine test procedures*: Describes the test procedures of the short-circuit characteristic test, open-circuit characteristic test and the retardation test used to test the Siemens-Schuckert machine.

Chapter 4 - *Standstill frequency response (SSFR) test*: Outlines the theoretical foundation for SSFR-testing in addition to describing the test procedure including instrumentation and measurement set-ups.

Chapter 5 - *Presentation of machines to be tested*: Presents the two machines tested in this thesis, including nameplate and other relevant electrical characteristics.

Part II - Laboratory work, results and analysis

Chapter 6 - *Test results for Siemens-Schuckert machine*: Presentation of instrumentation, methodology and results from the tests conducted on the Siemens-Schuckert machine.

Chapter 7 - *SSFR measurement set-up and test procedure*: Introduction to the developed test set-up and measurement procedure to be used for the SSFR-tests. Includes a brief presentation of the development process.

Chapter 8 - *SSFR-test results and analysis*: Presentation of the SSFR-tests conducted on the Rudolf-Dietze machine, including measurement results, data-processing and a basic curve-fitting procedure used to identify the parameters of the machine. Where appropriate, analysis of test results are provided.

Chapter 9 - *Concluding remarks*: Summary of the conclusions made based on the test results. Includes a commentary on recommendations for further work.

Part I

Theoretical foundations

The theoretical foundation required to understand, interpret and appreciate the laboratory work and results obtained in this thesis, is founded in part I of this thesis. This part is divided into four chapters.

Chapter 2 contains fundamental modelling of salient pole synchronous machines and describes the set of parameters that completely describe the electrical characteristics of such machines, termed *fundamental parameters*. The relation these parameters have to the *operational parameters* of the machine during tests is also described. A brief introduction to inertia and stability is also included.

Chapter 3 describes the test procedures of the short-circuit characteristic test and the open-circuit characteristic test as described in the IEEE-test guide for synchronous machines [7]. The test procedure for the retardation test and how to calculate inertia based on the results from this test is also provided.

Chapter 4 contains the theoretical foundation for SSFR-testing in addition to describing the test procedure. This includes instrumentation and measurement set-ups.

Chapter 5 describes the two machines tested in this thesis, including nameplate and other relevant electrical characteristics.

Chapter 2

Synchronous machine modelling

2.1 Mathematical description of the synchronous machine

The classic, 'lumped circuit' model of a synchronous machine is well known and illustrated in figure 2.1. It consists of three stator windings, a, b and c, and three rotor circuits. Two rotor circuits, the field winding and one amortisseur winding, are placed in the rotor Direct axis (d-axis), while one damper winding is placed in the Quadrature axis (q-axis) [13, 10]. Electrical quantities associated with the field and damper windings are denoted f and k, while subscripts d and q denotes the relevant axis. It should be noted that several such rotor circuits may be present in a synchronous machine [10]. However, for the purposes of this analysis only three rotor circuits are assumed.

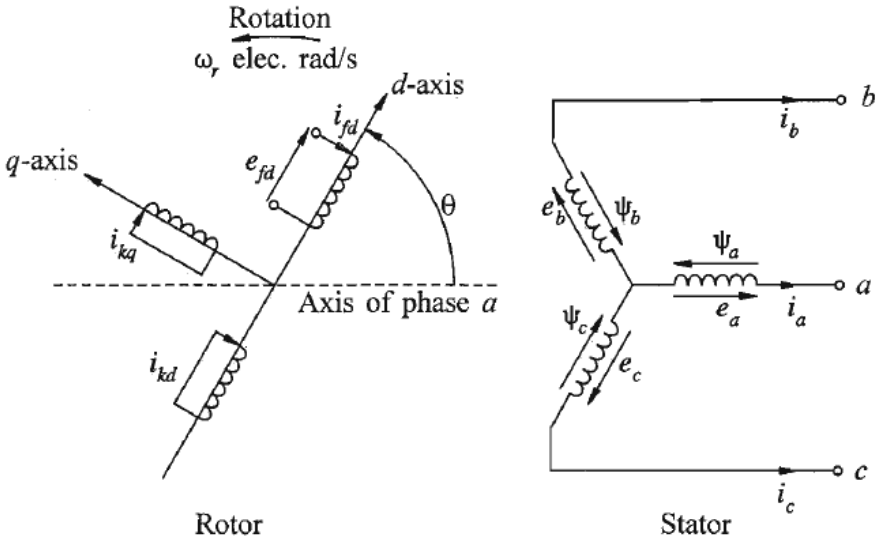

Figure 2.1: Schematic illustration of the 'lumped circuit' model of a synchronous machine [10]. The stator circuits consists of three windings that produce induced voltages and currents, electrically displaced by 120°. The rotor circuits contain two damper windings, one in each axis, and one field winding in line with the d-axis.

In a rotating machine, the magnetic flux produced by the rotor field penetrates the stator coils and an emf is induced. The voltage equations describing the relationship between rotor and stator coils are described below [10]:

Stator voltage equations:

$$e_a = \frac{d\psi_a}{dt} - i_a R_a \tag{2.1}$$

$$e_b = \frac{d\psi_b}{dt} - i_b R_b \tag{2.2}$$

$$e_c = \frac{d\psi_c}{dt} - i_c R_c \tag{2.3}$$

Rotor voltage equations:

$$e_{fd} = \frac{d\psi_{fd}}{dt} + i_{fd} R_{fd} \tag{2.4}$$

$$0 = \frac{d\psi_{kd}}{dt} - i_{kd} dR_{kd} \tag{2.5}$$

$$0 = \frac{d\psi_{kq}}{dt} - i_{kq} R_{kq} \tag{2.6}$$

Here, e are the phase or field voltages, i are the circuit currents and R is the circuit resistances. The flux linkages, denoted by ψ, describe the flux linking between the coils in stator and rotor. Each of the different linkages are expressed as a product of the current and the mutual inductance between the two linked coils [10]. In equation 2.7 below, the flux linkage of stator phase a is expressed in such a way, with l_{aa} being the phase a self-inductance, while l_{ab}, l_{ac}, l_{afd}, l_{akd} and l_{akq} is the mutual inductance between the phase a winding and phases b, c, field and damper windings respectively. The notation being used can be seen in the List of symbols. Note that the expression below can be made for phase b and c also.

$$\psi_a = -l_{aa} i_a - l_{ab} i_b - l_{ac} i_c + l_{afd} i_{fd} + l_{akd} i_{kd} + l_{akq} i_{kq} \tag{2.7}$$

The machine equations described above are further complicated due to the positional reliance of the self- and mutual inductances in the machine. In a salient pole synchronous machine, which is considered in this thesis, the airgap in which the flux passes through, varies along the machine's circumference [10]. This is shown in figure 2.2. The airgap is narrowest in the d-axis and largest in the q-axis, affecting the total permeance of the flux-path taken by the stator-flux at each new position of the rotor. Thus all self- and mutual inductances in equation 2.7 above can be described as a function of permeance, or rotor position [10, 13]. An example of this is shown in equation 2.2 below, where the self-inductance of phase a is a sum of the leakage flux, L_{al} and the expression for the positional dependent self-inductance

$L_{g0} + L_{aa2}cos(2\theta)$. Here θ is the rotor position.

$$l_{aa} = L_{al}L_{g0} + L_{aa2}\cos(2\theta) \tag{2.8}$$

For the sake of this thesis, it is only relevant to know the reliance these inductances have on rotor position. The complete mathematical description of the inductances in equation 2.7, and in the corresponding equations for phase b and c, are therefore neglected in this thesis. For sake of reference, these expressions can be found in [10] and [13].

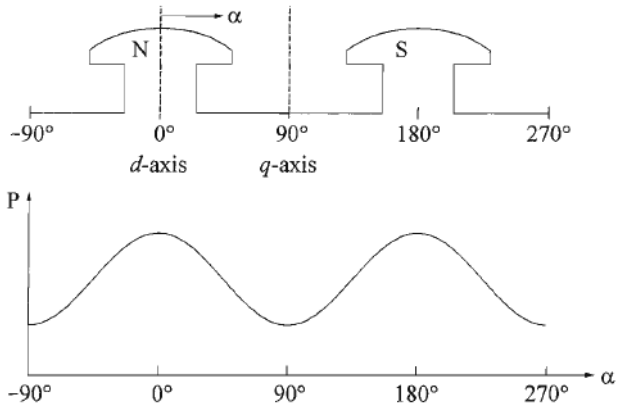

Figure 2.2: Permeance as a function of rotor position in a salient pole synchronous machine [10]

.

2.2 Park transformation and the dq-system

In order to simplify the above equations, the Park transformation is used. The Park transform is a mathematical transformation performed to express both rotor and stator quantities in a rotating reference frame, aligned to the d- and q-axes of the rotor [13]. With the transform, a fictitious model of the synchronous generator can be made, where all machine circuits can be represented as lumped and aligned to the two rotor axes, rotating with the rotor [13]. This is illustrated in figure and implies that all inductances, associated with the different dq-windings, are constant [10, 13]. The Park transform matrix, in this case ued to transform the stator currents from abc- to dq-coordinates, is stated in equation 2.9 below:

$$\begin{bmatrix} i_d \\ i_q \\ i_0 \end{bmatrix} = \frac{2}{3} \begin{bmatrix} \cos(\theta) & \cos(\theta - \frac{2\pi}{3}) & \cos(\theta + \frac{2\pi}{3}) \\ -\sin(\theta) & -\sin(\theta - \frac{2\pi}{3}) & -\sin(\theta + \frac{2\pi}{3}) \\ \frac{1}{2} & \frac{1}{2} & \frac{1}{2} \end{bmatrix} \begin{bmatrix} i_a \\ i_b \\ i_c \end{bmatrix} \tag{2.9}$$

Consequently, the flux linkage equations for the stator, as shown in equation 2.7, can be rewritten as a function of constant inductances. This is shown in equations 2.10, 2.11 and 2.12 below:

$$\psi_d = -L_d i_d + L_{afd} i_{fd} + L_{akd} i_{kd} \tag{2.10}$$

$$\psi_q = -L_q i_q + L_{akq} i_{kq} \tag{2.11}$$

$$\psi_0 = -L_0 i_0 \tag{2.12}$$

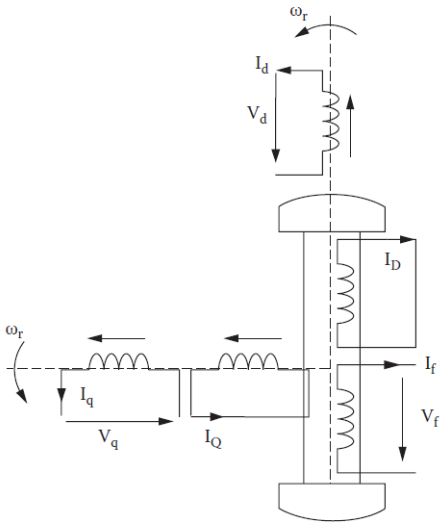

Figure 2.3: dq-representation of a salient pole synchronous machine [13].

The inductances L_d, L_q, L_{afd}, L_{akd}, L_{akq} and L_0 are a combination of constant inductance values that originate from the positional dependent inductance equations, such as equation 2.8. The point here is not to show where all the different inductance values originate from, but rather to show that machine modelling and analysis becomes considerably easier with the equations expressed with constant inductance values [10]. It is left up to the reader to find these relationships if needed. The relationships are expressed in [10] and [13].

Using the above transform, as well as the dq-model flux linkages, the stator voltage equations for the machine can be rewritten as follows:

Stator voltage equations in dq-components

$$e_d = \frac{d\psi_d}{dt} - \psi_q \omega_r - R_a i_d \tag{2.13}$$

$$e_q = \frac{d\psi_q}{dt} - \psi_d \omega_r - R_a i_q \tag{2.14}$$

$$e_0 = \frac{d\psi_0}{dt} - R_a i_0 \tag{2.15}$$

The same exercise can be made for the rotor equations, however the rotor voltage equations stay the same as in equations 2.4, 2.5 and 2.6 . The flux linkages in dq-components are instead expressed as in equations 2.16, 2.17 and 2.18.

$$\psi_{fd} = L_{ffd} i_{fd} + L_{fkd} i_{kd} - \frac{3}{2} L_{afd} i_d \tag{2.16}$$

$$\psi_{kd} = L_{fkd} i_{fd} + L_{kkd} i_{kd} - \frac{3}{2} L_{akd} i_d \tag{2.17}$$

$$\psi_{kq} = L_{kkq} i_{kq} - \frac{3}{2} L_{akq} i_q \tag{2.18}$$

2.3 Equivalent circuits

Based on the stator and rotor voltage equations describes in the previous section, d- and q-axis equivalent circuits can be constructed. For this analysis, the equivalent circuits for a machine with two rotor circuits in both axes are considered. The d-axis contains one field-circuit and one damper winding, while two damper windings are present in the q-axis. The complete set of voltage and flux-linkage equations for constructing the equivalent circuits are presented in Appendix A

It should be noted that the following equations presented in Appendix A, and hence the equivalent circuits presented below, are in per unit values. It is not the objective of this thesis to explain the relationships or the calculation of base values used for the per unit system used in this analysis, and it is left up to the reader to discover these relationships if necessary. The base values chosen for the per unit system is the same as used in [10]. For the purposes of this thesis however, it is only necessary to know that the correct choice for base values implies the following assumptions:

- Per unit mutual inductances between windings are reciprocal, for example: $L_{afd} = L_{fda}$.
- Per unit mutual inductances between stator and rotor circuits in each axis are equal. For example: $L_{afd} = L_{akd}$.

In addition, the two self-inductances L_d and L_q are assumed equal to the sum of the leakage inductance L_l, due to flux not linking any of the rotor circuits, and the mutual inductance L_a, linking the rotor circuits. Then:

$$L_d = L_l + L_{ad}, \qquad L_q = L_l + L_{aq} \tag{2.19}$$

The d- and q-axis equivalent circuits are illustrated in figure 2.4 and figure 2.5 respectively. Thus, a complete model describing the characteristics of a synchronous machine is developed. It should be noted that in the literature, it is very common to neglect the series inductance $L_{fld} - L_{ad}$ in the d-axis rotor circuit [10]. Also, it is normal practice to simplify the equivalent circuits by neglecting the stator circuits [10].

The parameters, i.e resistances and inductances, expressed in the equivalent circuits below completely describe the electrical characteristics of the machine [10]. They are termed *fundamental parameters* for future reference in this thesis.

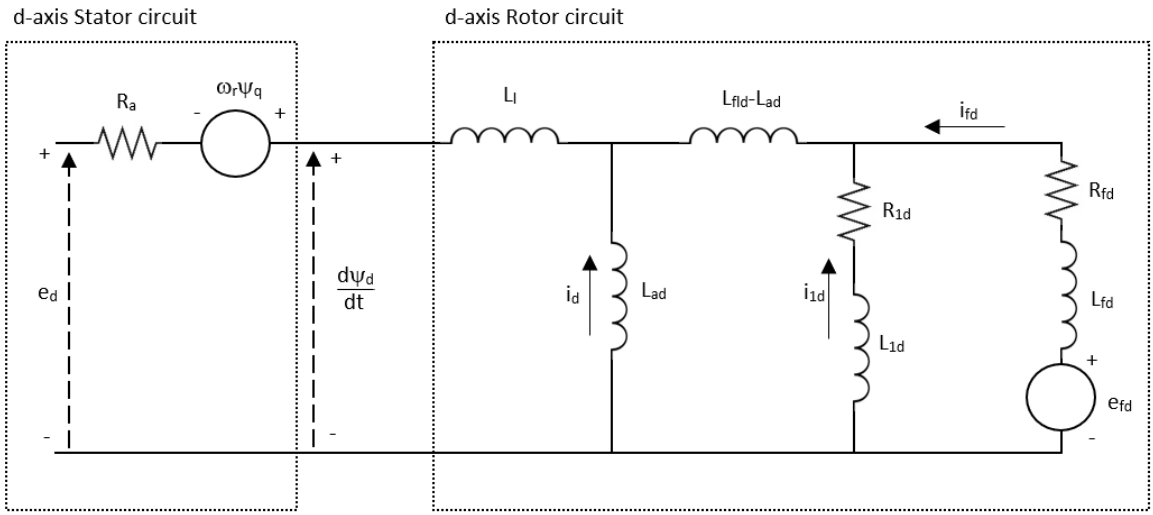

Figure 2.4: d-axis equivalent circuit. Adapted from [10].

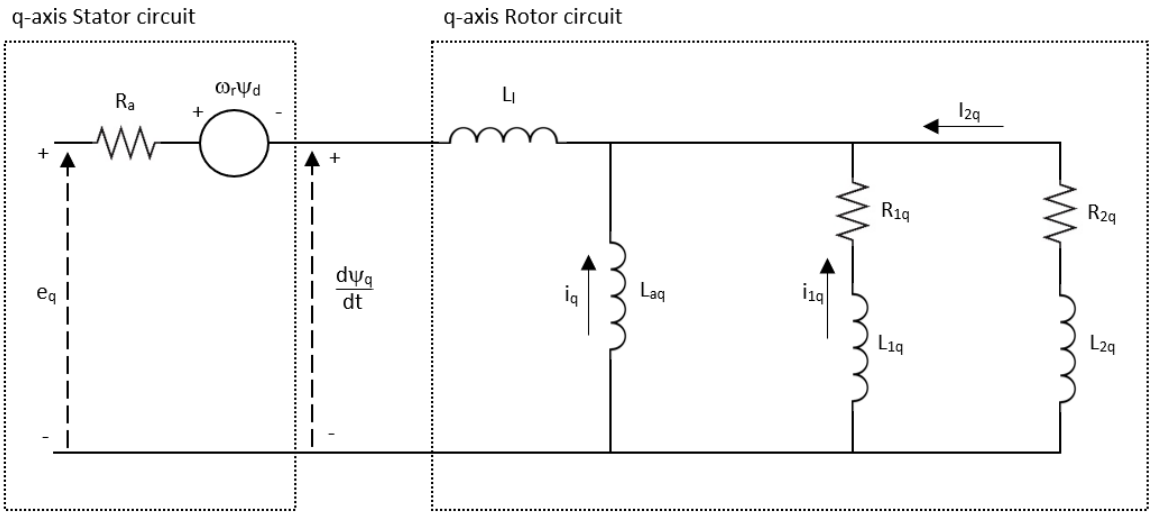

Figure 2.5: q-axis equivalent circuit. Adapted from [10].

2.4 Operational parameters

Even though the complete electrical characteristics of a synchronous machine can be described by the fundamental parameters presented in the previous section, these parameters can not readily be determined from machine testing [10]. In order to be able to determine the machine's electrical characteristics, a different set of parameters are developed that can be related to the observed behaviour of the machine during testing. These parameters are called *operational parameters* [10].

Conceptually, the operational parameters can be determined from the machine's observable behaviour during testing, while at the same time being related to the fundamental parameters of the machine [10]. This way, by determining the operational parameters, the fundamental parameters can be obtained.

The operational parameters can be represented as transfer functions that relate the behaviour between the rotor and stator terminals when the machine is considered a two port network [10]. This is illustrated in figure 2.6. The idea is that, when the machine circuits are considered a black box, a set of parameters can still describe the responsive nature of the machine.

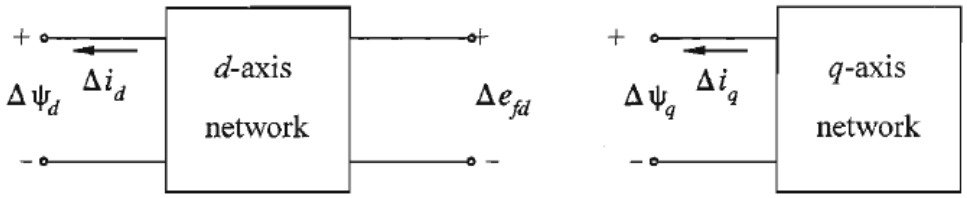

Figure 2.6: The machine represented by a two-port network i the d- and q-axis respectively.

For a synchronous machine, the common way of representing the incremental relationship between the field and armature terminal quantities is shown in equation 2.20 and 2.21. Here, ψ is the armature flux linkages, e_{fd} is the field voltage and i_d and i_q is the d- and q-axis armature currents respectfully. 's' is the Laplace operator.

$$\Delta\psi_d(s) = G(s)\Delta e_{fd}(s) - L_d(s)\Delta i_d(s) \tag{2.20}$$

$$\Delta\psi_q(s) = -L_q(s)\Delta i_q(s) \tag{2.21}$$

The three operational parameters $L_d(s)$, $L_q(s)$ and $G(s)$ can be described as follows:

G(s) is the armature to field transfer function. It is the Laplace transform of the ratio between d-axis armature flux linkages and the field voltage, with the armature open circuited [10].

$\mathbf{L_d(s)}$ is the d-axis operational inductance. It is the Laplace transform of the ratio between d-axis armature flux linkages and the d-axis current, with the field winding short circuited[10].

$\mathbf{L_q(s)}$ is the q-axis operational inductance. It is the Laplace transform of the ratio between the q-axis armature flux linkages and the q-axis current[10].

The expressions for the operational parameters can be obtained by considering the circuit-equivalents in figure 2.4 and 2.5, but is a mathematically demanding exercise. In order not to clutter these pages with an unnecessary amount of equations, the derivation of the d-axis operational parameters $L_d(s)$ and $G(s)$ are referred to Appendix B. The resulting expressions, both for d- and the q-axis, are shown below:

$$L_d(s) = L_d \frac{1 + (T_4 + T_5)s + T_4 T_6 s^2}{1 + (T_1 + T_2)s + T_1 T_3^2} \tag{2.22}$$

$$L_q(s) = L_q \frac{1 + (T_4 + T_5)s + T_4 T_6 s^2}{1 + (T_1 + T_2)s + T_1 T_3^2} \tag{2.23}$$

$$G(s) = G_0 \frac{(1 + sT_{kd})}{1 + (T_1 + T_2)s + T_1 T_3 s^2} \tag{2.24}$$

where

$$G_0 = \frac{L_{ad}}{R_{fd}} \qquad T_{kd} = \frac{L_{1d}}{R_{1d}}$$

$$T_1 = \frac{L_{ad} + L_{fd}}{R_{fd}} \qquad T_2 = \frac{L_{ad} + L_{1d}}{R_{1d}}$$

$$T_3 = \frac{1}{R_{1d}}\Big(L_{1d} + \frac{L_{ad}L_{fd}}{L_{ad} + L_{fd}}\Big) \qquad T_4 = \frac{1}{R_{fd}}\Big(L_{fd} + \frac{L_{ad}L_l}{L_{ad} + L_l}\Big)$$

$$T_5 = \frac{1}{R_{1d}}\Big(L_{1d} + \frac{L_{ad}L_l}{L_{ad} + L_l}\Big) \qquad T_6 = \frac{1}{R_{1d}}\Big(L_{1d} + \frac{L_{ad}L_{fd}L_l}{L_{ad}L_l + L_{ad}L_{fd} + L_{fd}L_l}\Big)$$

It should be noted that the expressions are derived with the two-rotor circuit-model as derived in section 2.3. The operational parameters can be extended to any number of rotor circuits, however the two-rotor circuit model is usually considered adequate [10].

For the $L_q(s)$-expression, the time constants can be written exactly as presented above, but but changing the damper and field annotations with the second and first damper circuit annotations respectively. For example, all *fd*-annotations change to *1q*, and all *1d*-annotations become *2q* [10]. For future reference, it is ssumed that all expressions involving d-axis quantities, also have a q-axis counterpart, but with the annotations changed as described here.

In the literature, it is more common to express the equations for $L_d(s)$, $L_q(s)$ and $G(s)$ in factored form [10], as shown in the equations below.

$$L_d(s) = L_d \frac{(1+sT'_d)(1+sT''_d)}{(1+sT'_{d0})(1+sT''_{d0})} \tag{2.25}$$

$$L_q(s) = L_q \frac{(1+sT'_q)(1+sT''_q)}{(1+sT'_{q0})(1+sT''_{q0})} \tag{2.26}$$

$$G(s) = G_0 \frac{(1+sT_{kd})}{(1+sT'_{d0})(1+sT''_{d0})} \tag{2.27}$$

The relationship between time constants in equation 2.22, 2.23 and 2.24 and in the equations below can be determined by way of comparing the numerators and denominators of the relevant operational parameter. The classical way of portraying the time constants is by simplification [10]. Knowing that R_{1d} is much larger than R_{fd} leads to T_1 being much larger than T_2 and T_3, and T_4 being much larger than T_5 and T_6. This leads to the following, approximate relationship between the time constants:

$$T'_{d0} \approx T_1 \qquad T''_{d0} \approx T_3 \qquad T'_d \approx T_4 \qquad T''_d \approx T_6 \tag{2.28}$$

The same time constants exist for the q-axis [10]. Also, the $G(s)$ time constant T_{kd} is as described in the previous section. For more accurate relationships, refer to [10].

A comment should be made that the goal here is not to confuse the reader with a lot of equations and a fair amount of subscripted quantities, but rather to show that the factored form time constants derived above are related to the fundamental parameters of the machine. In the next section, the operational parameters' relation to the transient behaviour of synchronous machines are investigated.

2.5 Transient parameters

One of the advantages of expressing the operational parameters in the factored form is that they can describe the machine's performance during transient conditions, as seen from the generator terminals [10]. During a disturbances, currents are induced in the rotor circuits of the machine, where the different rotor currents decay at different rates [10]. The fastest decaying components are called *subtransient* components, while slower decaying components are called *transient* components. Similarly to the decaying current components, machine parameters that affect the most rapidly decaying components are called *subtransient parameters*, those that affect the slower decaying components are called *transient parameters*, and those parameters

that influence the steady-state components are called *synchronous parameters* [10].

The time constants that govern these rates are the same as presented in equation 2.25, 2.26 and 2.27 [10]. Consider the incremental form of the d- and q-axis flux linkages in equation 2.20 and 2.21 with the expressions for the operational parameters as shown below.

$$\Delta\psi_d(s) = G_0\frac{(1+sT_{kd})}{(1+sT'_{d0})(1+sT''_{d0})}\Delta e_{fd}(s) - L_d\frac{(1+sT'_d)(1+sT''_d)}{(1+sT'_{d0})(1+sT''_{d0})}\Delta i_d(s) \tag{2.29}$$

$$\Delta\psi_q(s) = -L_q\frac{(1+sT'_q)(1+sT''_q)}{(1+sT'_{q0})(1+sT''_{q0})}\Delta i_q(s) \tag{2.30}$$

With the stator terminals open ($\Delta i_d = 0$), and applying a change to the field terminals, the d-axis stator flux, and hence the terminal voltage, experiences a change where the rate of change is governed by the two time-constants $T'_{d0} = T_4$ and $T''_{d0} = T_6$ [10]. Due to the large differences in the field and damper resistances, T''_{d0} is much smaller than T_{d0}. Thus, T''_{d0} governs the rapid changes and is termed the *d-axis open-circuit subtransient time constant*, while T'_{d0} governs the less rapids changes and is therefore termed the *d-axis open-circuit transient time constant* [10].

The same exercise can be done for the d-axis when short circuiting the field ($\Delta e_{fd} = 0$), leading to the *d-axis short-circuit subtransient time constant*, T''_d, and the *d-axis short-circuit transient time constant*, T'_d. The q-axis constants can be derived in the same way [10].

Also the transient and subtransient inductances are of interest when considering a machine's transient behaviour [10]. These are the inductances as seen from the terminals of the machine during transient or subtransient conditions. Synchronous inductances are associated with the steady-state operation of the machine.

The synchronous inductance can be derived using the steady-state condition $s = 0$, while the subtransient inductance is found using the subtransient condition $s = \infty$. Thus:

$$L_d(0) = L_d \qquad\qquad L''_d = L_d(\infty) = L_d\Big(\frac{T'_dT''_d}{T'_{d0}T''_{d0}}\Big) \tag{2.31}$$

For the transient inductance, the transient condition can be seen as neglecting the effect of the d-axis damper winding. This yields:

$$L'_d = L_d(\infty) = L_d\Big(\frac{T'_d}{T'_{d0}}\Big) \tag{2.32}$$

The same exercise can be done for the q-axis inductances.

The important thing to note from these derivations is that the operational parameters of the machine can be derived from the synchronous and transient behaviour of the machine, as measured from the machine's terminals. In extension of this, the fundamental parameters of the machine can be derived. The Standstill Frequency Response test (SSFR-test) is a test that attempts to derive the operational parameters through machine testing. This form of testing is discussed further in Chapter 4.

2.6 Equations of motion, inertia and stability

The rotor dynamics of a synchronous machine is governed by the so called *swing equation* [10] and is presented in equation 2.33 below.

$$J\frac{d^2\delta_m}{dt^2} + D_d\frac{d\delta_m}{dt} = \tau_m - \tau_e \tag{2.33}$$

The equation relates swings in the rotor angle δ to disturbances in the grid [10]. As seen from the equation, the rotor angle is balanced as long as the electromagnetic torque, τ_e, and the mechanical torque produced by the prime mover of the machine, τ_m, are equal. The electromagnetic torque is the torque produced by the electromagnetic forces in the machine due, and oppose the mechanical torque [14]. D_d is the damping torque coefficient and accounts for the mechanical rotational loss due to windage and friction, while J is the total rotor inertia [15].

The swing equation can also be written in terms of electromagnetic and mechanical power, as expressed in equation 2.34.

$$J\omega_m\frac{d^2\delta_m}{dt^2} + D_d\omega_m\frac{d\delta_m}{dt} = P_m - P_e \tag{2.34}$$

Here, ω_m is the mechanical rotational speed, while P_m and P_e is the net shaft power and the electric air-gap power respectively [15]. The rotor angle can also be expressed in terms of rotational speed, and thus relate either power or torque imbalances to changes in rotor speed [15].

$$\omega_m = \omega_{sm} + \frac{d\delta_m}{dt} \tag{2.35}$$

It is also common practice to express the inertia of the rotor mass in terms of an inertia constant, H [15]. As shown in equation 2.36, the inertia constant H is expressed as the stored energy at synchronous speed, divided by the machine rating, S. The inertia constant unit is seconds, and can be interpreted as the amount of kinetic energy stored in the rotor at synchronous speed in terms of the number of seconds it would take the generator to provide

an equivalent amount of electrical energy when operating at a power output equal to its MVA rating [15].

$$H = \frac{1}{2}\frac{J\omega_m^2}{S} \tag{2.36}$$

The equations above are important when analysing power system stability [14]. Power system stability may be defined as the ability of a power system to remain in a state of operating equilibrium under normal operating conditions, and to maintain and regain this state after being subject to disturbances [10]. This usually refers to the ability of the synchronous machines in a power system to maintain synchronism during both small and large disturbances. The nature of disturbances that affect synchronism, that is the rotor angle or the rotor speed of machines, range from small disturbances, such as load changes, to larger more severe disturbances in the form of short-circuits, disconnection of large loads or generators or loss of transmission lines [10]. Stability studies of these disturbances and how they are affected by the synchronous machine equations above are termed *small signal stability* and *transient signal stability* respectively.

Small signal stability depends on the machine' ability to maintain their operation without severe changes to the rotor angle during small disturbances [10]. Transient stability concerns itself with large disturbances that cause large changes to rotor angle position. It is normal that post-fault conditions after such a fault may be different to the operating condition prior to the fault[10]. For such faults, ancillary stability services are initiated in order to keep the system stable [10, 15]. The role of the individual machines are therefore usually to maintain the rotor angle long enough for other services to take over [15].

Consider the equations above. The two factors that affect the change in rotor angle position are the damping torque coefficient, D_d and the rotor inertia, J. For example, as seen from the equation, during an unbalance in the torques τ_m and τ_e, the magnitude of J determines the rate of change of the rotor angle: A larger inertia leads to a slower retardation of the rotor speed. The point to note here is that the inertia and damping torque affects the change in rotor position due to disturbances, and are therefore important to determine for stability studies of synchronous machines.

Chapter 3

Machine test procedures

In order to determine the performance characteristics of a synchronous machines it is necessary to conduct tests to identify the parameters and relations describing a machine's operating capabilities. These tests cover a wide range of conditions and characteristics including resistance measurements, saturation tests, losses and efficiency, torque and synchronous and transient parameters of the MUT [7]. An IEEE-guide has been developed for standardizing the accepted tests for determining the performance characteristics of synchronous machines. This guide is mainly used for the tests conducted in this thesis. The guide is primarily made with focus on testing synchronous generators, but can however also be used to test synchronous motors, synchronous condensers and synchronous frequency changers [7].

The following sections presents the test procedures used to test the Siemens-Schuckert synchronous machine. The tests involve the Open-Circuit Characteristic (OCC) test, the Short-Circuit Characteristic (SCC) test, and the retardation test used to determine the machine's inherent rotational inertia.

The Standstill Frequency Response (SSFR) test procedure, used to test the Rudolf-Dietze machine, is covered in Chapter 4.

3.1 Open-Circuit Characteristic test

The Open-Circuit Characteristic test is used to construct the OCC of the machine. The OCC is a curve of the open-circuit terminal voltage, V_{oc}, as a function of the armature field current, I_f. The resulting curve, an example of which is illustrated in figure 3.1, is used to determine the saturation characteristics of the machine [10]. When the field current is increased, the iron saturates and the reluctance in the core-iron is increased dramatically. Thus, the magnetic flux, or the internal generated voltage, increases much more slowly for increasing field current [16], leading to the curved behaviour observed for higher field currents. The air-gap line is the relationship between terminal voltage and field current if no saturation occurs [16].

The open-circuit test is performed by measuring the open-circuit armature terminal voltages for increasing field current when the machine is operated at no-load and at rated speed [7].

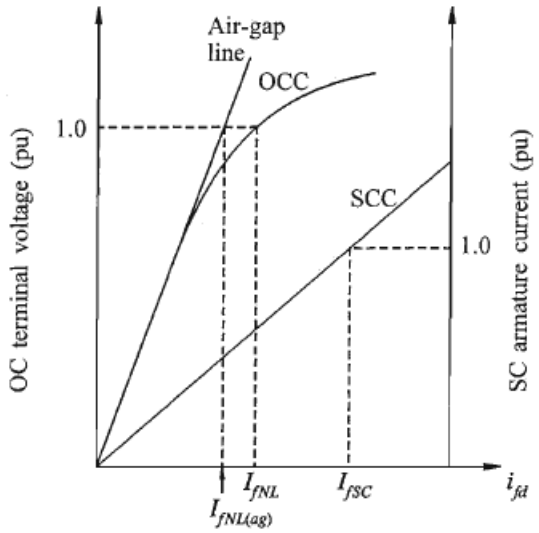

Figure 3.1: Caption

Since the machine terminals are open-circuited, no current flows, and the terminal open-circuit voltage, V_{oc} is equal to the internal generated voltage, E_a [16]. The IEEE-guide recommends the following readings to be taken [7]:

- Six readings should be taken below 60% of rated voltage. One of these readings should be at zero excitation.
- Between 60% and 110% of rated voltage, at least 10 readings should be taken approximately of every 5% increment in terminal voltage.
- Above 110% of rated voltage, at least two readings should be taken. One should be taken at approximately 120% of rated voltage, or at the maximum voltage recommended by the machine's manufacturer.

All readings should be taken with increasing excitation. If the field current must be reduced for whatever reason, the field current should be reduced to zero and then slowy increased to the desired value in order to negate the effect of hysteresis [7].

The observed air-gap line can be obtained by extending the low-field-current linear part of the OCC beyond the point from which the machine begins to saturate. If the low-field-current region of the OCC is non-linear, the air-gap line can be constructed tangent to the OCC at the origin [7].

3.2 Short-Circuit Characteristic test

The Short-Circuit Characteristic test is used to construct the Short-Circuit Characteristic (SCC) of the machine. The SCC is the relationship between short-circuit armature current

I_{sc} and the armature field current, I_f, as illustrated in figure 3.1. It is used, together with the OCC, to determine the *saturated* and *unsaturated* synchronous reactance of the machine. In addition, it can be used to measure the short-circuit losses as well as the stray-load losses of the machine [7].

The SCC is obtained by measuring the short-circuit currents on a three-phase short circuited armature for increasing field current. The machine should be run at rated speed. The short-circuit current should be measured at 125%, 100%, 75%, 50%, 25% and 0% of the rated current, starting with the highest excitation. This is to keep the temperature in the machine nearly constant during the test [7]. The maximum test current value of 125% is normally provided by the manufacturer as the machine should not be operated at above 100% without risking damage to the machine [7].

3.3 Retardation test and determination of rotor inertia

The rotor inertia of a machine can be determined by a number of methods used in the literature, where some tests even require the removal of the rotor from the machine [17]. In the context of this thesis and the machine involved, it was deemed unpractical to attempt separation of the rotor from the rest of the machine. One common experimental method for determining rotor inertia, that does not require any separation between rotor and machine, is the retardation test [17].

The retardation test is performed by rotating the machine's rotor at no-load, above rated speed, before removing the prime mover, subsequently letting the rotor decelerate until stand-still [17]. During this period, power is dissipated due to friction and windage, gradually slowing down the machine. A typical retardation curve for an electrical machine is illustrated in figure 3.2.

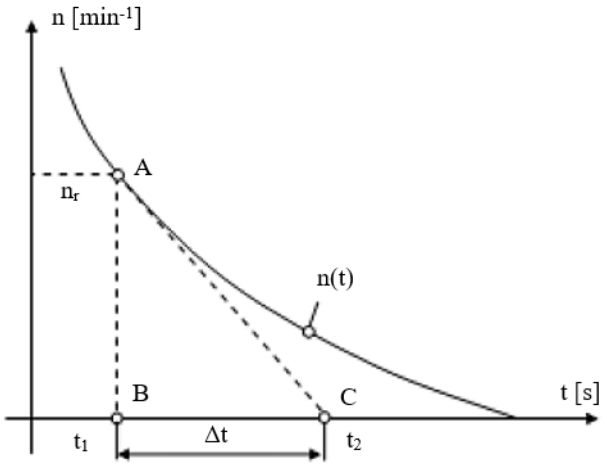

Figure 3.2: Typical deceleration curve for a rotor decelerating from above-rated speed [17].

This curve can be described by the motion equation for free body rotation[15], also known as the swing equation. This equation is shown in equation 3.3 below:

$$J\frac{d\omega_m}{dt} + D_d\omega = T \tag{3.1}$$

Here, J is the total rotor inertia, ω_m is the mechanical speed in rad/s, T is the net torque on the rotor shaft and D_d is the damping-torque coefficient which accounts for rotational losses due to friction and windage [15]. At constant speed, the derivative term $\frac{d\omega_m}{dt} = 0$. This yields:

$$D_d\omega = T_0 \tag{3.2}$$

T_0 is the idling torque associated with driving the rotor shaft when the machine is operated at no-load. Thus, the friction and windage "torque" is equal to the no-load torque of the machine run at constant speed. Consider then a machine operated at constant speed and no-load which is suddenly disconnected from its prime mover. The acting torque on the rotor shaft is zero, leading to the following differential equation.

$$J\frac{d\omega_m}{dt} = -D_d\omega \tag{3.3}$$

Solving the above equation with the initial condition $\omega(t = 0) = w_0$ yields the following equation for the deceleration curve:

$$\omega = \omega_0\, e^{-\tau t}\ , \qquad \tau = \frac{J}{D_d} \tag{3.4}$$

Thus, in order to calculate the rotor inertia, both the time constant of the deceleration curve and the damping torque must be found. The time constant is defined as the time it takes for the speed to reach $\frac{1}{e}$ of the initial value [18], which can be extracted from the deceleration curve.

Chapter 4

Standstill Frequency Response test

The SSFR-test aims to obtain the transfer functions of the operational parameters $L_d(s)$, $L_q(s)$ and $G(s)$. By exciting the the armature terminals of the machine, and observing the response in either stator or field windings, different relationships between voltages and currents in the stator and field can be developed. These test results can further be used in order to derive the operational parameters, which in turn is needed to derive the complete model of the machine [19]. This chapter examines the theoretical background for SSFR tests in addition to the methodical approach to SSFR-testing, test set-ups and instrumentation as recommended by the IEEE-test guide [7] and other literature.

4.1 Theoretical background of SSFR-testing

The theoretical foundation that SSFR-testing rests upon is frequency response characteristics of the operational parameters of the MUT. Consider the parameter $L_d(s)$ from equation 2.25 and the accompanying asymptotic approximation of its magnitude plot in figure 4.1. As illustrated, the corner points of the asymptotic plot is governed by the open- and short circuit time constants of $L_d(s)$ as well as the magnitude of both synchronous, transient and subtransient inductance values, L_d, L'_d and L''_d respectively. The general shape of the plot shown in figure 4.1, in addition to the shapes of both $L_q(s)$ and $G(s)$, is applicable to all synchronous machines. This also applies to the characteristic phase plots of the operational parameters [10]. The conceptual idea of SSFR-testing is thus that if these frequency response characteristics can be constructed through experimental measurements, analytic methods and tools can be applied in order to derive the characteristic parameters of the MUT [7].

The conceptual approach, as described in [20], is summarized in short below:

Step 1 SSFR-test process. Measurement data from SSFR-tests are obtained, and used to construct the frequency response characteristics of the operational parameters.

Step 2 Analysis procedure. The complete transfer functions of $L_d(s)$, $L_q(s)$ and $G(s)$ are obtained using analytic methods and curve-fitting tools.

Step 3 Derivation of the complete machine model. The fundamental parameters are derived from the operational parameters.

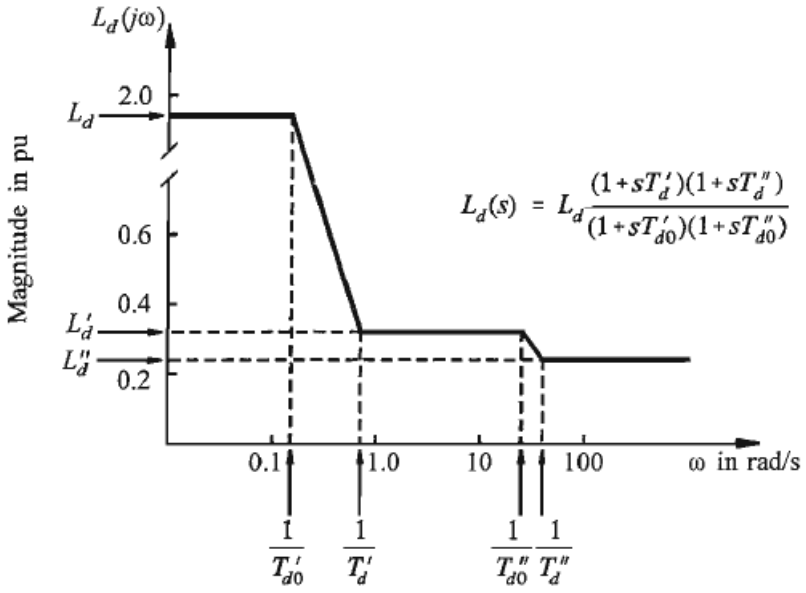

Figure 4.1: Asymptotic approximation of the magnitude plot of $L_d(s)$ [10].

4.2 Methodical approach to SSFR-testing

The following sub-sections describes the general SSFR-test procedure, as outlined in the IEEE-guide for test procedures of synchronous machines [7], in addition to discussing different aspects of the test-setup. This includes instrumentation, required measurement accuracy and factors that may affect the test results. A brief comment is also made on the analytic part of the test procedure, and on which approaches that has been used in the literature.

4.2.1 Measurable quantities

In order to obtain the frequency response characteristics of the operational parameters, the following quantities are measured:

$$Z_d(s) = \left.\frac{\Delta e_d(s)}{\Delta i_d(s)}\right|_{\Delta e_{fd}=0} \tag{4.1}$$

$$Z_q(s) = -\frac{\Delta e_q(s)}{\Delta i_q(s)} \tag{4.2}$$

$$G(s) = \left.\frac{\Delta e_d(s)}{s\Delta e_{fd}(s)}\right|_{\Delta i_d=0} \tag{4.3}$$

From the above equations, each of the operational parameters can be derived. $Z_d(s)$ and $Z_q(s)$ indicate the operational *impedances* as seen from the generator terminals. The operational *inductances* can be derived from these by subtracting the armature resistances, as shown in equation 4.4 and 4.5 below.

$$L_d(s) = \frac{Z_d(s) - R_a}{s} \tag{4.4}$$

$$L_q(s) = \frac{Z_q(s) - R_a}{s} \tag{4.5}$$

An alternative to measuring $G(s)$, and which is generally preferred to measuring of $G(s)$, is to measure small changes in the field and armature currents when the field winding is shorted [19, 21]. This is shown in equation 4.6

$$sG(s) = \left.\frac{\Delta i_{fd}(s)}{s\Delta i_d(s)}\right|_{\Delta e_{fd}=0} \tag{4.6}$$

Also, the armature to field transfer impedance, Z_{afo} is usually measured, as shown in equation 4.7.

$$Z_{afo}(s) = \left.\frac{\Delta e_{fd}(s)}{s\Delta i_{fd}(s)}\right|_{\Delta i_{fd}=0} \tag{4.7}$$

A brief note on the notation used in the above equations: The vertical bar to the right of some of the expressions, and accompanying subscript, indicate the physical connection of the stator or field during the test. $\Delta e_{fd} = 0$ indicates that the field is shorted under test, while $\Delta i_{fd} = 0$ indicates an open field connection [7]. This is also indicated in the test setup schematics, which is presented in section 4.2.3.

4.2.2 Test procedure

As previously discussed, the objective of the SSFR test is to construct the frequency response characteristic plots of the operational parameters, that is phase and magnitude plots, over a wide range of frequencies [7]. Thus, tests are performed for each of the measurable quantities, $Z_d(s)$, $Z_q(s)$, $G(s)$ or $sG(s)$ as well as $Z_{afo}(s)$.

Conceptually, each test is performed by exciting the generator terminals with a current and measuring the response in either stator or field, dependent on what parameter is being measured. From the measured response, the magnitude and phase difference can be calculated, and a point on the frequency response characteristic plot is constructed. This process is then repeated while adjusting the frequency of the exciting current between each measurement. The tests should be performed for frequencies between approximately three times the rated frequency of the MUT and down to around 1mHz, with at least 10 logarithmically spaced measurement points per decade of frequency [7]. Measurement accuracy is discussed in section 4.2.5. Eventually the measurements results in the construction of a magnitude and phase plot as a function of frequency. A typical result of such a test is illustrated in figure 4.2.

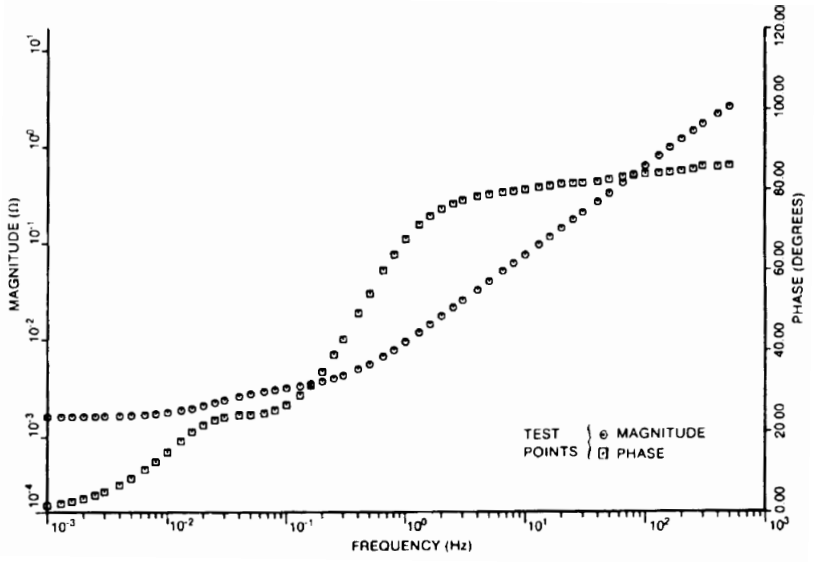

Figure 4.2: Typical frequency response test result. The schematic illustrates the frequency response of the operational impedance, $Z_d(s)$ [7].

4.2.3 Measurement setup

Typical test setups for the SSFR tests include a signal generator which provides the test signals, a power amplifier that amplifies the test signal to suitable levels, the MUT and an analyzer that must be able to measure both magnitude and phase angle differences of two input signals [7].

The following four schematics illustrates the test-setup for each of the measurable quantities

$Z_d(s)$, $Z_q(s)$, $sG(s)$ and $Z_{afo}(s)$. Notice that the rotor position, i.e the direction of the field winding, is different for tests in the d- and q-axis respectively. A brief note on rotor positioning is made in section 4.2.4.

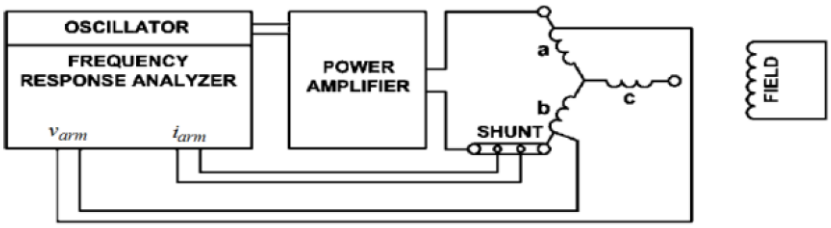

Figure 4.3: Test setup schematic for the d-axis operational impedance, $Z_d(s)$ [7].

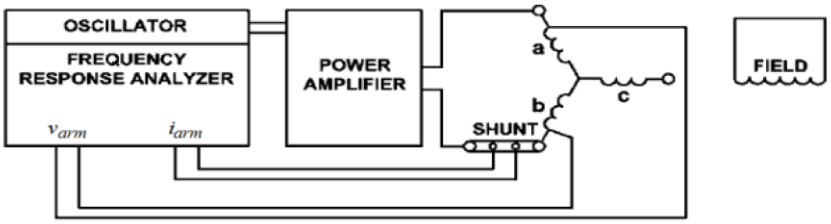

Figure 4.4: Test setup schematic for the q-axis operational impedance, $Z_q(s)$ [7].

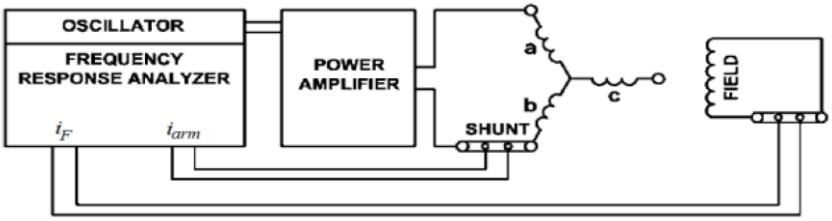

Figure 4.5: Test setup schematic for the armature-to-field transfer function, $sG(s)$ [7].

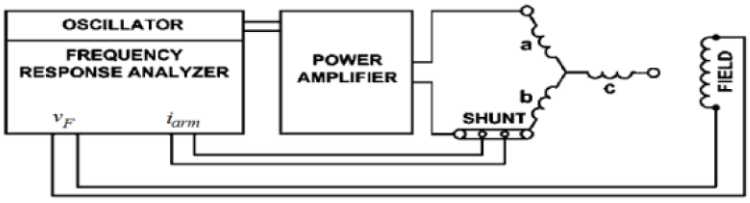

Figure 4.6: Test setup schematic for the armature to field transfer impedance, $Z_{afo}(s)$ [7].

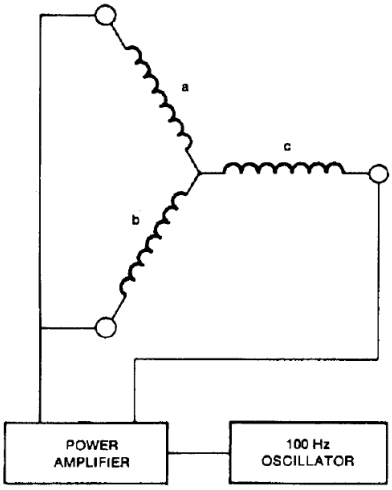

Figure 4.7: Schematic of the stator connection used for d-axis rotor positioning. Adapted from [7].

4.2.4 Rotor positioning

Since the operational parameters are measured independently for the d- and q-axis, the rotor must be positioned in such a way that the stator and field is properly aligned, dependent on the axis the test is performed on [7, 19]. The following procedure, is used to correctly align the rotor for both the d- and q-axis tests [7]:

d-axis alignment Excite all phases of the stator terminals with a 100Hz sinusoidal signal, as illustrated in figure 4.7, and measure the induced field voltage with an oscilloscope. The generator shaft is then slowly turned until the magnitude of the observed field voltage reaches zero. The field winding is then properly aligned with phases a and b, which is used for the d-axis tests.

q-axis alignment For the q-axis alignment, the machine is connected to the signal generator as in the d-axis measurement test setup in figure 4.3. As with the d-axis alignment, the stator is excited with a 100Hz signal and the field voltage is measured with an oscilloscope. The shaft is turned until the magnitude of the field voltage reaches zero. The field winding is then properly aligned, and the setup is ready for the q-axis measurements.

In machines with a large number of poles, a small change in mechanical positioning represents a large change in electrical angle position. Thus, for these types of machines, it may be difficult to accurately position the rotor to the correct alignment [19].

4.2.5 Instrumentation and measurement accuracy

This section describes and considers the type of instrumentation and measurement accuracy required for the SSFR tests. The type of instrumentation presented is as described in the IEEE guide for testing of synchronous generators [7].

Signal generator and power amplifier

The signal generator must be able to generator sinusoidal signals from 1mHz and up to several hundred Hz. In combination with the power amplifier, the signals provided should be able to induce readily measurable responses in both stator and field. Test currents are not expected to exceed 0.5% of the rated armature current of the MUT [7].

In addition, test currents should be small enough as to negate any temperature changes in either the armature, field or damper windings. This is due to the effect temperature changes has on the winding resistance values. In the low-frequency region of the frequency response characteristics for the operational impedances, the armature resistance is mostly dominant, and the test points in this region are therefore susceptible to variations in the winding temperature [7, 22]. It has been reported that the winding resistance experiences a 20mΩ change per degree Celsius, and that the phase measurement can experience a 2° change per mΩ [22]. It is normal to monitor the armature winding temperature during testing, especially in the low-frequency range. Thus, resistance values can be corrected if necessary [19].

Frequency response analyzer

The frequency response is normally measured by a frequency response analyzer. This type of equipment is able to measure the magnitude and phase angle difference of two input signals [7]. It is also not uncommon that the above mentioned signal generator is part of the frequency response analyzer [7]. The necessary basic specification of the analyzer is that it must be able to measure signals in the 1mHz-1kHz region in addition to a phase measurement accuracy down to 0.1° [7].

Measuring accuracy

As previously mentioned, the low-frequency region of the operational parameters are susceptible to large variations for the obtained test points. This may partly be attributed to temperature changes is the windings, but also the noisy signals that appear for low frequencies [7, 22]. Generally, data-acquisition in the low-frequency range is regarded as one of the main challenges for the SSFR test [19], and several instances report the importance of accurate data acquisition and measurement accuracy, especially in the low-frequency range, in order to obtain the best results [7, 22, 19].

The IEEE-guide reports a measurement density of about 10 test points per decade, logarithmically spaced, in the 0.01Hz-1kHz range and 40 test points in the 1mHz-0.01Hz frequency range [7, 22]. However, noise-minimization by averaging the signal over several periods of signal measurement is seen as a way of reducing the amount of test points in the low-frequency region to about 15 points per decade [7].

It has also been reported that higher sampling rates in the lower frequency range improved test results. An example could be a sampling rate of 100Hz in the 1mHz-10mHz range, and 200Hz in the 10mHz-1Hz range [22].

It should also be noted that the q-axis measurements can be expected to be more susceptible to noise than the d-axis measurements and that phase measurements generally are more difficult to determine than magnitude measurements [22]

Measuring devices

For measuring the voltages and currents, voltage probes and current shunts are recommended. For the voltage probes, instruments with differential inputs are preferred. In order to ensure adequate measuring accuracy during testing, these measuring devices' ratings should match the expected test and response voltage and current magnitudes. In addition the connections should be made as close as possible to the generator terminals, and measures should be taken to minimize the effect of contact resistances that might affect the test results [7].

4.2.6 Analysis of test data

In order to produce a transfer-function that fits the test-data, several techniques can be used. In the literature, most of these include some form of curve-fitting technique [7]. Among these are the Maximum-Likelihood Estimation method MLE [20, 19] in addition to Levenberg-Marquadt, and "Pattern-Search" methods [7]. Other alternatives are digital software that enables curve fitting and extraction of curve parameters based on measurement data. One such option is the transfer-function estimation tools in the MATLAB System Identification Toolbox [23], which estimates a transfer function on rational form with a predetermined amount of poles and zeros. It is however, not up to this thesis to establish which of these methods are best to use, and the methods in itself must be investigated separately. For the purposes of this thesis, the transfer-function estimation options provided by MATLAB is used.

Chapter 5

Presentation of machines to be tested

In this thesis, two synchronous machines are tested using known parameter identification tests. These machines are the 75kVA Siemens-Schuckert synchronous machine and the 8kVA Rudolf-Dietze synchronous machine. At the time of writing (Spring 2019), the machines are respectively located at the National Smart Grid laboratory and the F-151 Machine laboratory at NTNU in Trondheim.

5.1 Siemens-Schuckert synchronous machine

The 75kVA Siemens-Schuckert machine is part of a motor-generator set constituting a synchronous generator and a DC-motor. The synchronous machine has a double set of armature windings, enabling each phase to either be coupled in double-star (parallel) or in single-star (series). The coupling affects the rated parameters of the machine. For the purpose of this thesis, the armature is coupled in series.

A schematic overview of the machine is illustrated in figure 5.1. The connections used during testing is as shown on the figure. The nameplate of the synchronous machine is presented in table 5.1.

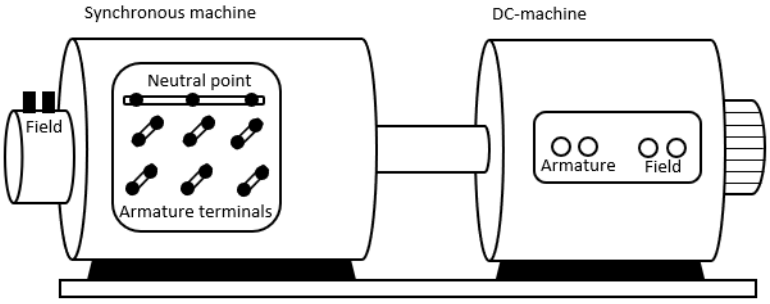

Figure 5.1: An illustration of the Siemens-Schuckert motor-generator set. The armature of the actual machine is coupled in series-star connection, as shown on the figure.

Table 5.1: Nameplate parameters of the Siemens-Schuckert synchronous machine

Machine parameter	**Symbol**	**Value**
Power	S_n	75kVA
Stator voltage (single-star connected)	V_n	450V
Stator line current	I_n	96A
Frequency	f	50Hz
Speed	n_n	1000 rpm

5.2 Rudolf-Dietze synchronous machine

The 8kVA Rudolf-Dietze machine is also part of a motor-generator set consisting of a synchronous machine and an asynchronous motor. A schematic illustration of the machine is shown in figure 5.2, while the machine's nameplate is listed i in table 5.2. The machine's synchronous, transient and subtransient parameters, in addition to fundamental parameters of the d- and q-axis rotor circuits, has previously been identified in a master's thesis from 2017 [11]. These parameters are listed in table 5.3.

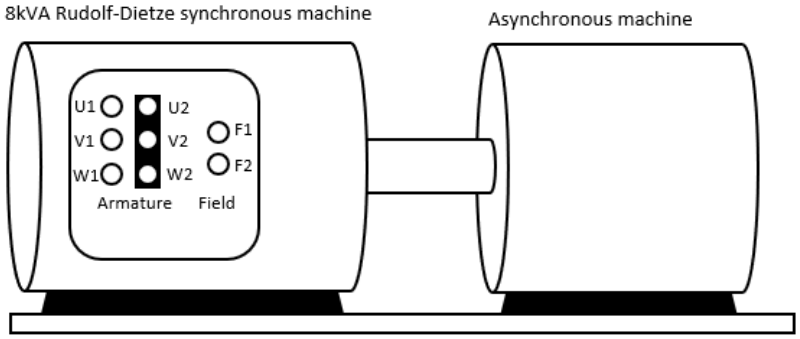

Figure 5.2: Schematic illustration of the Rudolf-Dietze machine. The armature and field winding in the figure is portrayed exactly as the terminals appear on its real-world counterpart.

Table 5.2: Nameplate parameters of the Rudolf-Dietze machine

Machine parameter	**Symbol**	**Value**
Power	S_n	8kVA
Stator voltage (star connected)	V_n	220V
Stator line current	I_n	26.1A
Frequency	f	50Hz
Speed	n_n	1000 rpm
Maximum speed	n_{max}	1500 rpm
Excitation voltage	-	110-140V
Excitation current	-	3.5A
Pole-pairs	pp	3

Table 5.3: Parameters of the Rudolf-Dietze machine as determined in the Master's thesis from 2017 [11].

Resistances and reactances	**Symbol**	**Value**
Armature resistance	Ra	0.2185 Ω
Field resistance	R_f	31.5 Ω
d-axis synchronous reactance	x_d	3.9 Ω
q-axis synchronous reactance	x_q	2.56 Ω
d-axis transient reactance	x'_d	1.32 Ω
d-axis subtransient reactance	x''_d	0.505 Ω
q-axis subtransient reactance	x''_q	0.756 Ω
Time constants		
d-axis transient short-circuit time constant	T'_d	0.069s
d-axis subtransient short-circuit time constant	T''_d	0.0062
Armature time constant	T''_a	0.014s
q-axis subtransient short circuit time constant	T''_q	0.0062
d-axis transient open-circuit time constant	T'_{d0}	0.20
d-axis subtransient open-circuit time constant	T''_{d0}	0.16
q-axis subtransient open-circiot time constant	T'_{q0}	0.21
Mechanical time constant	T''_m	0.41s
Damper-, leakage- and magnetizing reactances		
Stator leakage reactance	$x_{s\sigma}$	0.064
d-axis magnetizing reactance	x_{ad}	0.58
Field winding leakage reactance	$x_{f\sigma}$	0.21
d-axis damper leakage reactance	$x_{D\sigma}$	0.022
q-axis damper leakage reactance	$x_{Q\sigma}$	0.073
d-axis damper resistance	r_D	0.035
q-axis damper resistance	r_Q	0.065

Part II

Laboratory work, results and analysis

In part II of this thesis, the laboratory work, obtained results, data processing and analysis of the results are covered. Part II consists of three chapters. Chapter 6 presents the results of the tests conducted on the Siemens-Schuckert machine, namely the OCC-test, SCC-test and the retardation test. Chapter 7 describes the development and resulting laboratory test set-up and measurement method for the SSFR tests, while Chapter 8 presents the results of the SSFR-tests conducted on the Rudolf-Dietze machine. All chapters contain one or more of the following points:

Laboratory set-up and equipment A description of the equipment and laboratory set-up used for the test. In addition, identification numbers for the different instruments and equipment used is provided for ease of reference in NTNU's digital instrument archive .

Method of measurement Description of the measurement method used to conduct the test in question. Descriptions of any alterations done to the tests with reference to the methods described in the previous chapters are also included.

Results and data processing Test results, in addition to any calculations performed on the basis of test results are provided. Results are presented in table or graphic formats, or should otherwise be accentuated in-text. Some test-data is considered too cumbersome to present in the results. For these results, refer to the relevant Appendix.

Analysis Where appropriate, an analysis of and discussions around the test results are provided.

Concluding remarks and recommendations for further work are included at the end of part II.

Chapter 6

Test results for Siemens-Schuckert machine

I this chapter, the methodical approach used for testing the Siemens-Schuckert machine, in addition to the results obtained from the OCC-, SCC- and retardation tests, are presented.

A schematic set-up for the tests is presented in figure 6.1. As illustrated, the prime mover used to drive the machine during the tests was the DC-motor constructed as part of the Siemens-Schuckert motor-generator set. The nameplate of the DC-motor is shown in table 6.1. The field of the motor was supplied by the Elektro-Automatic DC-supply, while the armature was excited using the in-house developed drive-converter for the DC-machine. The converter is a 6-phase interleaved chopper [24], fed by the Delta Electronica DC-supply. A complete overview of instruments used for excitation of the machines, and the measurement instruments used, is presented in table 6.2.

It should be noted that values for voltage and currents in the subsequent sections are presented in RMS-values.

The speed regulation option of the converter control system was used to excite the DC-machine for operation at 1000rpm. The breakaway current, i.e the current required for starting the machine, measured approximately 150A on the Delta Electronica supply. The machine runs at rated speed when the Delta Electronice supply measures approximately 220V, the field excited by approximately 42V and 3.66A.

Table 6.1: Nameplate of the Siemens-Schuckert DC-motor

Machine parameter	Value
Power	46kW
Rated voltage	120V
Rated current	115A
Rated speed	1200rpm

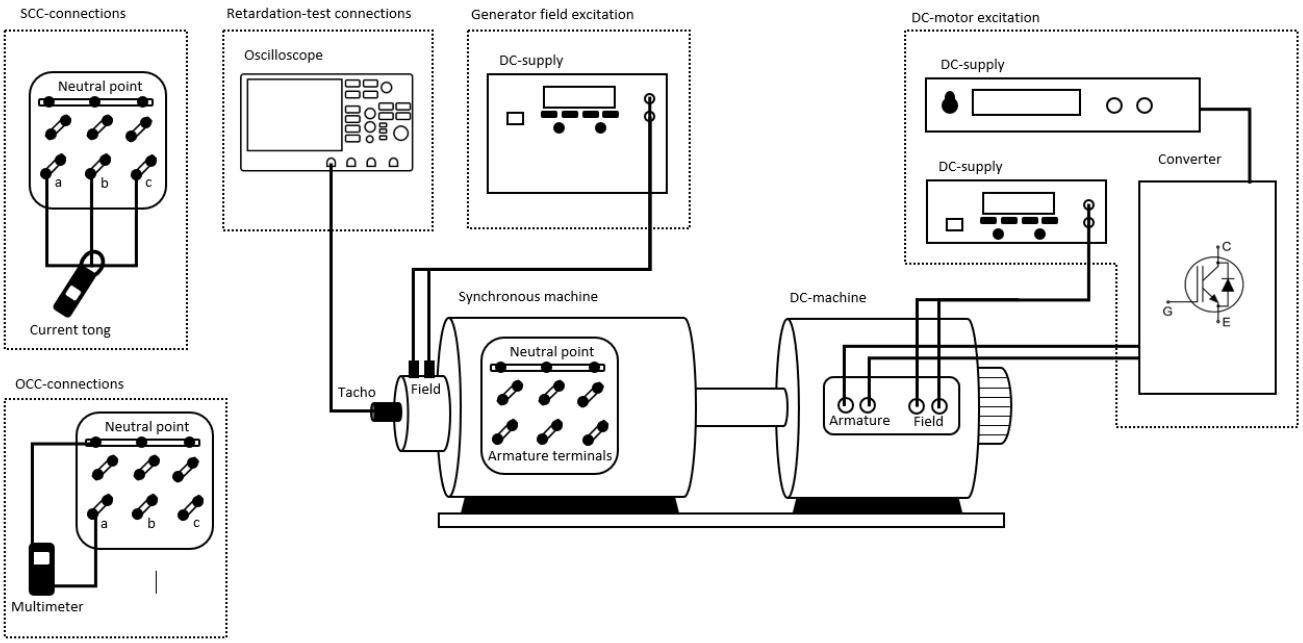

Figure 6.1: Schematic set-up of the machine excitation systems and the connections on the armature and field terminals of the synchronous machines for the different tests.

Table 6.2: List of equipment used for the open-circuit characteristic test, the short-circuit characteristic test and the retardation test.

Number	Instrument	Model type	ID-nr.
1	Synchronous generator	Siemens-Schuckert	A02-0035
2	DC-motor	Siemens-Schuckert	A01-0136
3	DC Power supply	Elektro-Automatik	B02-0729
4	DC Power supply	Delta Electronica	B02-0737
5	DC Power supply	ET System	B02-0527
6	Current clamp	FLUKE	I04-0308/0327/0324
7	Current clamp	HIOKI 3285	I04-0373
8	Multimeter	Fluke	S03-0415/0465/0439/0436
9	Oscilloscope	Tektronix	G04-0375
10	Milliohm meter	HIOKI	H01-0128
11	Converter	-	-

6.1 Open-circuit characteristic test

The open circuit characteristic test was conducted with the set-up illustrated in figure 6.1. The machine was operated at rated speed and the open-circuit voltage was measured on the three FLUKE multimeters between each phase terminal and the neutral point. As recommended in the IEEE-test guide, 6 measurements with 10% increments was recorded for the first 60% of rated voltage. The synchronous machine field current supply was adjusted until the desired percentage of rated voltage was measured on the multimeters. Between 60% and 110% of the rated voltage, measurements per 5% interval in armature voltage were recorded. Due to

the age of the machine, and to ensure its safety, only one of the two recommended readings above 110% was taken. The reading was recorded at 120% rated voltage. Table 6.3 show the measurements for each phase.

Table 6.3: Open-circuit characteristic measurements of the Siemens-Schuckert synchronous machine.

$\mathbf{I_f}$(A)	$\mathbf{V_a}$(V)	$\mathbf{V_b}$(V)	$\mathbf{V_c}$(V)
0	2.09	2.09	2.09
0.6	26.1	26.13	26.1
1.3	51.9	51.9	51.9
1.9	77.4	77.4	77.4
2.6	104.1	104.1	104.1
3.2	129.5	129.6	129.6
4	156.4	156.5	156.4
4.3	169.2	169.3	169.2
4.6	182	182	182
5	195.1	195.2	195.1
5.4	207.8	207.8	207.8
5.8	221.2	221.3	221.2
6.2	234.2	234.3	234.2
6.6	246.9	246.9	246.8
7.1	260.1	260.1	260.1
7.5	273.2	273.3	273.2
8.1	286	286	286
9.2	311	311	310.9

The OCC of the machine was constructed using the average value of the measured phase voltages. The measured points was fitted using the MATLAB Curve Fitting App from the Curve Fitting Toolbox [25], with the resulting 2nd order function being $V = -1.139{I_f}.^2 + 44.86I_f - 1.735$, having a R^2-value of $R^2 = 0.9994$. Two air-gap lines were constructed. Following the recommendations of the IEEE-guide, one air-gap line was constructed using the tangent-line to the fitted OCC at the origin [7]. The other air-gap line was constructed using a linear line-fit of the first 6 measurement points. The linear fit resulted in the expression $V_{oc} = 39.67I_f + 1.72$, with $R^2 = 0.9997$. The OCC-fit, including measurement points, and the two air-gap lines are displayed in figure 6.2.

6.2 Short-circuit characteristic test

For the short-circuit characteristic tests, two cables was bolted between phase 'a' and 'b', and between phases 'b' and 'c' on the synchronous generator armature terminals to create a solid, three phase short-circuit. This is shown in figure 6.1. The machine was run at rated speed using the speed regulating option of the supply-converter, ensuring that measurement were taken at 1000rpm. Currents in each phase was measured using the FLUKE current tongs in table 6.2. For phase 'b', the current tong enclosed both of the cables connecting the three

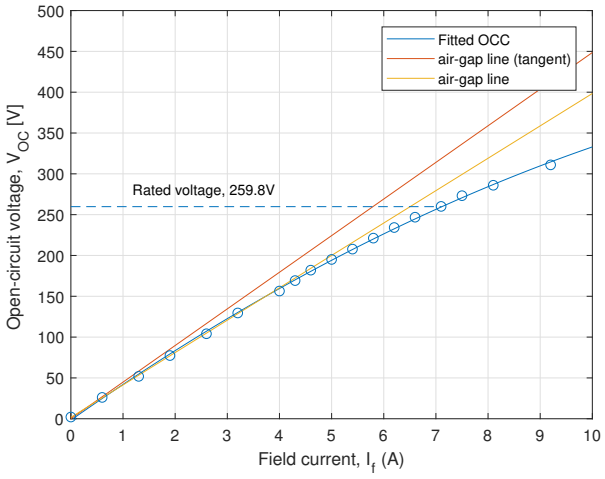

Figure 6.2: Open-circuit characteristic of the Siemens-Schuckert machine, including two air-gap lines. The first is tangent to the fitted line at the origin, the other is a linear fit to the 6 first measurements of the OCC. Voltages are given as phase-to-neutral values.

phases. Measurements were taken at approximately 85%, 75%, 50%, 25% and 0% of rated armature current, starting with the largest armature current as recommended by IEEE [7]. To ensure the safety of the machine, it was decided to not make any measurements above 85% of the rated current. The measurements are listed in table 6.3. The MATLAB Curve Fitting App was used to create a linear fit, $I_{sc} = 22.44I_f + 1.821$, $R^2 = 0.9998$, which is displayed alongside the measurements in figure 6.3.

Table 6.4: Short-circuit characteristic measurements of the Siemens-Schuckert synchronous machine.

$\mathbf{I_f}$(A)	$\mathbf{I_a}$(A)	$\mathbf{I_b}$(A)	$\mathbf{I_c}$(A)
0	1.8	1.8	1.2
1	24.2	24.3	24.1
2.1	49.6	50.1	49.5
3.2	72.9	73.5	72.8
3.5	80	81	80.3

6.3 Retardation test

The retardation test was performed by operating the DC-motor up to rated speed using the speed-regulation option of the converter. After about two minutes, the armature-current supply was cut off, letting the rotor shaft of the machine freely rotate until standstill. The rotational speed of the machine was measured continuously by a tachometer, the data being processed by an oscilloscope. The resulting retardation curve is displayed in figure 6.4.

In addition, for the calculations conducted in the next section, measurements of armature current and voltage was recorded. The recordings was performed with an amperemeter and a

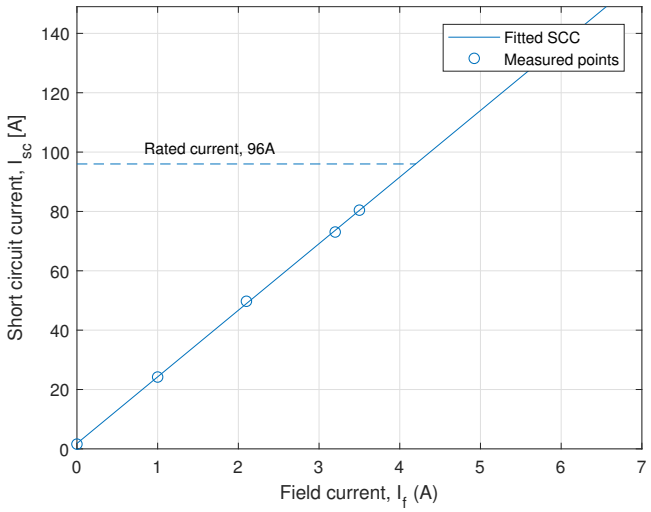

Figure 6.3: Short-circuit characteristic of the Siemens-Schuckert machine.

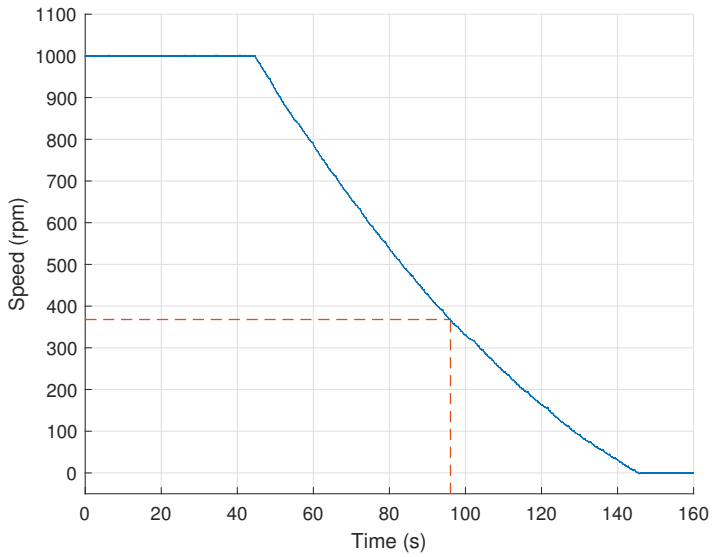

Figure 6.4: Retardation curve of the machine. The time constant is equal to $\tau = 96.06s$, as can be read from the curve.

multimeter respectively, the multimeter being connected on the converter terminals. Measurements of the armature resistance was conducted beforehand with the HIOKI Milliohm-meter. The measured values are presented in table 6.5.

Table 6.5: Armature voltage- and current measurements at no-load and rated speed. The armature resistance was measured at standstill.

Parameter	Measured value
Armature current, I_a	37.7A
Armature voltage, V_a	115.1V
Armature resistance, R_a	67.7mΩ

6.4 Inertia calculation

The rotor inertia is calculated in the same way as conducted in [26].

From section 3.3, it was found that the equation for the retardation curve can be described with the following equation, where the time constant, τ, represents the rate of decay of the curve. This is the same equation described in section 3.3.

$$\omega = \omega_0 e^{\frac{-t}{\tau}} \quad , \qquad \tau = \frac{J}{D_d} \tag{6.1}$$

Notice that the time constant, τ is dependent upon the damping-torque coefficient, D_d, and the rotational inertia, J. In addition, D_d can further be expressed by the idling torque, T_0 of the machine, that is the torque associated with running the machine at no-load and rated speed. This is expressed in equation 6.2 below, which is also described in section 3.3.

$$T_0 = D_d \omega \tag{6.2}$$

Thus, by knowing the idling torque, T_0, and the time constant, τ, the inertia of the rotor can be obtained. The idling torque can be determined by considering the equations for induced torque and induced voltage in a DC-machine [16], as expressed in equation 6.3 and 6.4 below.

$$E_a = k\Phi\omega \tag{6.3}$$

$$T_{ind} = k\Phi I_a \tag{6.4}$$

Here, k, is a machine constant, Φ is the air-gap flux, ω is the rotational speed of the rotor, I_a is the armature current, while E_a and T_{ind} is the internal generated armature voltage and induced torque respectively. Combining these equations yields the following:

$$T_{ind} = \frac{E_a I_a}{\omega} \tag{6.5}$$

Using the measured values in table 6.5, and Kirchoff's voltage law for DC-machines [16], the internal induced voltage is calculated:

$$E_a = V_a - R_a I_a - E_b = \underline{\mathbf{110.55V}} \tag{6.6}$$

Here, E_b is the brush voltage drop. This voltage can be neglected, or is usually a fixed voltage drop of 1-2V [16, 27]. In this thesis, the brush voltage drop is considered to be 2V.

Using the calculated value of E_a and I_a, the idling torque, T_0 becomes:

$$T_0 = \frac{E_a \cdot I_a}{\omega} = \frac{110.55V \cdot 37.7A}{1000rpm\frac{2\pi}{60}} = \underline{\mathbf{39.8Nm}} \tag{6.7}$$

The damping-torque coefficient is then determined by utilizing equation 6.2:

$$D_d = \frac{T_0}{\omega} = \frac{39.8}{1000rpm\frac{2\pi}{60}} = \underline{\mathbf{0.38Nms}} \tag{6.8}$$

The time constant can be extracted from the deceleration curve. The time constant is defined as the time it takes for the speed to reach $\frac{1}{e}$ of the initial value of $\omega_0 = 1000rpm$ [18]. From the curve, this equates to $\underline{\tau = \mathbf{96.06s}}$.

Thus, the rotational inertia of the machine can be computed as follows:

$$J = \tau \cdot D_d = 96.06s \cdot 0.38Nms = \underline{\underline{\mathbf{36.5kgm^2}}} \tag{6.9}$$

It can also be expressed as the *inertial time constant*, H.

$$H = \frac{1}{2}\frac{J\omega^2}{S} = \frac{1}{2}\frac{36.5kgm^2 \cdot (1000\frac{2\pi}{60})^2\frac{1}{s^2}}{75kVA} = \underline{\underline{\mathbf{2.67s}}} \tag{6.10}$$

Chapter 7

SSFR measurement set-up and test procedure

This chapter concerns itself with the development of the laboratory set-up and the test procedure used for the SSFR-tests. Preliminary tests were conducted, based on the recommended measurement methods outlined in Chapter 4, and available equipment. The goal with these tests was to obtain practical experience with the instruments, to establish what instruments provided the best test results and establishing a test-procedure to be used in the final SSFR-tests.

This chapter is divided into two parts. First, the resulting laboratory test set-up is described, including descriptions of the most notable equipment used. Secondly, the test-procedure developed from the preliminary tests is presented, including strategies for enhancing the test results.

The actual SSFR-tests are presented in Chapter 8.

7.1 Laboratory set-up development

A schematic for the laboratory test set-up used to conduct the d-axis operational inductance measurements is illustrated in figure 7.1. The test set-up shown here is principally the same as for the other d-axis and q-axis tests, only changing the rotor position and the measurement probe connections between tests. The other test set-ups are illustrated in Chapter 8.

The set-up includes a function generator to excite the terminals of the synchronous machine, an amplifier for amplifying the test signal and an oscilloscope for measuring the resulting waveforms and phase shifts. A complete list of the equipment used for all further tests presented in this thesis, is listed in table 7.1.

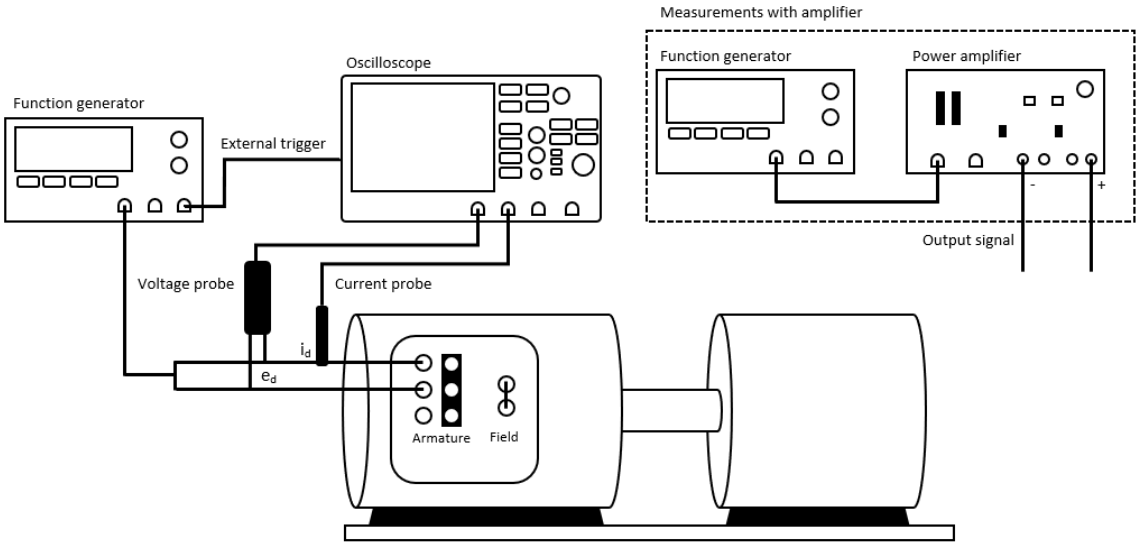

Figure 7.1: Principal schematic of the developed SSFR test set-up.

Function generator

The Tektronicx AFG31052 [28] was used as the arbitrary function generator in the set-up. The generator has the capacity of generating sinusoidal signals of 10Vpp in the required frequency interval of 1mHz-1kHz. It is equipped with two independent channels, in addition to an external trigger channel. During preliminary testing on the Rudolf-Dietze machine, a 10Vpp signal output of the signal generator measured an approximately 200mA input current on the generator. With a rated current of 26.3A, this was deemed sufficient for the recommended magnitude of test currents, about 0.5% of rated armature current. As is discussed later, it was discovered that the test currents would decrease for lower frequencies.

Power amplifier

In order to keep the armature current constant at approximately 0.5% of the rated current, the Toellner TOE 7610-20 power amplifer was used. The power amplifier is able to amplify the input voltage from the signal generator up to 40Vpp, and a maximum output current of 7.5A [29]. The amplifier also has a frequency bandwidth of 2Hz-30kHz for AC-coupling and 0Hz-30kHz for DC-coupling .

Oscilloscope

The Rohde & Schwarz RTO2044 digital oscilloscope was used as a substitute for the recommended frequency response analyzer in order to measure the magnitudes and phase shift of the measured waveforms. An attempt at acquiring a frequency response analyzer was made by e-mail to other departments at NTNU, but was unsuccessful, and it seems that no such

equipment currently exist at NTNU. For future SSFR-studies, a frequency response analyzer should be acquired.

The oscilloscope was chosen due to its high sample rate of up to 20Gsamples/s, accurate trigger system, low noise-floor and high presicion measurements [30]. In discussions with the laboratory personnel, this seemed like the best option in lieu of a frequency response analyzer.

Measuring probes

For the measurement probes, the preliminary tests provided comparable measurements from which to establish which of the probes were the best and most accurate to use for the SSFR-tests. Several probes, both differential and current probes were tested. The signal-to-noise ratio for the different probes were mainly considered due to the corrupting nature signals with larger signal-to-noise ratios had on the measurements made by the oscilloscope. This resulted in the choice of the Rohde & Schwarz RT-ZC30 and FLUKE current probes, in addition to the Tektronix P5200 differential probe.

Table 7.1: Measurement list for the instruments and equipment used for the SSFR-tests.

Number	Equipment	Model type	ID nr.
1	Oscilloscope	Rohde & Schwarz RTO2044	G04-0385
2	Function generator	Tektronicx AFG31052	B03-0629
3	Power amplifier	Toellner TOE 7610-20	B03-0479
4	Differential probe	Tektronix P5200	I06-0490
5	Current probe	FLUKE	I04-0520
6	Current probe	Rohde & Schwarz RT-ZC30	G04-0385-03
7	Milliohm-meter	HIOKI RM3548	H01-0127
8	Synchronous generator	Rudolf Dietze	A02-0021

7.2 Test procedure

As described in section 4.2.5 about measuring accuracy, accurate data acquisition is important to consider for the best possible test results. It was therefore important to identify aspects of the test-setup and the test procedure that might affect the measurements. These aspects include factors that affect the actual measurements, such as winding temperature, but also aspects regarding the test set-up and correct operation of test instruments and equipment. Preliminary tests were performed, both to obtain experience with the equipment and to identify where in the test set-up sources of error might arise, and what measures that could be taken to eliminate these sources of error. Based on these tests, a strict test procedure was developed with the goal of eliminating source of error, and strategies to use in order to enhance the accuracy of the test results.

The test-procedure is separated in two distinct procedures: an initiation procedure, which includes preparations to be done before testing, and the method of measurement, which includes strategies for enhancing the accuracy of test results. The complete measurement procedure applies for all the SSFR-measurements.

7.2.1 Initiation procedure

The initiation procedure was performed at the beginning of each measurement cycle. The goal was to create a basis for measuring to ensure that all measurements taken was taken on the same system, eliminating any differences in the test-setup between measurements. The complete initiation procedure is described step-wise below:

Step 1: Oscilloscope calibration

The oscilloscope was calibrated using a split signal from one of the function generator output channels connected to the oscilloscope channels to be used for the actual measurements. The set-up is illustrated in figure 7.2. A 100Hz 10Vpp signal was applied. The two sinusoids shown on the oscilloscope was then positioned right on top of each other by adjusting the position of one waveform either horizontally or vertically. This way, any relative measurements between the channels, such as phase measurements, is taken on the correct reference.

Step 2: Probe calibration

Measurement probes used for the measurements was correctly calibrated, as described in their respective user manuals [31, 32, 33]. The user manuals can be found in NTNU's digital instrument archives.

Step 3: Rotor alignment

Correct rotor alignment was initiated with the machine being connected to the function generator and oscilloscope as illustrated in figure 7.3. The connection used was dependent on wheteher d- or q-axis tests was to be done. A 100Hz 10Vpp signal was applied to the armature terminals, and the resulting induced field voltage was observed on the oscilloscope. The rotor was then turned until the voltage waveform was nearly nulled, and the minimum voltage obtained was recorded.

7.2.2 Measurement method

The measurement method follows the general test procedure as outlined in section 4.2.2, with some adjustments. This section describes the procedure in detail. When using a digital oscilloscope with fine resolution such as in this thesis, it was discovered that the obtained signals often contained varying degrees of noise. In addition, for frequencies $<\sim$1Hz, it was difficult

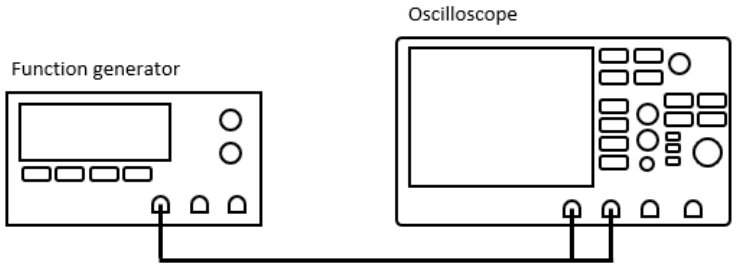

Figure 7.2: Schematic set-up for oscilloscope calibration.

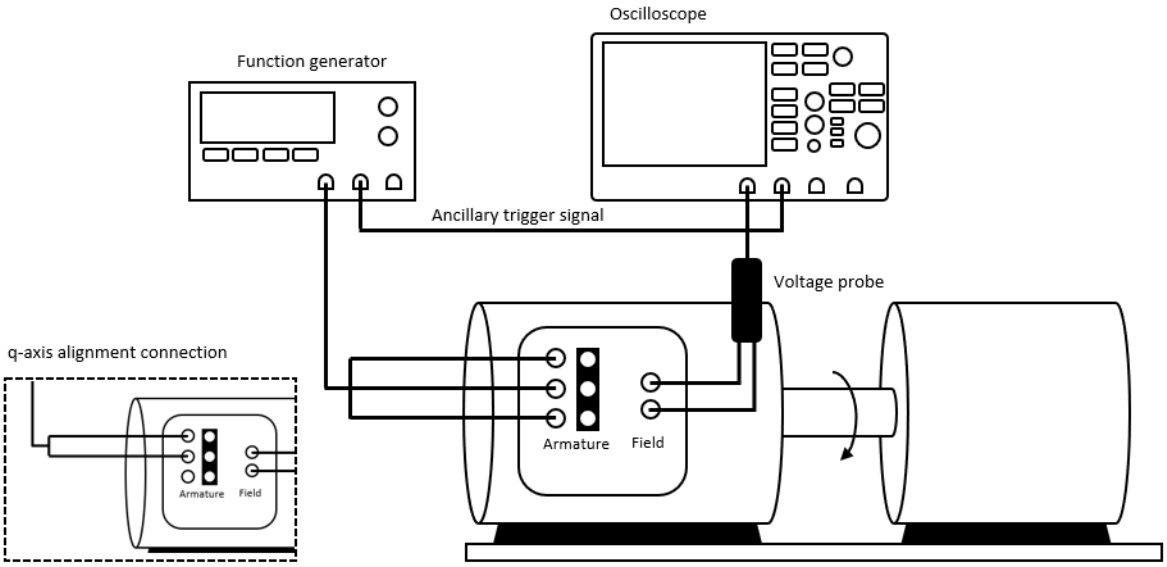

Figure 7.3: Schematic set-up for d-axis rotor alignment. The q-axis connection for q-axis rotor alignments is illustrated in the bottom left corner. An ancillary trigger signal can be used for easier waveform triggering.

to obtain stable waveforms. This affected the ability of the oscilloscope to make accurate measurements on and between the test signals. Therefore, during the preliminary tests, strategies for enhancing the test signals and for obtaining more accurate results was developed. These strategies are briefly described below, in addition to the measurement procedure.

Measurement procedure

Step 1: Test set-up

☐ The instruments were set up and connected according to the relevant test. These test set-ups are illustrated in figure 8.1, 8.18 and 8.16, in the relevant results- and analysis sections.

Step 2: Data acquisition

☐ A 1kHz signal was applied to the machine's armature terminals, and the response

of the resulting waveforms of currents and/or voltages in either stator or field was measured on the oscilloscope.

- ☐ The signals were measured using the 'High'- and 'Phase'-measurement types on the oscilloscope. The 'High'-function measures the highest point of the waveform, i.e the largest amplitude measured, while the 'Phase'-function measures the phase shift between the two waveforms [30]. The phase shift is measured in degrees [30].
- ☐ The 'Statistics'-function on the oscilloscope was used to obtain a statistically more accurate measurement of the amplitude and phase shift. The 'Statistics'-function measures the relevant parameters over several cycles of the test signals, enabling the recording of quantities such as averages, RMS-values, standard deviation and the amount of waveforms the calculations take into account [30]. The calculated averages of the amplitude and waveform phase difference were recorded manually in a Microsoft Excel sheet.
- ☐ The process described above was then repeated a number of times, each time changing the frequency of the generated test signal. The frequencies used for testing was predetermined in order to generate approximately 10 recordings per frequency decade, as discussed in section 4.2.5.

Measurement accuracy strategies

As previously mentioned, preliminary tests showed that noisy waveforms might heavily distort the oscilloscope's ability to make accurate measurements of both amplitude and phase shift. In addition, for lower frequencies, it became harder for the oscilloscope to portray waveforms correctly, and to maintain a steady waveform on-screen, which also affected the measurements performed. Thus, several strategies was developed in order to enhance the oscilloscope's ability to conduct these measurements.

Signal filtering

A digital filter of 100kHz was used to reject high frequency noise on the measurement signals [30]. This filter was applied to all measurement channels, and was used at all times during the SSFR-testing.

High-res mode

In order to portray waveforms with higher vertical resolution, the 'High-res' mode of the oscilloscope's acquisition set-up was used. This option changes the sampling method of the oscilloscope by averaging n numbers of samples and portraying the average value as one sample point [30]. This strategy was utilized during rotor positioning and for almost all the SSFR-tests, especially for lower frequencies.

Waveform averaging

The 'Average' waveform arithmetic method was used when signals became too difficult to measure using the default specifications of the oscilloscope. This includes low-amplitude, high-noise and/or low-frequency waveforms. The method builds the digitized waveforms based on the average of several acquisition cycles. It reduces random noise [30] and seems to create a signal more suited for measurements. The strategy was used extensively during testing and for accurate rotor positioning.

Ancillary trigger signal

An ancillary trigger signal was used when the oscilloscope had difficulties triggering, i.e creating stable waveforms based on the test-signals alone. The strategy is based on creating an easily portrayable signal for the oscilloscope to trigger on. Channel 2 of the function generator was set to apply a signal with the same frequency as the exciting signal used for the SSFR-tests, while directly connected to a free channel on the oscilloscope. This channel was then used as the trigger-channel in the trigger set-up menu. In the schematic for axis-alignment shown in figure 7.3, the connections of such a signal is illustrated.

Sampling rate

For lower frequencies, i.e < 5Hz, the sampling rate was reduced in order to produce more readily measurable signals.

Chapter 8

SSFR-test results and analysis

In this chapter, test set-up, results and analysis of the SSFR-tests are presented. The chapter is divided in four parts, as described below.

1. **Preliminary tests**

   Preliminary tests of $L_d(s)$ and $L_q(s)$ were performed in order to test the test set-up, decide what equipment was best to use and how to obtain the best results. Test results and analysis are provided. Results regarding the test-instrumentation has previously been discussed in Chapter 7 and is therefore not discussed further. Measurement results are included in Appendix F.

2. **Resistance measurements**

   The method for accurate determination of the armature winding resistance R_a is provided. Measurements are presented in Appendix D.

3. **SSFR-tests**

   Four tests are performed, one for each of the operational parameters $L_d(s)$, $L_q(s)$, $sG(s)$ and $Z_{afo}(s)$. Test set-ups, measurement method, results, data-processing and analysis of results are provided. Measurements results are provided in Appendix G.

4. **Parameter estimation**

   A parameter estimation method using a MATLAB transfer-function estimation function is presented. A validation study of the method is performed on a machine with known parameters. Lastly, the method is used in an attempt at estimating some of the transient parameters of $L_d(s)$, $L_q(s)$ and $G(s)$. Analysis of results are provided.

A note should be made that, if not otherwise specified, the initiation- and measurement procedure, as well as the measurement strategies stated in the previous chapter, are all used for all relevant tests presented in the following sections.

8.1 Preliminary tests

For the preliminary tests of the operational parameters $L_d(s)$ an $L_q(s)$, the test set-up as illustrated in figure 8.1 was used. The difference in test set-up was the rotor positioning, which was correctly positioned in advance of each test, as outlined in section 4.2.4.

Three types of tests were performed:

- **Base test** The base test was performed by exciting the terminals with a constant **10Vpp** signal for all frequencies.
- **Constant current** In order to keep the test-current in the preferred 0.5%-range of the machine's rated value, a test was performed while keeping the test-current at approximately **150mA** for all frequencies. As shown in table 5.2, the machine's rated current is 26.1A.
- **High current** The high current test was performed in order to test if a higher current had any significant impacts on the results. The test-signal was maintained at approximately **250mA** for all frequencies.

The constant- and high-current tests was performed with the amplifier connected. The base test was performed exclusively with the function generator. Also, the high-current test was only performed during testing of $L_d(s)$.

When calculating the operational inductances, the armature resistance R_a is needed. The armature resistance was therefore measured using the HIOKI milliohm-meter. Each of the phases were measured separately, and the average values of these measurements were used in the calculations. The obtained value was $\mathbf{R_a = 0.231\Omega}$. This value is relatively consistent with the value used in earlier testing of the machine [11], which was measured at $R_a = 0.2185\Omega$.

8.1.1 Preliminary measurement results

The results from the $Z_d(s)$- and $Z_q(s)$-measurements are shown in figure 8.2a and 8.2b. The resulting curves are consistent with what was expected. At higher frequencies, the resistance of the conductor is higher due to decreasing skin depth. This is illustrated by the increasing linear part of the magnitude curves of $Z_d(s)$ and $Z_q(s)$, and can also be illustrated by plotting the real part of the impedances, as illustrated in figure 8.3.

Also, the phase increases for higher frequencies. At low frequencies, the magnitude of the operational impedances are mostly governed by the armature resistance, leading to a magnitude which is almost purely resistive, and accompanied by almost zero phase shift. However, as the inductive part of the operational impedances increase, both the magnitude and phase shift increase. This is consistent with an impedance that shifts towards a more inductive nature.

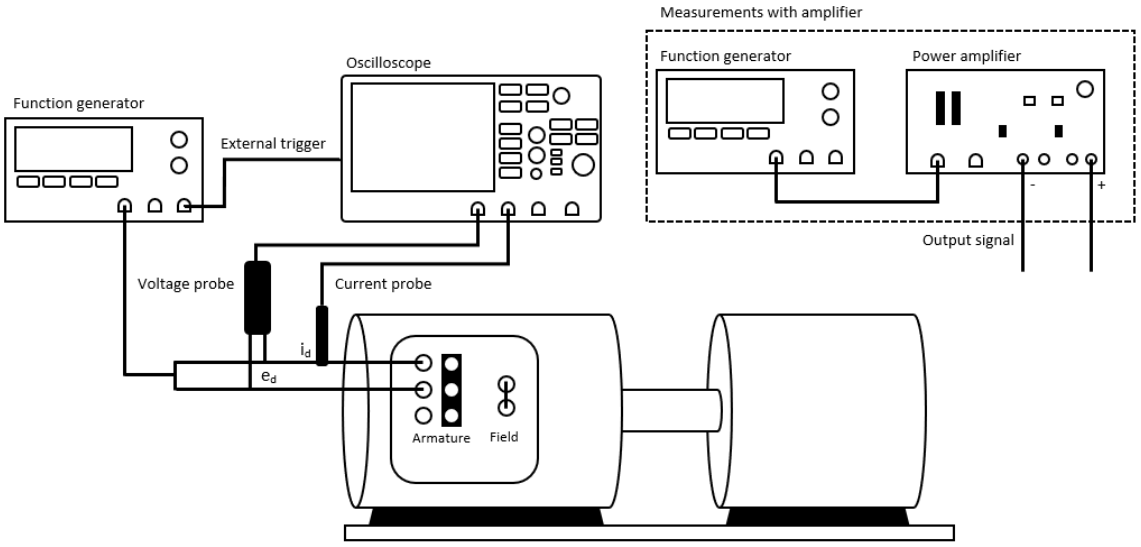

Figure 8.1: Schematic test set-up for the d-axis operational impedance measurements. The dotted square in the top-right corner illustrates the connections using the amplifier. In that case, the output signal connectors are connected to the armature terminals of the machine.

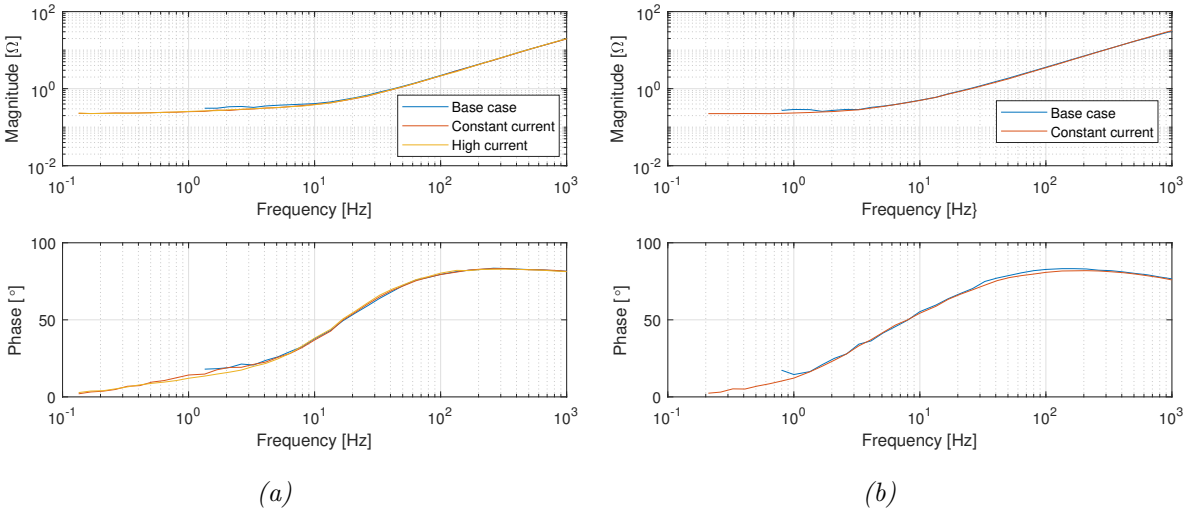

Figure 8.2: Comparison of the resulting frequency responses for the d- and q-axis operational impedances $Z_d(s)$ (a) and $Z_q(s)$ (b).

By using equations 4.4 and 4.5, the operational *inductances* $L_d(s)$ and $L_q(s)$ was calculated. The script used for the calculations are shown in Appendix C.2. The resulting frequency responses is illustrated in figures 8.4a and 8.4b.

In contrast to the operational impedances, the magnitudes of the operational inductances *decrease* for higher frequencies. As the expression $sL(s) = Z(s) - R_a$ states, the magnitude of the inductance should decrease due to the increasing value of R_a for higher frequencies.

However, what is most apparent with the frequency responses illustrated in figures 8.2 and 8.4 is the relatively short frequency range of measurement, the degree to which the base test,

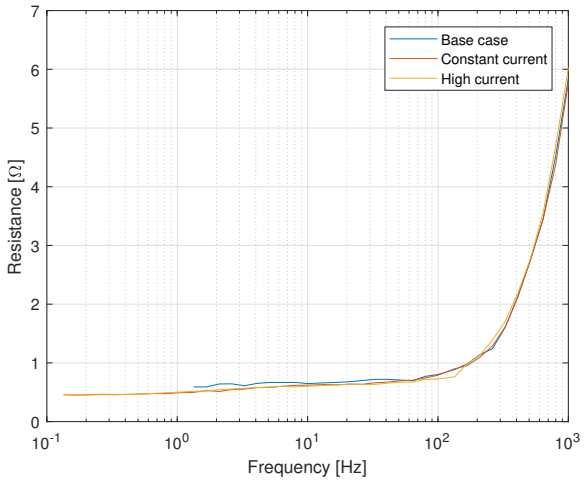

Figure 8.3: Comparison of the real part of the d-axis operational impedance, $Z_d(s)$. Notice the dramatic increase in resistance for higher frequencies.

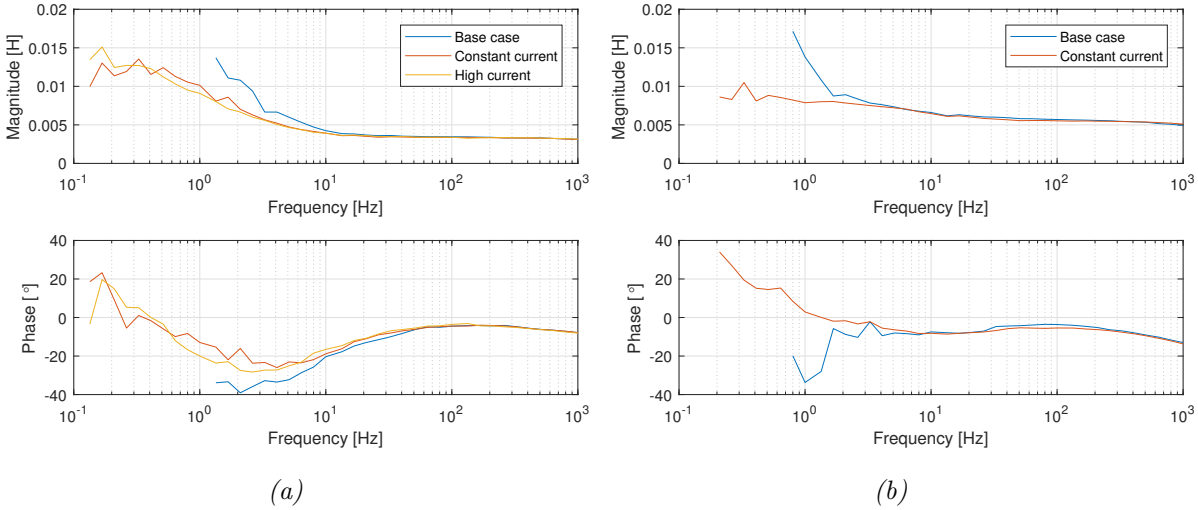

(a) *(b)*

Figure 8.4: Comparison of the resulting frequency responses for the d- and q-axis operational inductances $L_d(s)$ (a) and $L_q(s)$ (b).

constant current test and the high current test diverge. This is discussed further in the next section.

8.1.2 Low-frequency measurements

During the preliminary tests described above, it quickly became apparent that the oscilloscope, used for measuring waveforms, had increasing difficulties with measurements in the low frequency region. As can be seen from the frequency responses for the operational impedances and inductances, the measurements stops in the 1-10Hz range for the base case, and 0.1-1Hz range for the constant and high current tests. In these parts of the frequency spectrum, stable

and triggered waveforms was increasingly difficult to obtain until, at some point, it became virtually impossible for the oscilloscope to obtain any reasonable data or make any measurements at all. For example, the leftmost point on the curves in the frequency response plots above was the last point that the oscilloscope was able to measure using the strategies described in section 7.2.2. The oscilloscope was not able to measure anything for frequencies any lower than this.

The main reason for these difficulties comes from the fact that the oscilloscope was not able to create a stable, triggered signal for low frequencies. When measuring the test points, as described in section 7.2.2, an averaging of the signals was used to provide the most accurate measurement possible. However, this function only works for relatively stable and triggered signals, and when no waveforms can be generated, no measurements based on this 'averaging' can be done. Consequently, the measurable frequency range of the tests performed in this thesis is approximately 0.1-1000Hz.

At the same time, signals take longer to complete a full cycle for lower frequencies. When 'averaging' these low-frequency waveforms, fewer cycles are used for the 'averaging', possibly making the measurements less accurate. In combination with noisier signals and small response amplitudes, the lowest amplitudes in this range being in the order of several hundred μV to 1-2mV, these factors may cause less accurate measurements. For this reason, data acquisition in the low frequency range can be assumed to be less accurate than for higher frequencies.

From this, the following conclusions can be made:

- It is impossible to obtain the complete frequency response of the operational parameters with the current test set-up. The implications of this is that it is impossible to identify the complete set of machine parameters.
- Measurements in the low-frequency region can be assumed less accurate than in the high-frequency range.
- With regards to competence development, and to future work and studies into SSFR-tests on the Rudolf-Dietze machine, the SSFR-tests are still performed, but only in the measurable frequency region.

8.1.3 Sensitivity to armature resistance

As can be seen in figure 8.4, the base case, constant current and high current tests seem to diverge somewhat, especially in the low-frequency region. The reason for this might be less accurate measurements in the lower frequency range, as discussed in the previous section. However, when taking figure 8.2 and the operational impedance measurements into consideration, the measurements seem to still be consistent with the trend in the measurements, not diverging in any significant way. This makes an argument that other factors might affect the diverging nature of the different operational inductance plots.

One such factor is the armature resistance, R_a. In the literature, the armature resistance is deemed an important parameter to accurately determine in order to mitigate possible large errors in the operational inductance for low frequencies [7]. Consider first figure 8.5, and how dramatically the low frequency region of the plots are affected to even small changes in armature resistance.

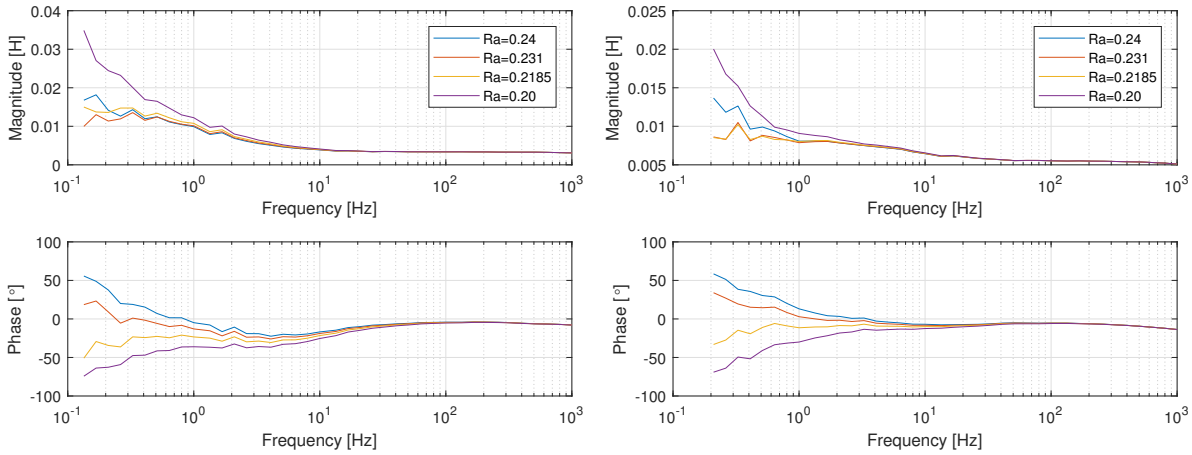

Figure 8.5: The figure illustrates the sensitivity of the operational inductances, $L_d(s)(a)$ and $L_q(s)(b)$, to the armature resistance value, R_a. The test used for comparison, in both (a) and (b), are the constant current test cases.

In addition, notice how different the base case is from the constant- and high current tests in figure 8.4. Even though all operational inductances were calculated using $R_a = 0.231$, the curves look drastically different. With the constant- and high current tests however, there seems to be small differences between the curves, in contrast to the base case. As already discussed in section 4.2.5, the temperature in the windings may affect the resistance in the armature windings. In the example of the constant- and high current tests, the current is relatively constant throughout the test, the currents held constant at approximately 150mA and 250mA respectively. Thus small resistance changes would be expected throughout the tests. In the base case however, the current changes throughout the test, varying in the range of 30-180mA in the 1-5Hz frequency range. This may cause the armature resistance to change during the test, especially in the lower frequency region when more time is needed to record any measurements. This may explain the more sudden increase or decrease in magnitude and phase for the base case when compared to the constant- and high current cases. It may also explain why the constant- and high current cases seems to follow each other more closely in the low frequency range. When the current is constant, the temperature change is minimal, which results in small changes in resistance. The differences between the constant- and high current cases can then be attributed to the difference in winding temperature between the two tests, however this has not been confirmed.

From this, the following conclusions can be made:

- The operational inductance calculations are very sensitive to the armature resistance, R_a. In order to provide the most accurate test results, accurate determination of the armature resistance value is required. The following section discuss the determination of a more accurate value of the armature resistance.
- In order to obtain accurate test results, the temperature must be kept as constant as possible throughout the test. For further tests, the temperature is then kept constant by keeping the test currents at approximately the same level throughout the test. All further tests were performed by keeping the test-current constant at approximately **150mA**.

8.2 Armature resistance measurements

A new, more accurate armauture resistance measurement was performed in order to obtain a more accurate value for the armature resistance of the Rudolf-Dietze machine. The process of measuring is described briefly below.

The resistance measurements on the Rudolf-Dietze machine were performed using the HIOKI Milliohm-meter. The 'neutral-chip' connecting the three-phase windings in a neutral point on the machine was removed. In order to connect the alligator-clips of the milliohm-meter to the banana-plug connectors on the machine, two small banana-plug cables were used. A measurement series of 10 measurements were used to determine the resistance of the cables. These measurements are listed in table D.1 in appendix D. The sum of the average value of these measurements are listed in table 8.1 below.

The resistance of each of the three-phases on the machine was then measured. A measurement series of 5 measurements per phase were performed, the average of which are listed in table 8.1 below. The per-phase measurement series are listed in appendix D.

The winding resistance was then calculated by subtracting the series resistance of the two cables from the average per-phase resistance value. The resulting armature resistance value is also listed in table 8.1 below.

Table 8.1: Measured resistance values for the measurement cables and three-phase armature windings of the Rudolf-Dietze machine. The resistance values R_U, R_V and R_W are the per-phase measured resistance values, not subtracting the resistance of the cables. R_a is the average of the three-phase resistances presented, with the resistance value of the cables subtracted.

Resistance	Value ($m\Omega$)
R_{cables}	17.9
R_U	232.91
R_V	233.93
R_W	233.03
$\mathbf{R_a}$	**215.39**

The resulting resistance value of $R_a = 215.39m\Omega$ is much more in line with the previously

measured value of $R_a = 218.5m\Omega$ as measured in [11].

Another method for measuring the armature resistance is to consider the real part of the operational impedances, as illustrated in figure 8.6. The armature resistance can be obtained by extrapolating the data of measured points towards zero frequency [7].

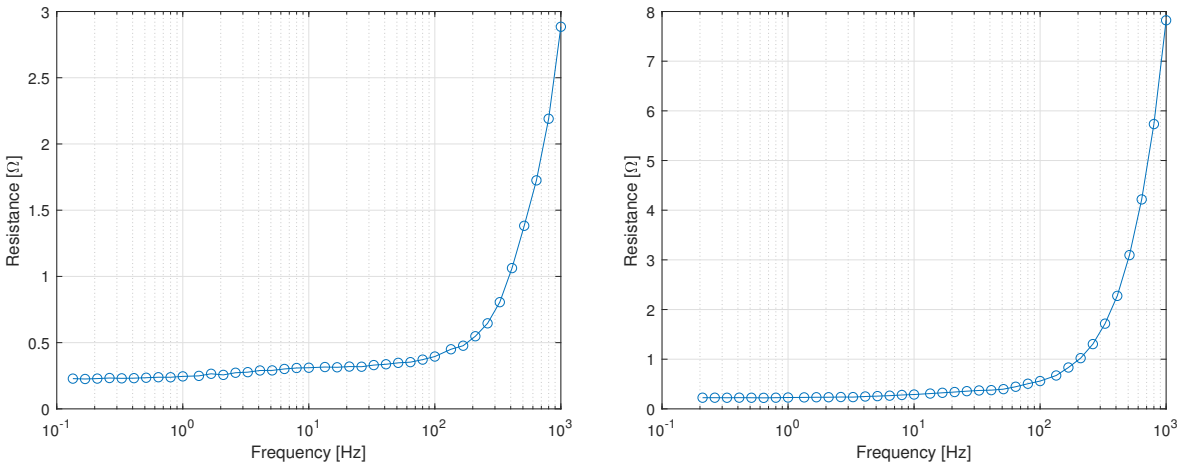

(a) *(b)*

Figure 8.6: Real components of the operational impedances $Z_d(s)$(a) and $Z_q(s)$(b) plotted as a function of frequency. The test data used is from the constant current preliminary tests.

The data was extrapolated using the Curve Fitting App [25] from the MATLAB Curve Fitting Toolbox on test points in the frequency region of <10Hz. The curve fit was performed using the Polynomial fit option and choosing the degree that resulted in the best R-square value. The resulting fit, using a 3rd order polynomial fit, is illustrated in figure 8.7.

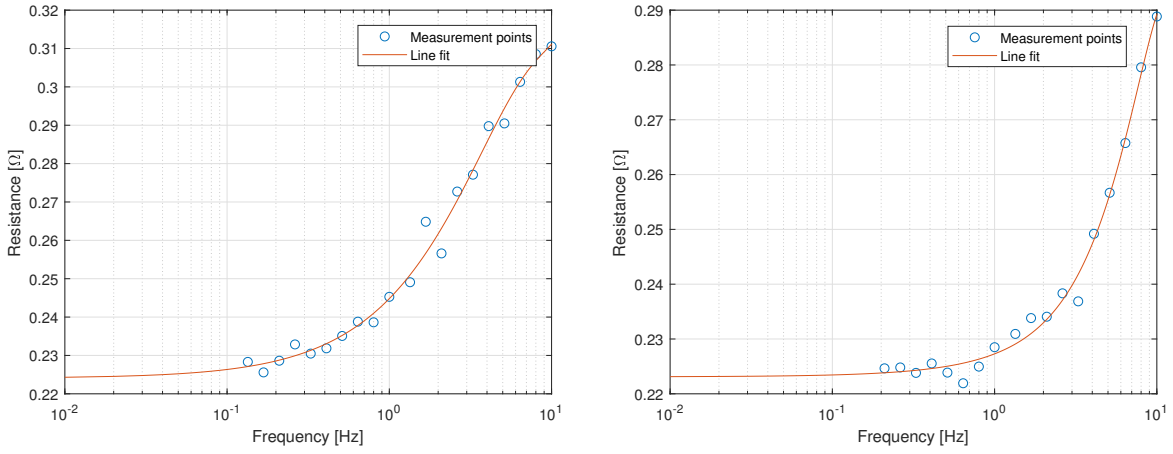

(a) *(b)*

Figure 8.7: Resulting 3rd order curve fit of the real part of the operational impedance constant current preliminary tests. Figure (a) display the curve fit of $Z_d(s)$, while figure (b) shows the $Z_q(s)$ curve fit. The curve fit was performed on test points for frequencies below 10Hz.

When extrapolating the curves to zero frequencies, the resulting values of the armature resistance becomes, $R_{a,d} = 224.3m\Omega$ for the d-axis measurements, and $R_{a,q} = 223.1m\Omega$ for the q-axis. The resulting values differ from each other by approximately 0.5%, and from the measured value for R_a by approximately 3-4%. It is clear that these values differ from the measured value to a relatively large extent. This may be attributed to the fact that the oscilloscope was not able to measure anything for lower frequencies than approximately 0.1Hz. This means that two decades of data that normally would be taken into account, i.e frequencies between 1mHz-0.1Hz, was not part of the data used for the curve fit. This may have caused discrepancies in the resulting extrapolated R_a-values. In combination with the fact that the low frequency measurements are deemed less accurate, as discussed in section 8.1.2, these values are deemed approximate at best.

Therefore, the measured value of the armature resistance value, $\mathbf{R_a = 215.39m\Omega}$, is the per-phase armature resistance value used for further calculations throughout this thesis.

SSFR-tests

The following sections presents the test set-up, measurement results and analysis of the complete set of frequency response characteristics for the operational parameters: $L_d(s)$, $L_q(s)$, $Z_{afo}(s)$ and $sG(s)$.

In order to negate the tests' sensitivity to armature resistance changes, as established from the preliminary test results, the SSFR-tests in these sections were performed using the following conditions:

- The tests were performed using the amplifier and keeping the test current near constant at approximately **150mA**, around 0.5% of the machine's rated current of 26.1A.
- An armature resistance value of $R_a = 215.39m\Omega$ was used in the calculations of the operational impedances $L_d(s)$ and $L_q(s)$.

When recording the measurable parameters for each test, such as armature voltage or current, additional recordings of the accompanying standard deviation value of the associated parameters were also taken. This possibility is enabled by the 'Statistics'-function in the measurement options of the oscilloscope. When averaging the measurements of a waveform over several cycles, all of the oscilloscopes recorded values for each acquisition is saved into one point [30]. The variance in the data set used to calculate the measurement average is represented by a standard deviation value. This value was recorded for all measurable parameters in the tests, except for the armature to field transfer impedance $Z_{afo}(s)$.

The recording of the standard deviation values was made in an attempt at illustrating the spread in the measurement data. When performing calculations using quantities with attached uncertainty values, such as standard deviations, it is important to properly estimate the propagation of uncertainties [34]. The formulas used for calculating error propagation in this thesis is presented in Appendix E.

The measurement data files, including recorded values of accompanying standard deviation values and test frequencies, is presented in Appendix G.

8.3 Direct axis operational inductance, $L_d(s)$

The direct axis operational inductance frequency response characteristics were obtained using the laboratory set-up and connections illustrated in figure 8.1. The rotor was positioned as outlined in section 4.2.4, and the minimum voltage recorded was $e_{fd} = 280\mu V$. The resulting frequency response characteristic is displayed in figure 8.8.

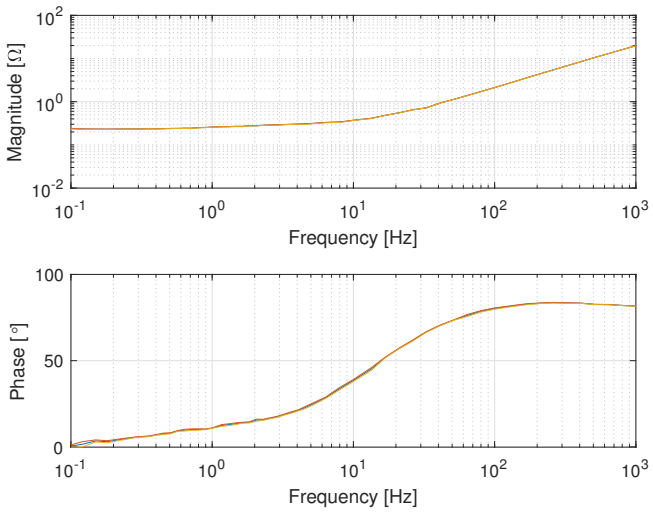

Figure 8.8: Frequency response characteristic of the d-axis operational impedance, $Z_d(s)$, including standard deviation envelope.

The resistive part of the impedance was calculated using the MATLAB-script in Appendix C.1, and the resulting curve is illustrated in figure 8.9a. A 4th degree polynomial fit of the curve was performed using the MATLAB Curve Fitting App [25], the results of which is shown in figure 8.9b.

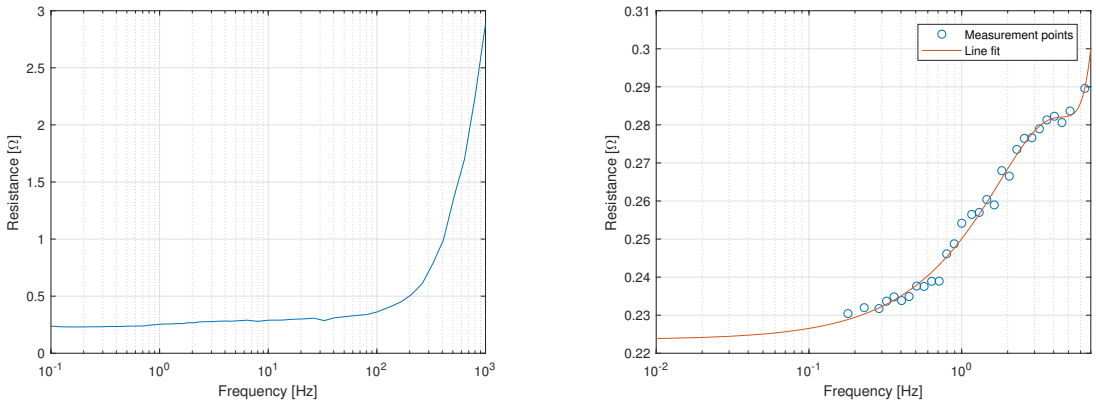

(a) *(b)*

Figure 8.9: Resistive part of the d-axis operational impedance, $Z_d(s)$ (a) and 4th degree polynomial fit of the same curve for frequencies below 10Hz (b).

The extrapolated value of the armature resistance was $R_a = 223.9m\Omega$. This value is a little higher than the measured value of R_a, diverging with approximately 4%. However, as discussed in section 8.2, the extrapolated value is deemed too uncertain to be used in further calculations.

The operational inductance was calculated using the MATLAB scripts as presented in Appendix C.2. The resulting curves are showed in figure 8.10, in addition to standard deviation envelopes. Notice the increased uncertainties in the lower frequency range. As shown in figure 8.11, the uncertainties are larger for lower frequencies, especially the phase measurements, sometimes amounting to as much as 5-10°.

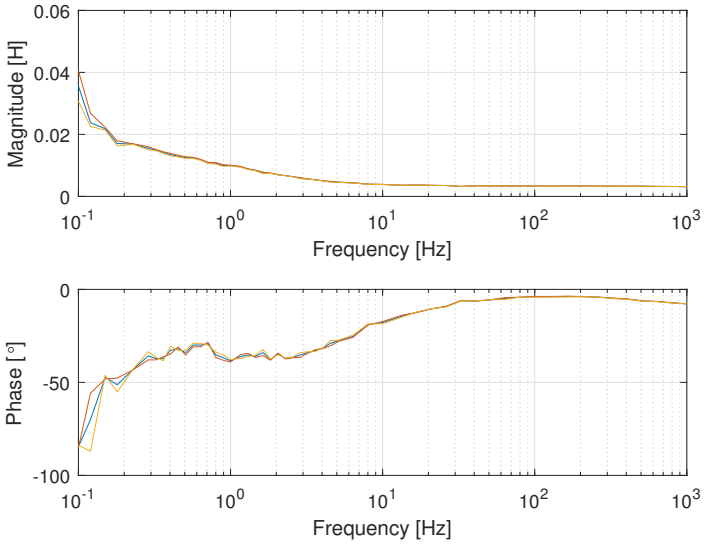

Figure 8.10: Frequency response characteristic of the d-axis operational inductance, $L_d(s)$, including standard deviation envelope.

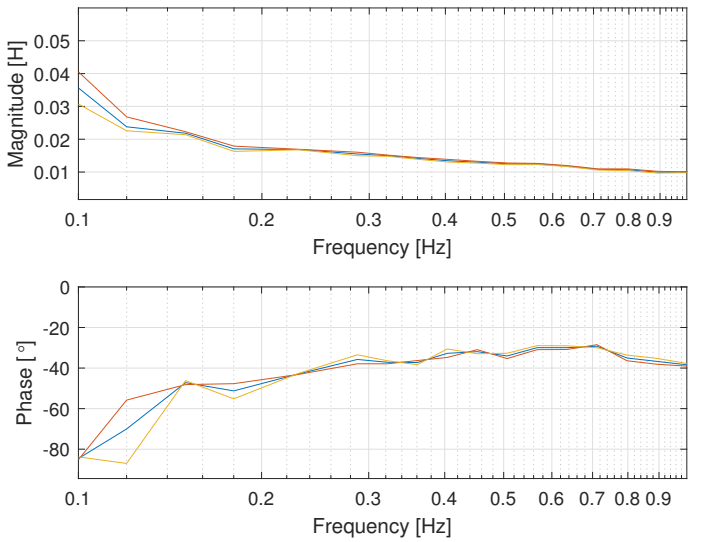

Figure 8.11: The figure illustrates the increased variance in $L_d(s)$ for lower frequencies.

8.4 Quadrature axis operational inductance, $L_q(s)$

The quadrature axis operational inductance frequency response characteristics were obtained using the laboratory set-up shown in figure 8.1 using the q-axis connections. The rotor was positioned following the q-axis rotor alignment procedure as outlined in section 4.2.4. The minimum voltage recorded was $e_{fq} = 350\mu V$. The measured frequency response characteristic is shown in figure 8.12.

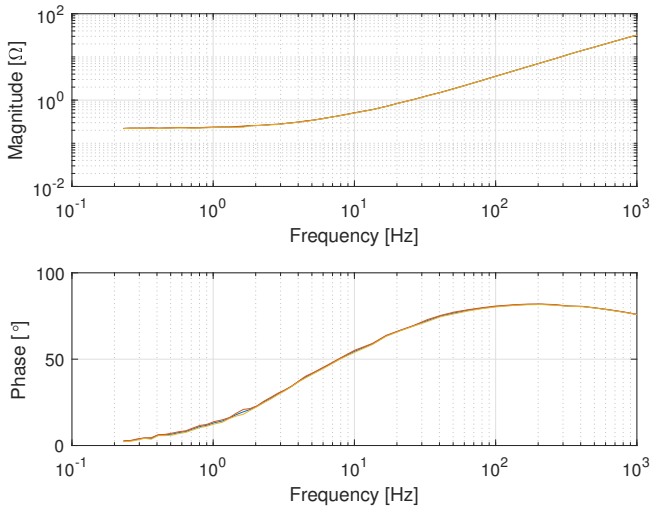

Figure 8.12: Frequency response characteristic of the q-axis operational impedance, $Z_q(s)$, including standard deviation envelope.

In the same way as for the d-axis, the resistive part of the impedance was calculated and extrapolated to zero frequency with a 4th order polynomial fit, as shown in figure 8.13. The resistance value estimate was $R_a = 0.2198$, a 1% difference from the measured value of R_a.

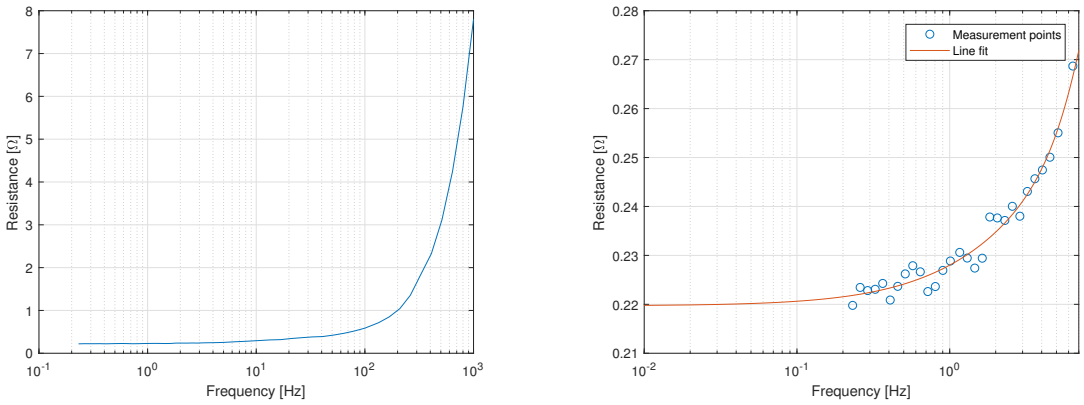

(a) *(b)*

Figure 8.13: Resistive part of the q-axis operational impedance, $Z_q(s)$ (a) and 4th order polynomial fit of the same curve for frequencies below 10Hz (b).

The operational inductance was calculated in the same way as for the d-axis measurements. The resulting frequency response characteristic is displayed in figure 8.14a, while the increased variance for frequencies below 1Hz are accentuated with figure 8.14b. Compared to the d-axis measurements, variations in the q-axis magnitude and phase measurements are significantly greater, and contain much more variance in each measurement point. This is not only true for the measured standard deviation values, but also for variance between measurements. When considering the frequency plots of the d-axis in figure 8.10, both magnitude and phase plots appear much more consistent, resulting in more smooth and even curves than the corresponding q-axis plots illustrated below. These plots, on the other hand, contain a more 'choppy' and uneven nature in the low-frequency region.

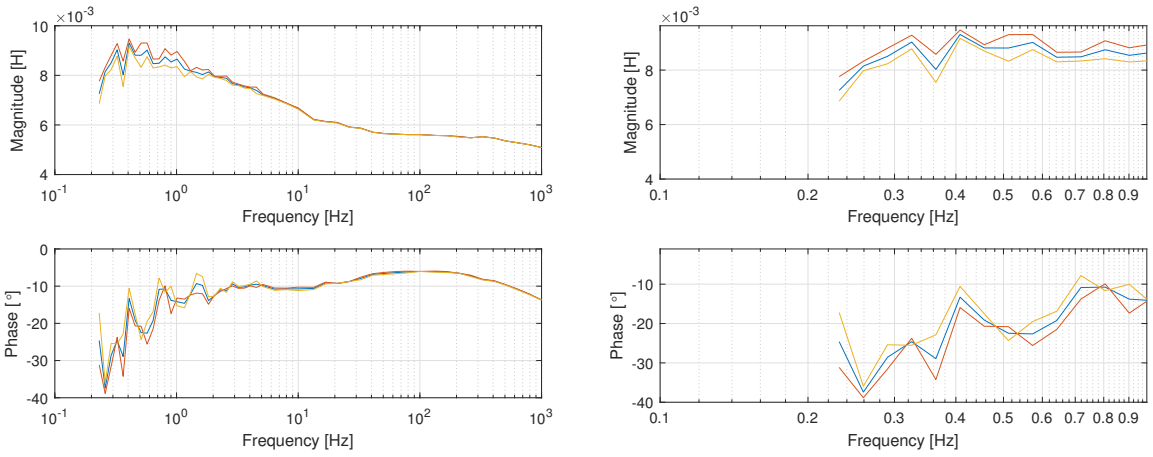

(a) *(b)*

Figure 8.14: Frequency response characteristic of the q-axis operational inductance, $L_q(s)$, including standard deviation envelope (a), and illustration of the increased variance in $L_q(s)$ for lower frequencies(b).

These inconsistencies may come from the fact that the low-frequency test-points in the q-axis was much harder to obtain than for the d-axis, and that greater accuracy when obtaining the test-points in this region is required. In order to demonstrate the inconsistencies when making measurements in this region, another test was made. The operational-inductance for this test is shown in figure 8.15. As illustrated, the same upward- and downward-sloping trends of the $L_q(s)$ magnitude and phase plots seem to be consistent for the two tests. However, the relative large scatter of points in this region indicates low measurement-accuracy.

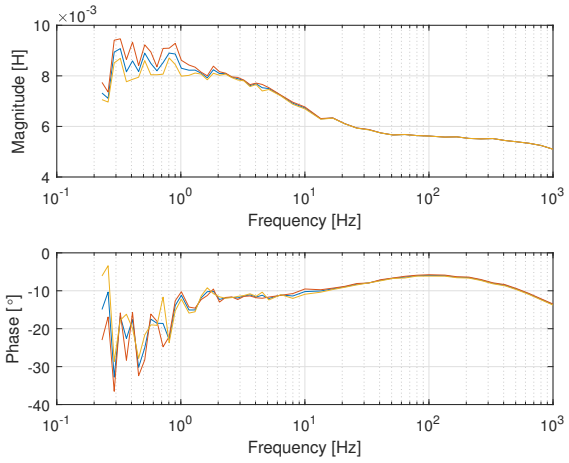

Figure 8.15: q-axis inductance frequency response characteristic for the additional q-axis test, including standard deviation envelope. Notice the scatter of test-points in the low-frequency region.

8.5 Armature-to-field transfer impedance, $Z_{afo}(s)$

The armature-to-field transfer impedance was measured using the test set-up schematically illustrated in figure 8.16, and the rotor aligned for d-axis measurements. The lowest field voltage measured during the alignment was $e_{fd} = 270\mu V$.

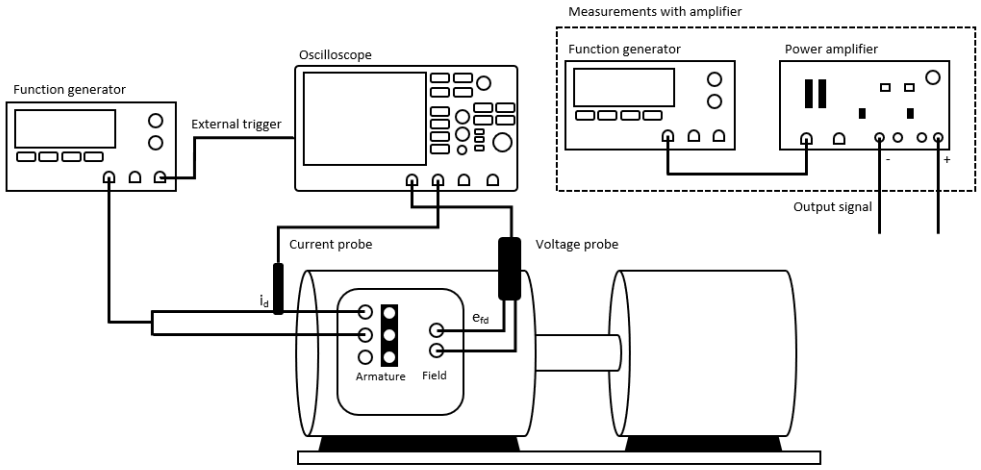

Figure 8.16: Schematic test set-up for the armature-to-field transfer impedance measurements.

The armature-to-field transfer impedance frequency response characteristic was calculated using the MATLAB-script presented in Appendix C.3. The resulting frequency response characteristics are displayed in figure 8.17. The goal of this test is purely to supplement further studies with comparable results. The results of this test is therefore not discussed further.

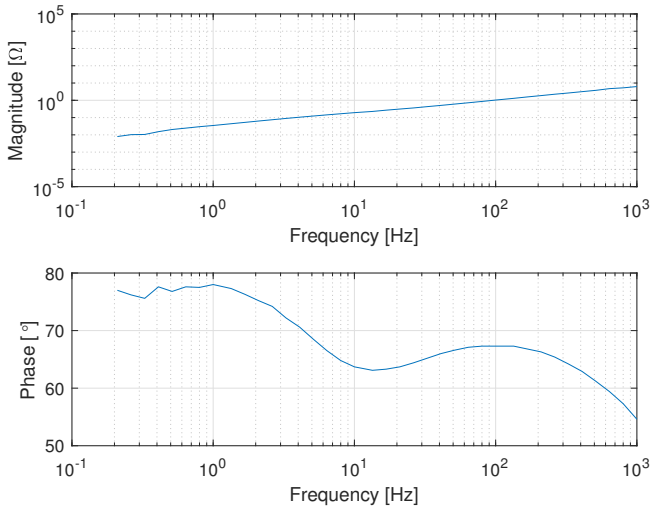

Figure 8.17: Frequency response characteristic for the armature-to-field transfer impedance, Z_{afo}.

8.6 sG(s)-test

The frequency response characteristic of sG(s) was obtained by measuring the field-response with the armature excited, using the test set-up as illustrated in figure 8.18. The rotor was aligned for the d-axis measurements, and the lowest field voltage measured during alignment was $e_{fd} = 150\mu V$.

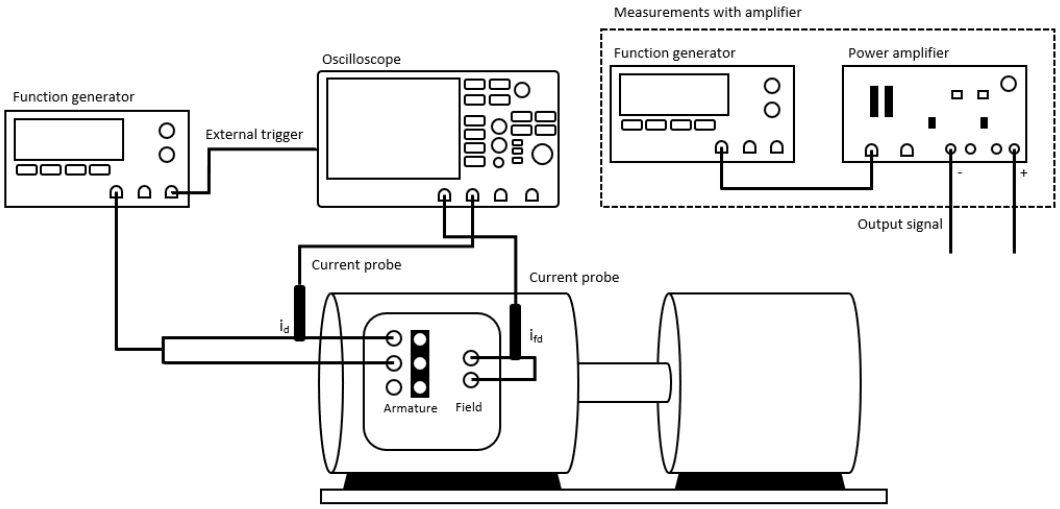

Figure 8.18: Schematic test set-up for the sG(s) measurements.

The magnitude of $sG(s)$ was calculated using the MATLAB-script presented in Appendix C.4. The resulting magnitude- and phase characteristics is illustrated in figure 8.19a. Dividing $sG(s)$ by s, results in the characteristic for $G(s)$, shown in figure 8.19b.

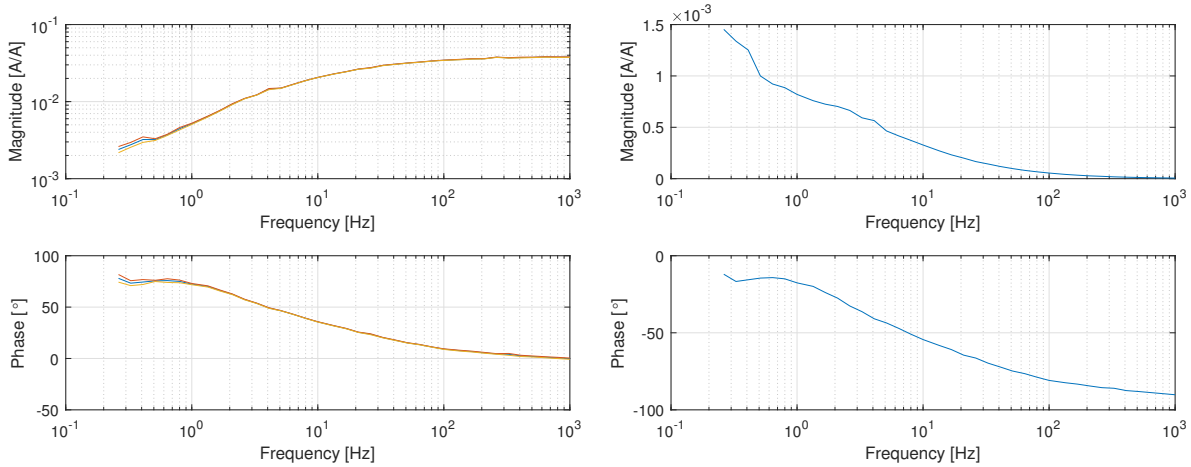

(a) *(b)*

Figure 8.19: Frequency response characteristic for sG(s) (a) and G(s) (b).

Parameter estimation

As illustrated and discussed in the previous sections, the oscilloscope only enables complete measurements of the frequency response characteristic down to between 0.1-1Hz. This is clearly not enough measurements to obtain the complete form of the characteristics, and in extension it is impossible to say anything about the complete set of fundamental parameters. However, with the goal of competence development and to present a practical way of extracting said parameters, it was decided to make an attempt at measuring some of the parameters based on the SSFR-tests performed in the previous sections.

The ensuing sections contain the following:

- **Parameter estimation method** Presentation of the estimation method used.
- **Validation test** The method is validated using a machine with known parameters, as known from [19].
- **Estimation of transient parameters** The method is then performed on the test results for $L_d(s)$, $L_q(s)$ and $G(s)$ in an attempt to estimate some of the transient parameters.

8.7 Parameter estimation method

The estimation method used is based on the transfer function form of the operational parameters, as shown in equations 8.1,8.2 and 8.3, and the corresponding frequency response characteristics. These equations are the same as presented in section 2.4. Two examples of corresponding frequency responses are illustrated in figure 8.20.

$$L_d(s) = L_d \frac{(1 + sT'_d)(1 + sT''_d)}{(1 + sT'_{d0})(1 + sT''_{d0})} \tag{8.1}$$

$$L_q(s) = L_q \frac{(1 + sT'_q)(1 + sT''_q)}{(1 + sT'_{q0})(1 + sT''_{q0})} \tag{8.2}$$

$$G(s) = G_0 \frac{(1 + sT_{kd})}{(1 + sT'_{d0})(1 + sT''_{d0})} \tag{8.3}$$

In order to estimate a transfer function based on the frequency response characteristic, an estimation tool using the 'tfest'-function of the MATLAB System Identification Toolbox was used. The function's output is a transfer function on a rational form, as shown in equation 8.4, based on an input of a set amount of zeros and poles, and frequency-domain measurement data as obtained from the SSFR-tests [23].

$$H(s) = \frac{(1 + sT_1)(1 + sT_2) \cdot \cdot}{(1 + sT3)(1 + sT_4) \cdot \cdot} \tag{8.4}$$

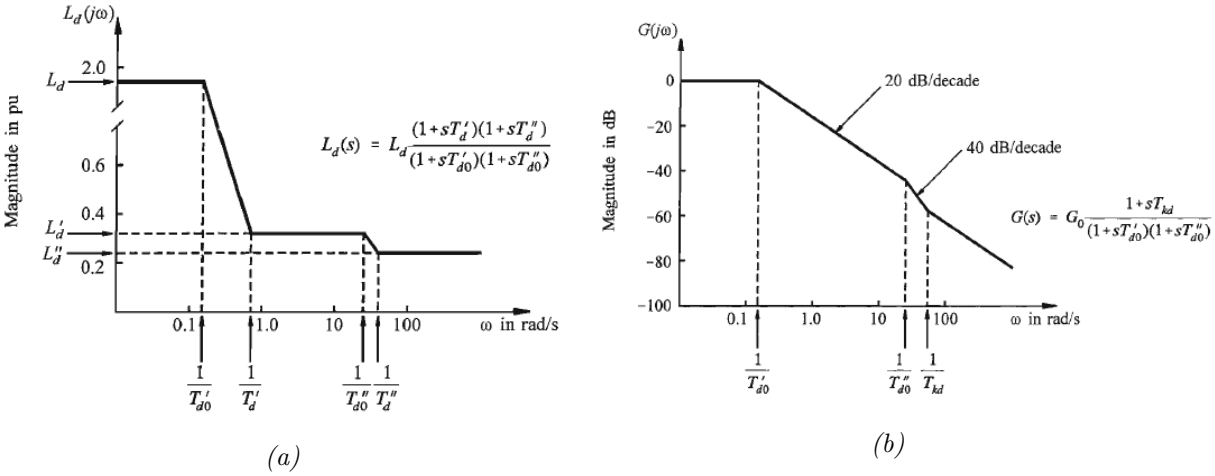

Figure 8.20: Asymptotic approximation of the magnitude plot of $L_d(s)$ (a) and phase plot of $sG(s)$(2) [10]. Notice how the time-constants and the synchronous and transient inductance values govern the characteristic form of the frequency responses.

8.8 Parameter estimation method validation test

In order to validate the estimation method, the parameters of a known machine was used to create frequency response characteristics on which to test the 'tfest'-function. The parameters are listed in table 8.2, and were used to create a bode-plot for the machine. The machine in question is a 55.6MVA salient pole machine tested with SSFR-testing in [19]. The resulting frequency response plot of the machine's d-axis operational inductance is displayed in figure 8.21a.

Using the 'bode'-function, a test-curve was made using vectors containing 100 evenly spread frequency-domain data from the original bode-plot. In order to create more oscillatory test-data, to model the rough measurement data from the tests, noise was added to the frequency-domain vectors. The resulting 'test-curve' is shown in figure 8.21b.

The 'tfest'-function was then applied, creating a second-order estimated fit of the original bode-plot, as shown in figure 8.21c. Resulting time constants and The custom made 'asymp'-function [12] was then used to plot the estimated bode-plot including asymptotic lines, as illustrated in figure 8.21d. For the MATLAB-script used for testing the d-axis operational inductance, $L_d(s)$, see Appendix C.5. Note that the figures presented is just the result of one such test. Several tests were performed by changing the amount of noise and the amount of test-points in the test-curve. Some of these results are presented in table 8.3 and 8.4.

Table 8.2: Parameters of the 55.6MVA salient pole machine [19].

Parameters	Value
T'_d	1.25s
T''_d	0.06s
T'_{d0}	2.82s
T''_{d0}	0.07s
T''_q	0.07s
T''_{q0}	0.12s
L_d	1.19pu
L_q	0.86pu

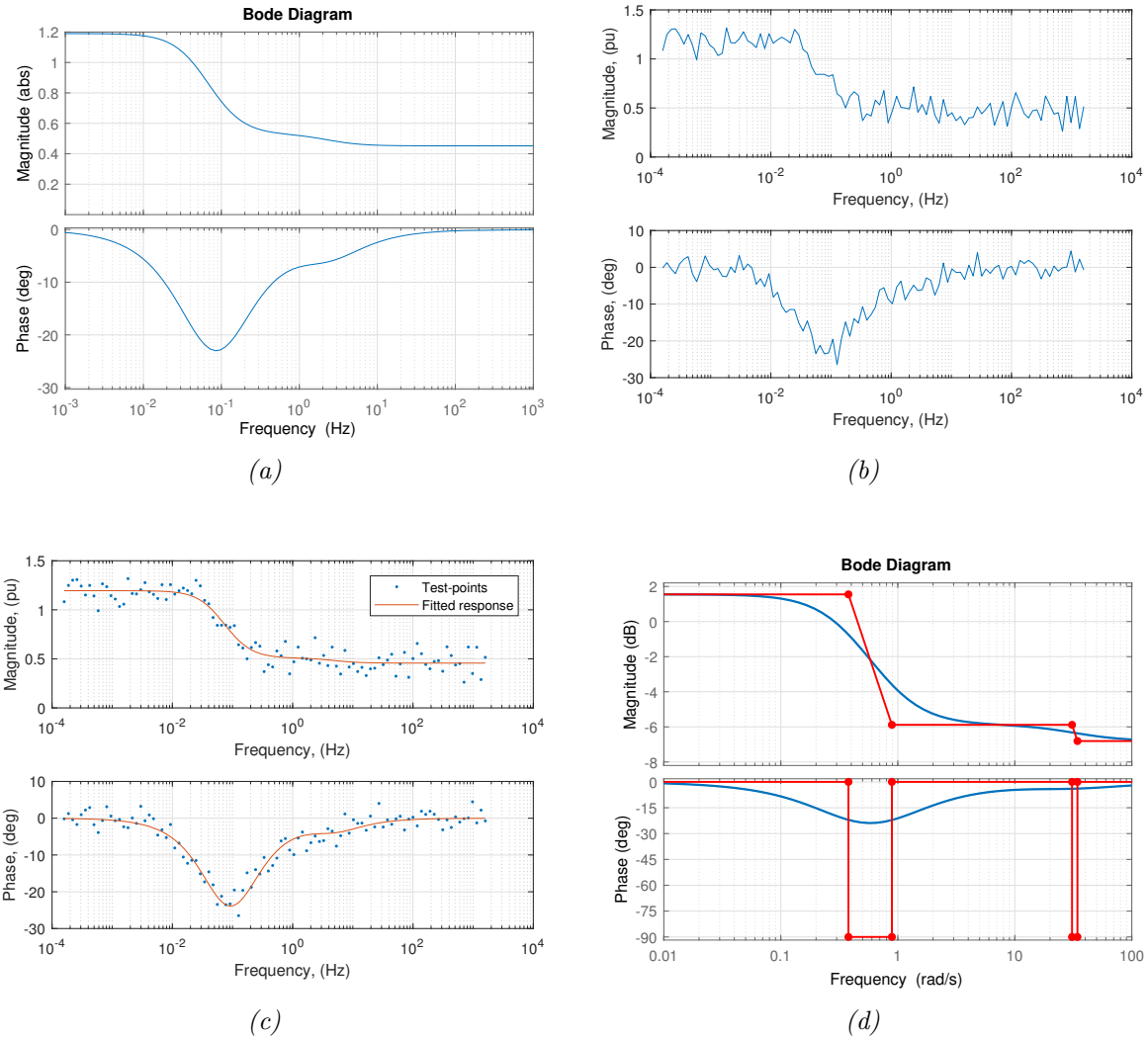

Figure 8.21: a) d-axis operational inductance frequency response, based on the known parameters in table 8.2. b) Test-curve of 100 'measurement'-points, including noise, based on the curve in (a). c) Estimated curve fit for the test-curve in (b) for a second-order model (2 zeros, and 2 poles). d) Asymptotic approximation curves of the estimated frequency response curve in (c).

From the resulting curves in figure 8.21, the estimation method provides a relatively accurate result. The fitted curve in figure 8.21c seems to follow the same trend as the original curve. It seems as long as the 'tfest'-function i provided an input of the correct order of the transfer function being fitted, the results are consistent. For comparison, the fitted line and its accompanying asymptotic bode plot for a third order system, thus introducing subsubtransient quantities, are shown in figure 8.22. In order to produce the best results, the order of the transfer function, i.e the amount of rotor circuits in the machine, should be known.

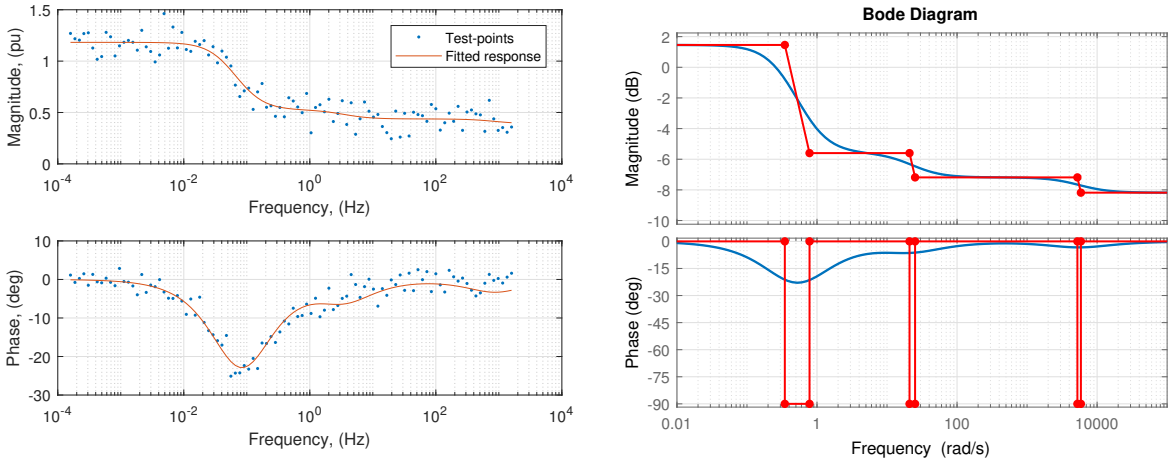

(a) *(b)*

Figure 8.22: 3rd order estimation fit (a) and accompanying 3rd order asymptotic plot (b) of the d-axis operational parameter $L_d(s)$ of the known machine parameters in table 8.2.

The method also produce a more accurate fit for less noisy test-curves, as is shown in table 8.3. This is seen in both the fit-to-estimation data percentage, and in the fit for the different parameters. As the amount of noise reduces, the general trend is that the parameters fit better to the actual measured parameter values shown to the left in the table. This is not true in all cases however. For example, the d-axis subtransient time-constant diverge more from the actual value for Case 2 than for the less noisy Case 3. This can, however, probably be attributed to the fact that the test signal changes between tests due to the randomly generated noise. This is bound to cause such discrepancies. Had the signal been the same for each case, only changing the amplitude of the noise, the results would probably be more accurate for the less noisy signals, which is to be expected.

For the results based on changing the amount of test points in the test-signal, as shown in table 8.4, no certain trends were discovered. An observation based on both tables however, indicate that the subtransient time-constants experience the most relative change between tests. This indicates that these values are most susceptible to variations using this method of parameter determination.

Table 8.3: Estimated d-axis time constants and inductances for 100 measurement points. The numbers in parenthesis represents the maximum amplitude of the noise added to the original bode-plot.

	Original	**Case 1** (0.2pu/3°)	**Case 2** (0.1pu/2°)	**Case 3** (0.05pu/1°)
Fit (%)	-	45.16	71.1	85.4
T'_d (s)	1.25s	1.09	1.34	1.26
T''_d (s)	0.06s	0.025	0.058	0.086
T'_{d0} (s)	2.82s	2.30	3.06	2.8
T''_{d0} (s)	0.07s	0.029	0.064	0.099
L_d (pu)	1.19pu	1.158	1.209	1.186
L'_d (pu)	0.53pu	0.552	0.528	0.535
L''_d (pu)	0.46pu	0.475	0.479	0.464

Table 8.4: Estimated q-axis time constants and inductances for a constant 0.1pu and 1° amplitude on the noise added to the original bode-plot. The numbers in parenthesis represents the amount of test-points in the test-curve.

	Original	**Case 1** (100pt)	**Case 2** (200pt)	**Case 3** (400pt)	**Case 4** (1000pt)
Fit (%)	-	71.1	70.57	69.71	71.51
T'_d (s)	1.25s	1.34	1.18	1.27	1.33
T''_d (s)	0.06s	0.058	0.041	0.04	0.062
T'_{d0} (s)	2.82s	3.06	2.7	2.91	3.01
T''_{d0} (s)	0.07s	0.064	0.05	0.046	0.075
L_d (pu)	1.19pu	1.209	1.19	1.188	1.21
L'_d (pu)	0.53pu	0.528	0.52	0.52	0.533
L''_d (pu)	0.46pu	0.479	0.437	0.452	0.443

8.9 Estimation of transient parameters

It is clear from the resulting frequency plots in sections 8.3, 8.4, 8.5 and 8.6, that it is impossible to obtain the full set of time constants and inductance values using the method described above. This is due to the fact that the frequency plots only provide data for approximately half the desirable frequency range of 1mHz-1kHz. However, the rightmost parts of the frequency plots may be accurate enough to indicate a value for the smallest time constants and some of the transient inductances. The resulting curves from the SSFR-tests for the d- and q-axis inductances, $L_d(s)$ and $L_q(s)$, in addition to $G(s)$, was therefore estimated using the 'tfest'-function as described in the previous section. It should be noted that the results from SSFR-tests was used as input-data for these estimations. In addition, the goal of this is not to obtain accurate values for the different parameters. As already discussed, this is simply impossible with the current range of frequency data. However, the results from these estimations may serve as a baseline from which to compare results for future studies into the SSFR-testing and the parameters of the Rudolf-Dietze machine.

The resulting estimation fit, including asymptotic approximation plots, are shown in figure 8.23 for $L_d(s)$, 8.24 for $L_q(s)$, and figure 8.26 for $G(s)$.

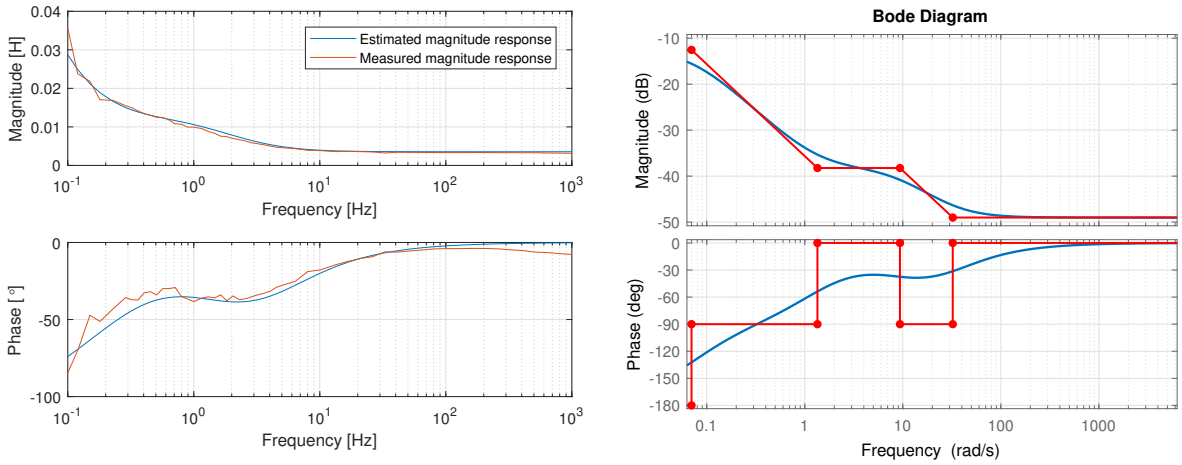

(a) *(b)*

Figure 8.23: 2nd order estimation fit, compared to measured data (a), and accompanying asymptotic plot (b) for the d-axis operational inductance, $L_d(s)$.

For the $L_d(s)$-fit, the 2nd order estimation seems to fit the measured data relatively good, and any time constant or inductances measured above 1Hz can probably be regarded as a good estimate of the respective machine parameters. It is possible, however, that these parameters could be shifted along the frequency axis if the estimation was based on the whole frequency range down to 1mHz. The value obtained here should therefore be regarded as approximate. The resulting time constants and inductances are listed in table 8.5.

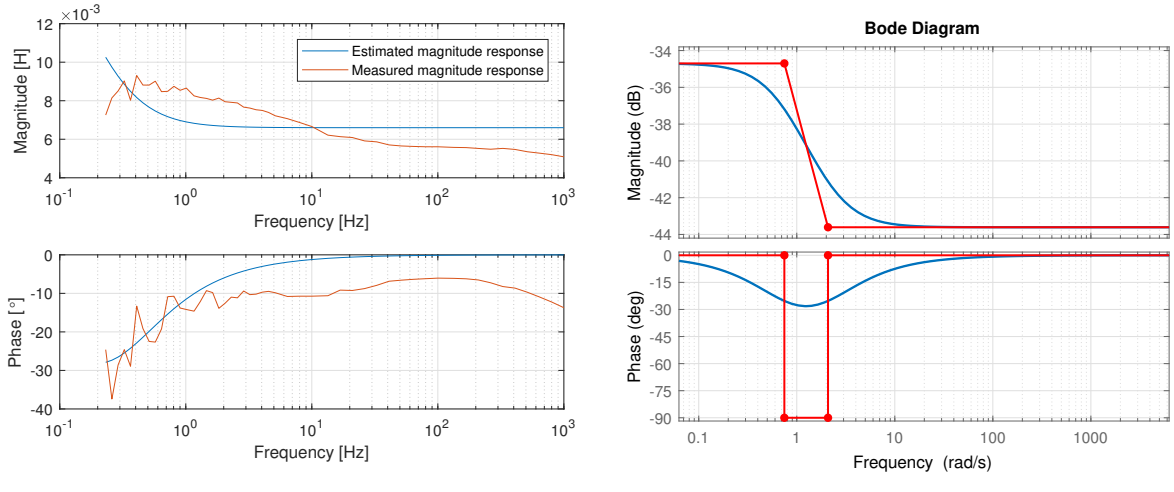

(a) *(b)*

Figure 8.24: 1st order estimation fit, compared to measured data (a), and accompanying asymptotic plot (b) for the q-axis operational inductance, $L_q(s)$.

For the q-axis inductance fit, a 1st order estimation was first applied. The first order fit was used because transient quantities is disregarded in a salient pole machine [10]. However, as figure 8.24 shows, this estimation has a less than satisfactory fit when compared to the measured data. A 2nd and 3rd order estimation was therefore performed, the results of which are presented in figure 8.25. As can be seen, the 3rd order estimation seems the best fit to the measured data. Time constants and inductances for all three cases are listed in table 8.5.

The armature-to-field transfer function, $G(s)$, was estimated using 2 poles and 1 zero for the 'tfest'-function input due to the structure of the function, as shown in equation 8.3. The fit is relatively good, but in the same way as for the $L_d(s)$- and $L_q(s)$-fits, the estimated time constants must be regarded as approximate. The resulting time-constants are listed in table 8.5.

Table 8.5: Estimation of parameters for $L_d(s)$, $L_q(s)$ and $G(s)$ based on the resulting asymptotic approximations.

	$\mathbf{L_q}$	$\mathbf{L''_q}$	$\mathbf{T''_q}$	$\mathbf{T''_{q0}}$		
$L_q(s)$ 1st order fit	18mH	6.6mH	0.4799s	-		
$L_q(s)$ 2nd order fit	8.49mH	5.5mH	0.017s	0.0268		
$L_q(s)$ 3rd order fit	8.58mH	5.75mH	0.0217s	0.0324s		
	$\mathbf{L'_d}$	$\mathbf{L''_d}$	$\mathbf{T''_d}$	$\mathbf{T''_{d0}}$	$\mathbf{T'_{d0}}$	$\mathbf{T_{kd}}$
$L_d(s)$-fit	12.25mH	3.54mH	0.1060s	0.0309s	-	-
G(s)-fit	-	-	-	0.245s	0.2989s	0.115s

To summarize the results from this parameter-estimation exercise, parameters obtained based on the asymptotic approximations should be regarded as approximate at best. The reason for this is due to the fact that it is hard to conclude anything valid based on only partly complete measurement data, and that the estimation function may have a hard time basing its estimations on the less accurate low-frequency measurements.

However, when used on a machine where the whole frequency response is known, the proposed estimation method seems to be able to extract relatively accurate parameter values. This is especially true when the noise in the measurement data, i.e the variance between measurements, is low. For future SSFR-studies, the proposed estimation method may therefore be able to extract relatively accurate parameters when ensuring measurements are taken over the whole frequency range, and that the accuracy of the measurements are satisfactory. The literature proposes that measurements for low frequencies are more susceptible to become less accurate [7, 19, 22]. Where this is the case, several tests may be conducted so that the estimation function may work on a larger data-set. This may mitigate the less accurate low-frequency measurements somewhat.

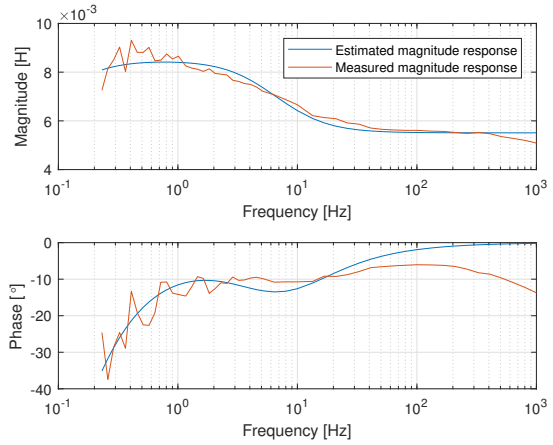

(a)

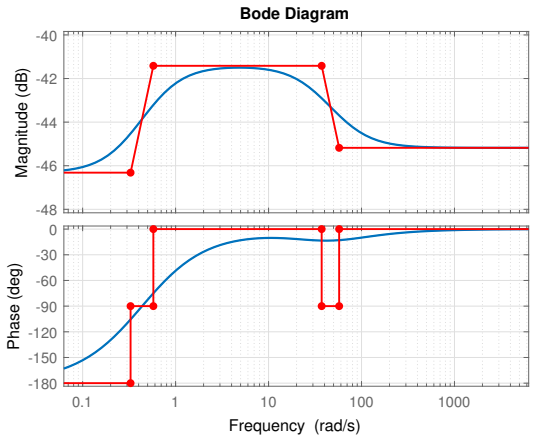

(b)

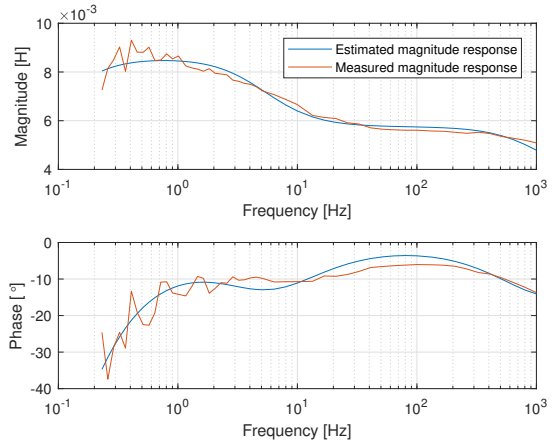

(c)

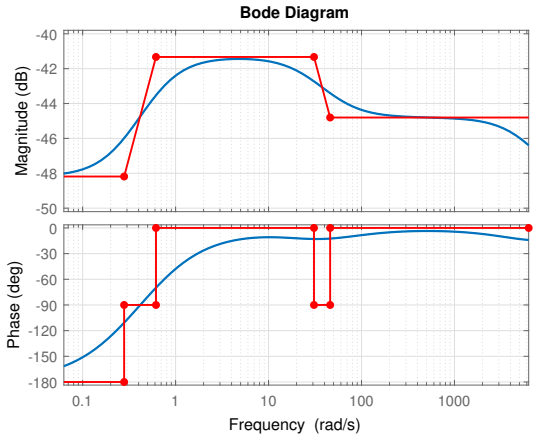

(d)

Figure 8.25: 2nd and 3rd order estimation fit (a and c) and accompanying asymptotic approximation plots (b and d) for the q-axis inductance $L_q(s)$.

8.10 Summary of discussion

During preliminary testing it became apparent that the resulting frequency responses for $L_d(s)$ and $L_q(s)$ was very susceptible to resistance changes in the windings. This both applies to the measured armature resistance, R_a, as well as the resulting magnitude plots of the operational inductances, Z_d and Z_q. In order to mitigate this possible source of error, future studies in SSFR-testing should be performed with more or less constant test-currents. In addition, the care should be taken to measure the armature resistance as accurately as possible.

A parameter estimation method using a MATLAB transfer-function estimation function was used in order to estimate values for the d- and q-axis synchronous and transient inductances as well as transient time constants. The method was validated by being used on a known synchronous machine from [19]. For the best possible estimation results, the SSFR-measurements

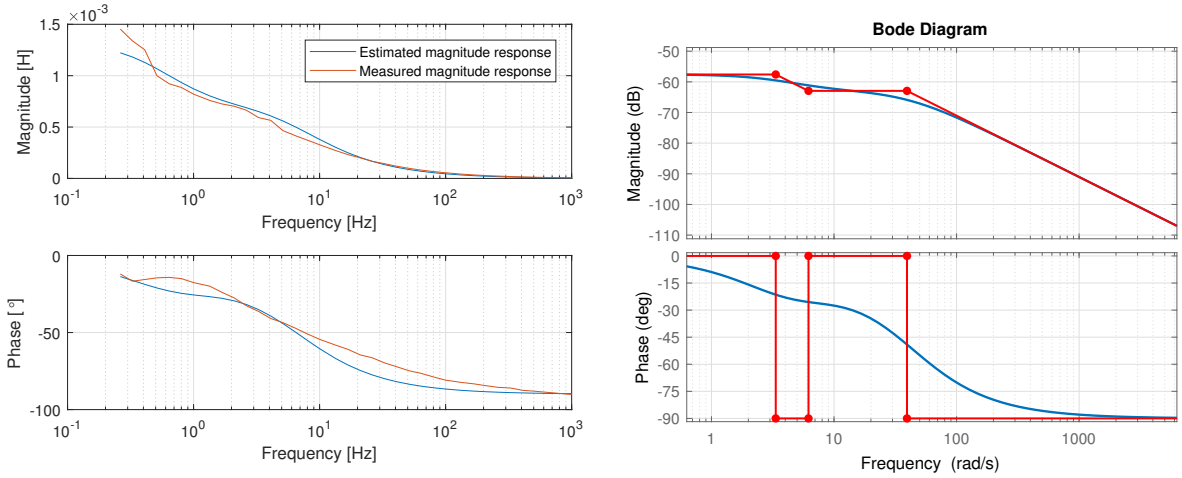

(a) *(b)*

Figure 8.26: Estimation fit of $G(s)$ using 2 poles and 1 zero as input for the 'tfest'-function.

should be performed with as much accuracy as possible. This way, the machine's parameters can be determined relatively accurately. The method was used on the resulting frequency responses for $L_d(s)$, $L_q(s)$ and $G(s)$, however, the resulting estimate must be regarded as approximate at best. This is due to the fact that the measurement data only partly describes the complete frequency response of the parameters in question, and that the measurement data seem less accurate for low frequencies.

The most notable result however, which affected most of the results obtained in this thesis, was the oscilloscope's difficulty obtaining accurate measurements for the whole relevant frequency range of 1mHz-1kHz. Without these limitations, more accurate parameter estimation could probably be obtained. For future SSFR-studies, measurements should be conducted with instruments enabling accurate measurements for the complete frequency range.

Chapter 9

Concluding remarks

This thesis serves as the starting point in the work with parameter identification of the Siemens-Schuckert machine at the National Smart Grid laboratory at NTNU in Trondheim. The motivation is future collaboration studies between NTNU, HydroCen and SINTEF Energy Research regarding the development of hydropower technology. Research objectives include stability studies, synthetic inertia and converter fed operation of synchronous machines [5, 6].

In this thesis, the 75kVA Siemens-Schuckert synchronous machine has been tested, the goal of determining the machine's SCC, OCC, as well as its inherent rotational inertia. The results from the OCC- and SCC-tests are presented in the relevant chapters. In addition, the 8kVA Rudolf-Dietze synchronous machine was tested using the Standstill Frequency Response test in order to validate the test as an alternative to the traditional, but more demanding, sudden short-circuit tests. The SSFR-test has been the main focus of this thesis.

A retardation test was performed in order to determine the inherent rotational inertia of the Siemens-Schuckert machine. Based on the rate of decay of the resulting deceleration curve, the machine's inertia was calculated to be $J = 36.5kgm^2$. This corresponds to an inertial time constant of $H = 2.67s$.

For the SSFR-tests, a laboratory set-up and method of measurement was developed based on available instruments and equipment at the Department of Electrical Power Engineering. Preliminary tests were performed, the results of which affected how the main SSFR-tests were conducted. In addition, a possible parameter estimation method, using a MATLAB estimation function, was presented and validated.

During the preliminary tests it became apparent that the resulting frequency responses was very susceptible to resistance changes in the windings. In order to mitigate this possible source of error, future studies in SSFR-testing should be performed with more or less constant test-currents. In addition, the care should be taken to measure the armature resistance as accurately as possible. The measured per-phase resistance of the machine's armature windings was $R_a = 215.39m\Omega$.

The operational parameters $L_d(s)$, $L_q(s)$ and $sG(s)$, in addition to the armature-to-field transfer impedance, $Z_{afo}(s)$ was measured using the SSFR-test procedure. The test-current was

held approximately constant at $I = 150mA$ for all tests. The oscilloscope used to measure the resulting waveforms had difficulties obtaining measurement for the whole frequency range of 1mHz-1kHz, and approximately 2 decades of measurement data, i.e the frequency range between 1mHz-0.1Hz, was omitted from the tests. In order to identify the complete electrical model of the machine, data for the whole range of frequencies are required. For future SSFR-studies, measurements should be conducted with instruments enabling accurate measurements for the complete frequency range.

To estimate transient inductances and time-constants, an estimation method using a transfer-function estimation function from the MATLAB System Identification Toolbox was used. The method was validated by being used on a known synchronous machine from [19]. Estimates of some of the transient inductances and time-constant in $L_d(s)$, $L_q(s)$ and $G(s)$ was then conducted. The resulting estimate must be regarded as approximate at best, due to low measurement accuracy for low frequencies and incomplete SSFR-test result data. In order to accurately estimate the complete set of the machine's parameters with this method, accurate SSFR-measurements for the whole range of frequencies are required.

9.1 Recommendations for further work

This section discuss recommendations for future studies regarding SSFR-testing, including acquisition of suitable measurement instruments, development of parameter-estimation algorithms and validation studies to validate the machine parameters identified with this kind of testing.

9.1.1 Acquisition of frequency response analyzer

The main result from this thesis is the current available instruments' inability to make accurate measurements for the whole frequency range. Thus, in order to use the methods presented in this thesis to completely identify the machine's parameters, instruments able to make the correct measurements must be acquired. Considerations for such instruments should be the ability of the instrument to make measurements down to the 1mHz-range and with satisfactory measurement resolution. An example of such an instrument, which has reportedly been used in SSFR-testing of a 55.6MVA synchronous machine [19] in the literature, is the frequency response analyzers provided by Ametek Scientific Instruments [35]. The 1260A model incorporates a frequency resolution of 0.015ppm, a frequency range of 15μHz-32MHz, and a magnitude and phase measurement accuracy of 0.1% and 0.1° respectively [36]. Other alternatives may be the Newtons4th Ltd. frequency response analyzers. Similar to Ametek, several variants exist. The PSM1700 model features a 10μHz-35MHz frequency range and an accuracy of 0.02dB and 0.02° for magnitude and phase measurements [37].

In addition, the instrument should be able to produce measurable signals to be used both for

the Rudolf-Dietze and Siemens-Schuckert machines. For the Siemens-Schuckert machine, the rated current of which is 96A, the set-up should be able to produce test-currents up to and above approximately 0.5A for the whole frequency range. An amplifier able to produce this current, based on the input from the frequency response analyzer, and keep the test-current constant for the whole frequency range may also have to be acquired. Lastly, measurement probes used in the set-up must be able to handle the 0.5A test-currents.

9.1.2 Development of parameter-estimation algorithm

The method for parameter estimation used in this thesis is a simple method based on transfer function estimation using the MATLAB System Identification Toolbox. An asymptotic approximation plot of the frequency response of estimated transfer function was used to extract the values of transient inductances and time-constants. This is a simple approach to parameter estimation however, and even though it were not in the scope of this thesis, other approaches to estimating the machine's parameters might be better. In the literature for example, curve-fitting procedures such as Maximum Likelihood Estimation (MLE) is used to completely establish the rotor model [19]. Other curve-fitting algorithms include Levenberg-Marquadt and "Pattern-search"-methods [7]. Development of such an algorithm is therefore suggested if the goal is to obtain more accurate alternatives for transfer-function estimation, and parameter identification.

9.1.3 Validation studies

After acquisition of instruments with the proper measurement specifications, a validation study can be conducted by testing the Rudolf-Dietze machine using SSFR-methodology. In order to validate the SSFR-method, the test results can be compared to the parameters of the machine as identified with the traditional sudden short-circuit test. Parameters for comparison can either be extracted from the results in a Master's thesis from 2017 [11], or from the results of a completely new test-run of the machine, using the traditional short circuit test.

As an alternative, Electromagnetic Transients (EMT) simulation software can be used for model validation. DIgSILENT Powerfactory represents one such software-solution, and should be available for use at the Department of Electrical Power Engineering. By modelling the machine with the resulting SSFR-parameters in the EMT-software, and simulating the machine's response to a sudden no-load three phase short-circuit, the resulting waveforms can be compared to the machine's actual response to the sudden short-circuit. This type of validation study has also been reported in the literature [19].

9.1.4 SSFR-test and validation studies of the Siemens-Schuckert machine

Parameter identification of the Siemens-Schuckert synchronous machine using SSFR-tests can be conducted as soon as instruments with satisfactory measurement specifications are acquired. To ensure the safety of the machine, studies including three-phase short circuits is probably not applicable to the machine. The validation studies described in the previous section is therefore unsuitable, and an alternative way of validating the eventual SSFR-test results must be identified.

Bibliography

[1] Manish Mohanpurkar et al. "Real-time co-simulation of adjustable-speed pumped storage hydro for transient stability analysis". In: *Electric Power Systems Research* 154 (2018), pp. 276–286. ISSN: 0378-7796. DOI: https://doi.org/10.1016/j.epsr.2017.08.010. URL: http://www.sciencedirect.com/science/article/pii/S0378779617303280.

[2] *Norwegian Research Centre for Hydropower Technology - HydroCen*. Accessed 03.06.2019. URL: https://prosjektbanken.forskningsradet.no/#/project/NFR/257588/Sprak=en.

[3] Mostafa Valavi and Arne Nysveen. "Variable-Speed Operation of Hydropower Plants, a look at the past, present and future". In: *IEEE Industry Applications Magazine* (Sept. 2018), pp. 18–27.

[4] *Fakta om HydroCen*. Accessed 03.06.2019. URL: https://www.ntnu.no/web/hydrocen/fakta-om-hydrocen.

[5] Mathias Gallefoss. "Synthetic Inertia from a Converter-Fed Synchronous Machine in a Hydro-Electric Power Plant". MA thesis. 2018.

[6] *Turbine and generators*. Accessed 03.06.2019. URL: https://www.ntnu.edu/hydrocen/turbine-and-generators.

[7] *IEEE Guide: Test Procedures for Synchronous Machines*. Tech. rep. IEEE-SA Standards Board, 2010.

[8] Trond Leiv Toftevaag. Personal conversation. Mar. 2019.

[9] Trond Leiv Toftevaag. *Re: Spørsmål angående motor/generator sett ved NTNU, Trondheim*. [email]. Mar. 2019.

[10] Prabha Kundur. *Power system stability and control*. McGraw-Hill, inc., 1994. ISBN: 0-07-035958-X.

[11] Erik Hildre Bjorkhaug. "Adjustable Speed of Synchronous Machine for Hydro Power Application". MA thesis. 2017.

[12] *Bode plot with asymptotes*. Accessed 25.06.2019. URL: https://se.mathworks.com/matlabcentral/fileexchange/10183-bode-plot-with-asymptotes.

[13] Ion Boldea. *The Electric Generators Handbook: Synchronous generators*. Taylor Francis Group, 2006. ISBN: 0-8493-5725-X.

[14] Stian Jensen Sørås. "Frequency Regulation of Synchronous Generator". MA thesis. 2017.

[15] Jan Machowski, Janusz Bialek, and Dr Jim Bumby. *Power System Dynamics: Stability and Control*. 2nd ed. John Wiley Sons, Ltd., Dec. 2008. ISBN: 978-0-470-72558-0.

[16] Stephen J. Chapman. *Electric Machinery Fundamentals*. 4th ed. McGraw-Hill. ISBN: 0-07-246523-9.

[17] I. D. Ilina. "Experimental determination of moment to inertia and mechanical losses vs. speed, in electrical machines". In: *7th International Symposium on Advanced Topics in Electrical Engineering (ATEE)*. May 2011, pp. 1–4.

[18] Susan A. Riedel James W. Nilsson. *Electric Circuits*. 9th ed. Prentice Hall, 2011. ISBN: 978-0-13-705051-2.

[19] A. Belqorchi et al. "Standstill Frequency Response Test and Validation of a Large Hydrogenerator". In: *IEEE Transactions on Power Systems* 34.3 (May 2019), pp. 2261–2269. ISSN: 0885-8950. DOI: 10.1109/TPWRS.2018.2889510.

[20] A. Keyhani, S. Hao, and R. P. Schulz. "Maximum likelihood estimation of generator stability constants using SSER test data". In: *IEEE Transactions on Energy Conversion* 6.1 (Mar. 1991), pp. 140–154. ISSN: 0885-8969. DOI: 10.1109/60.73801.

[21] S. Bogarra et al. "Detailed Off-Line Parameter Identification of Synchronous Generator Based on Frequency Response Tests". In: *2018 IEEE 18th International Power Electronics and Motion Control Conference (PEMC)*. Aug. 2018, pp. 906–911. DOI: 10.1109/EPEPEMC.2018.8521865.

[22] P.L. Dandeno et al. "Experience with Standstill Frequency Response (SSFR) testing and analysis of salient pole synchronous machines". In: *Energy Conversion, IEEE Transactions on* 14 (Jan. 2000), pp. 1209–1217. DOI: 10.1109/60.815048.

[23] *tfest, Transfer function estimation*. Accessed 25.06.2019. URL: https://se.mathworks.com/help/ident/ref/tfest.html.

[24] Kjell Ljøkelsøy. Personal conversation. June 2019.

[25] *Interactive Curve and Surface Fitting*. Accessed 22.06.2019. URL: https://se.mathworks.com/help/curvefit/interactive-curve-and-surface-fitting-.html.

[26] John Olav Gjæver Tande. "Vindmøllesimulator i vind/diesel-kraftverk. Realisering og testing av kontrollutrustning". MA thesis. 1988.

[27] I. J. Nagrath D. P. Kothari. *Electric machines*. 4th ed. McGraw-Hill Education, 2016. ISBN: 0-07-069967-4.

[28] *AFG31000 Series Arbitrary Function Generator User's Manual*. Tektronix.

[29] *Instruction Manual Four-Quadrant Amplifier TOE 7610*. TOELLNER. 2010.

[30] *RS®RTO Digital Oscilloscope User Manual*. Rohde & Schwarz. 2017.

[31] *80i-110s AC/DC Current Probe Instruction Sheet*. Fluke Corporation. 2005.

[32] *RS®RT-ZC30 Current Probe User Manual*. Rohde & Schwarz. 2017.

[33] *P5200A Series High Voltage Differential Probes Instruction Manual*. Tektronix.

[34] John R.Taylor. *An introduction to Error Analysis*. 2nd ed. University Science Books, 1997. ISBN: 0-935702-42-3.

[35] *Frequency Response Analyzers*. Accessed 01.07.2019. URL: https://www.ameteksi.com/products/frequency-response-analyzers.

[36] *Frequency response analyzers: 1260A Impedance Analyzer*. Accessed 01.07.2019. URL: https://www.ameteksi.com/products/frequency-response-analyzers/1260a-impedance-analyzer.

[37] *Frequency response analyzers*. Accessed 01.07.2019. URL: https://www.newtons4th.com/products/frequency-response-analyzers/.

Appendix A

Per unit equations for a two-rotor-circuit synchronous machine

The equations presented below are all in per unit form, and are used to construct the d- and q-axis equivalent circuits in section 2.3. Note that the following assumptions apply, as explained in section 2.3.

$$L_{ad} = L_{afd} = L_{fda} = L_{akd} = L_{kda} \tag{A.1}$$

$$L_{aq} = L_{akq} = L_{kqa} \tag{A.2}$$

$$L_{fkd} = L_{kdf} \tag{A.3}$$

Stator voltage equations

$$e_d = \frac{d\psi_d}{dt} - \psi_q\omega_r - R_a i_d \tag{A.4}$$

$$e_q = \frac{d\psi_q}{dt} - \psi_d\omega_r - R_a i_q \tag{A.5}$$

$$e_0 = \frac{d\psi_0}{dt} - R_a i_0 \tag{A.6}$$

Stator flux linkage equations

$$\psi_d = -(L_{ad} + L_l)i_d + L_{ad}i_{fd} + L_{ad}i_{1d} \tag{A.11}$$

$$\psi_d = -(L_{aq} + L_l)i_q + L_{aq}i_{1q} + L_{aq}i_{2q} \tag{A.12}$$

$$\psi_0 = -L_0 i_0 \tag{A.13}$$

Rotor voltage equations:

$$e_{fd} = \frac{d\psi_{fd}}{dt} + i_{fd}R_{fd} \tag{A.7}$$

$$0 = \frac{d\psi_{1d}}{dt} - i_{1d}dR_{1d} \tag{A.8}$$

$$0 = \frac{d\psi_{1q}}{dt} - i_{1q}R_{1q} \tag{A.9}$$

$$0 = \frac{d\psi_{2q}}{dt} - i_{2q}R_{2q} \tag{A.10}$$

Rotor flux linkage equations

$$\psi_{fd} = L_{ffd}i_{fd} + L_{f1d}i_{1d} - L_{ad}i_d \tag{A.14}$$

$$\psi_{1d} = L_{f1d}i_{fd} + L_{11d}i_{1d} - L_{ad}i_d \tag{A.15}$$

$$\psi_{1q} = L_{11q}i_{1q} + L_{aq}i_{2q} - L_{aq}i_q \tag{A.16}$$

$$\psi_{2q} = L_{aq}i_{1q} + L_{22q}i_{2q} - L_{aq}i_q \tag{A.17}$$

Appendix B

Derivation of operational parameters

In the ensuing derivation of the operational parameters $L_d(s)$ and $G(s)$, the two-rotor circuit in figures 2.4 and 2.5 are considered, and the mutual inductances L_{f1d} and L_{ad} are considered equal. The following operational form expressions for the d-axis flux linkages can thus be expressed as follows:

$$\psi_d(s) = -L_d i_d(s) + L_{ad} i_{fd}(s) + L_{ad} i_{1d}(s) \tag{B.1}$$

$$\psi_{fd}(s) = -L_{ad} i_d(s) + L_{ffd} i_{fd}(s) + L_{ad} i_{1d}(s) \tag{B.2}$$

$$\psi_{1d}(s) = -L_{ad} i_d(s) + L_{ad} i_{fd}(s) + L_{11d} i_{1d}(s) \tag{B.3}$$

The operational form of the rotor voltages can be expressed as:

$$e_{fd}(s) = s\psi_{fd}(s) - \psi_{fd}(0) + R_{fd} i_{fd}(s) \tag{B.4}$$

$$0 = s\psi_{1d}(s) - \psi_{1d}(0) + R_{1d} i_{1d}(s) \tag{B.5}$$

Here, the $\psi(0)$-terms express initial values of the relevant flux linkages. If the equations above are expressed in incremental values about the steady-state operating point, the initial values can be neglected [10]. Substituting equation B.2 and B.3 into the rotor voltage equations above, while neglecting the initial-value terms, yields:

$$\Delta e_{fd}(s) = -sL_{ad}\Delta i_d(s) + (R_{fd} + sL_{ffd})\Delta i_{fd}(s) + sL_{ad}\Delta i_{1d}(s) \tag{B.6}$$

$$0 = -sL_{ad}\Delta i_d(s) + sL_{ad}\Delta i_{fd}(s) + (R_{1d} + sL_{11d})\Delta i_{1d}(s) \tag{B.7}$$

The two equations above can be solved in terms of e_{fd} and i_d:

$$\Delta i_{fd}(s) = \frac{1}{D(s)}\big((R_{1d} + sL_{11d})\Delta e_{fd}(s) + sL_{ad}(R_{1d} + sL_{1d})\Delta i_d(s)\big) \tag{B.8}$$

$$\Delta i_{1d}(s) = \frac{1}{D(s)}\big(- sL_{ad}\Delta e_{fd}(s) + sL_{ad}(R_{fd} + sL_{fd})\Delta i_d(s)\big) \tag{B.9}$$

where D(s) equals:

$$D(s) = s^2(L_{11d}L_{ffd} - L_{ad}^2) + s(L_{1dd}R_{fd} + L_{ffd}R_{1d}) + R_{1d}R_{fd} \tag{B.10}$$

and

$$L_d = L_{ad} + L_l, \qquad L_{ffd} = L_{ad} + L_{fd}, \qquad L_{11d} = L_{ad} + L_{1d} \tag{B.11}$$

Thus, substituting equations B.8 and B.9 into the incremental form of equation B.1 yields the operational form of the d-axis flux linkage.

$$\Delta\psi_d(s) = G(s)\Delta e_{fd}(s) - L_d(s)\Delta i_d(s) \tag{B.12}$$

Where $L_d(s)$ and $G(s)$ then can be expressed as follows:

$$L_d(s) = L_d\frac{1 + (T_4 + T_5)s + T_4T_6s^2}{1 + (T_1 + T_2)s + T_1T_3^2} \tag{B.13}$$

$$G(s) = G_0\frac{(1 + sT_{kd})}{1 + (T_1 + T_2)s + T_1T_3s^2} \tag{B.14}$$

where

$$G_0 = \frac{L_{ad}}{R_{fd}} \qquad T_{kd} = \frac{L_{1d}}{R_{1d}}$$

$$T_1 = \frac{L_{ad} + L_{fd}}{R_{fd}} \qquad T_2 = \frac{L_{ad} + L_{1d}}{R_{1d}}$$

$$T_3 = \frac{1}{R_{1d}}\Big(L_{1d} + \frac{L_{ad}L_{fd}}{L_{ad} + L_{fd}}\Big) \qquad T_4 = \frac{1}{R_{fd}}\Big(L_{fd} + \frac{L_{ad}L_l}{L_{ad} + L_l}\Big)$$

$$T_5 = \frac{1}{R_{1d}}\Big(L_{1d} + \frac{L_{ad}L_l}{L_{ad} + L_l}\Big) \qquad T_6 = \frac{1}{R_{1d}}\Big(L_{1d} + \frac{L_{ad}L_{fd}L_l}{L_{ad}L_l + L_{ad}L_{fd} + L_{fd}L_l}\Big)$$

$L_q(s)$ can be written exactly as $L_d(s)$, but changing the damper and field annotations with the second and first damper circuit annotations respectively. For example, R_{fd} becomes R_{1q} and R_{1d} becomes $R_{2}q$ [10].

Appendix C

Data processing and MATLAB-scripts

The following appendix lists all relevant MATLAB-scripts used for data processing of the test results. Note that some parameters that are defined in the MATLAB-code may have changed during the data-processing step and when retrieving results to be used in this thesis. For example, the armature resistance value, R_a, listed in some of the MATLAB-scripts below may have changed during different tests. What armature value was used during the different tests are described in the relevant part of the thesis.

C.1 Calculations of $Z_d(s)$ and $Z_q(s)$

```
%% Calculation of Zd/q
%Varm and Iarm are vectors containing the measured values
%of the armature voltages and currents respectively.

Z=(1/2).*(50*Varm./Iarm);   %Varm is multiplied with 50 due
                            %to attenuation of voltage probe.

%% Estimating the Armature resistance, Ra
%Ra is estimated by plotting Re[Z] and extrapolating
%to zero frequency.

Z_cplx=(Z.*cos(PHASE)+1j.*Z.*sin(PHASE));
Z_real=real(Z_cplx);
figure()
semilogx(F,Z_real,'-o');
xlabel('Frequency [Hz]')
ylabel('Resistance [\Omega]')
```

C.2 Calculations of $L_d(s)$ and $L_q(s)$

```
%% Calculate and plot Ld/q(s)
%Calculating Ld/q(s) by L(s)=(Z(s)-Ra)/s. PHASE and F are
%vectors containing the measured phase-shift (in radians)
%at the different frequencies in F.

Ra=0.21539;                          %Armature resistance (ohm)
L_cplx=(Z.*cos(PHASE)+Z.*1j.*sin(PHASE)-Ra)./(1j*2*pi().*F);
L_abs=abs(L_cplx);                       %magnitude of L(H)
L_angle=angle(L_cplx).*(180/pi());   %phase angle of L (degrees)
```

C.3 Calculation of $Z_{afo}(s)$

```
%% Calculation of Zafo(s)
Zafo=cos(30*pi()/180).*(Vfd./Iarm);
```

C.4 Calculation of $sG(s)$ and $G(s)$

```
%% Calculation of sG(s)
sG=cos(30*pi()/180).*(Ifd./Iarm);


%% Calculation of G(s)
sG_cplx=cos(30*pi()/180).*(Ifd./Iarm).*exp(1j*PHASE);
G_cplx=sG_cplx./(1j*2*pi().*F);
G_abs=abs(G_cplx);
G_angle=angle(G_cplx).*(180/pi());
```

C.5 Parameter estimation validation test

```
%% Parameter estimation validation test
%The following code tests the validity of the 'tfest'-function.
%% Known synchronous generator
%The parameters below are the parameters of a known machine
%estimated using the SSFR-test.
Tdi=1.25;       %Td'
Tdii=0.06;      %Td''
Td0i=2.82;      %Tdo'
Td0ii=0.07;     %Td0''
Tqii=0.07;      %Tq''
Tq0ii=0.12;     %Tq0''
Ld=0.3;   %pu
Lq=0.86;  %pu

s=tf('s');          %Initialize transfer function
w=logspace(-3,4,1000);  %frequency vector

%% Original bode plot
%A bode plot is generated based on the known machine parameters.
Ld_s=(Ld*(1+s*Tdi)*(1+s*Tdii))/((1+s*Td0i)*(1+s*Td0ii));
bodeplot(Ld_s)
h=bodeplot(Ld_s);
setoptions(h,'FreqUnits','Hz', 'MagUnits', 'abs' , 'Xlim',
   [0.001, 1000], 'MagLowerLimMode', 'manual', 'MagLowerLim',
   0.00001) ;


%% Generate 'test-points'
%The following code extracts 1000 points of frequency-domain
   data in
%three vectors.
[MAG,PHASE,W] = bode(Ld_s, w);
MAG=reshape(MAG(:,:,:),1,1000);
PHASE=reshape(PHASE(:,:,:),1,1000);
W=transpose(W(:,:,:));


%% Noise generator
```

```
%Noise is generated by adding a random number between 0-1 to the
%frequency-domain data vectors.
sig=0.01;
noise_mag=sig*randn(size(MAG));
noise_phase=randn(size(PHASE));
MAG=MAG+noise_mag;          %Magnitude vector including noise
PHASE=PHASE+noise_phase;    %Phase vector including noise



%% Estimate transfer function
data = frd(MAG.*exp(1j*PHASE*pi/180),W);    %create a frequency
                        %response data mode 'data' the complex
                        %form r*e^theta where theta is the
                        %angle in rads.
Np=2;    %Number of poles
Nz=2;    %Number of zeros
sys = tfest(data,Np,Nz)      %estimate transfer function
                            %parameters for a transfer function
                            %with tfest(data,np,nz) np poles
                            %and nz zeros.
figure()
h=bodeplot(sys);
setoptions(h,'FreqUnits','Hz', 'MagUnits', 'abs' , 'Xlim',
   [0.001, 1000], 'MagLowerLimMode', 'manual', 'MagLowerLim',
   0.00001) ;
grid on

%% Estimated bode-plot
%A bode-plot is constructed based on the estimated
%transfer function fit.
g=tf(sys.Numerator,sys.denominator);

[Mag_est,Phase_est,W_est] = bode(g,W);
F_est = W_est/(2*pi);

Mag_est=reshape(Mag_est,[],1);
Phase_est=reshape(Phase_est,[],1);
F_est=reshape(F_est,[],1);

%Create a figure with two plots, the magnitude and phase as a
```

```
75 %function of frequency
76 subplot(2,1,1);
77 semilogx(F_est,MAG, F_est, Mag_est);
78 grid on
79 subplot(2,1,2);
80 semilogx(F_est,PHASE, F_est, Phase_est);
81 grid on
82
83
84 %% Create asymptotic plot
85 %The code creates an asymptotic plot based on the
86 %estimated transfer function fit.
87 figure()
88 asymp(sys)
```

Appendix D

Resistance measurements

Table D.1: Resistance measurements of measuring cables used for measuring the Rudolf-Dietze machine's armature resistances.

Measurement nr.	**Cable 1** ($m\Omega$)	**Cable 2** ($m\Omega$)
1	11.4	8.0
2	11.3	7.3
3	11.2	6.7
4	11.2	6.5
5	8.6	7.6
6	12.6	6.8
7	10.0	8.2
8	8.5	8
9	9.2	6.6
10	7.6	7.3
Avg.	**10.16**	**7.3**

Table D.2: Per-phase resistance measurements of the Rudolf-Dietze armature windings.

Measurement nr.	**U** ($m\Omega$)	**V** ($m\Omega$)	**W** ($m\Omega$)
1	233.00	234.16	233.10
2	232.86	233.80	232.98
3	232.90	233.90	233.01
4	232.86	233.76	232.96
5	232.95	234.03	233.1
Avg.	**232.91**	**233.93**	**233.03**

Appendix E

Error propagation

Consider a set of quantities, x,....,z, that are measured with uncertainties in the form of standard deviations Δx,...,Δz and used to compute the function q(x,....,z). Then the propagated uncertainty in q can be generally written as [34]:

$$\Delta q = \sqrt{\left(\frac{\partial q}{\partial x}\Delta x\right)^2 + \cdots + \left(\frac{\partial q}{\partial z}\Delta z\right)^2} \tag{E.1}$$

The following sections outline the calculation of standard deviations for the different operational parameter functions.

E.1 $Z_d(s)$ and $Z_q(s)$

Z_i depends on two parameters, e_a and i_a, with accompanying uncertainties Δe_a and Δi_a. Z_i can be written as follows:

$$Z_i(s) = \frac{1}{2}\frac{e_a}{i_a} \tag{E.2}$$

Thus, when using equation E.1, the uncertainty ΔZ_i can be written as:

$$\Delta Z_i = \sqrt{\left(\frac{1}{2}\frac{1}{i_a}\Delta e_a\right)^2 + \left(\frac{1}{2}\frac{e_a}{i_a^2}\Delta i_a\right)^2} \tag{E.3}$$

E.2 $Z_{afo}(s)$ and $sG(s)$

$Z_{afo}(s)$ and $sG(s)$ are equal in the sense that their mathematical expressed by a fraction, multiplied with the constant $\cos 30°$. Their uncertainties are therefore calculated the same

way. $Z_{afo}(s)$ and $sG(s)$ depend on the parameters e_{fd} and i_d, or i_{fd} and i_d , respectively.

$$Z_{afo}(s) = \frac{\cos 30° e_{fd}}{i_d} \tag{E.4}$$

$$sG(s) = \frac{\cos 30° i_{fd}}{i_d} \tag{E.5}$$

Thus, their uncertainties, ΔZ_{afo} and ΔsG can be written as follows:

$$\Delta Z_{afo} = \sqrt{\left(\frac{\cos 30°}{i_d}\Delta e_{fd}\right)^2 + \left(\frac{\cos 30° e_{fd}}{i_d^2}\Delta i_d\right)^2} \tag{E.6}$$

$$\Delta sG = \sqrt{\left(\frac{\cos 30°}{i_d}\Delta i_{fd}\right)^2 + \left(\frac{\cos 30° i_{fd}}{i_d^2}\Delta i_d\right)^2} \tag{E.7}$$

E.3 $L_d(s)$ and $L_q(s)$

L_i is a complex quantity that depends on the complex function $Z_i = Ze^{i\phi}$ witch accompanying uncertainties, ΔZ and $\Delta\phi$. L_i is written as follows:

$$L_i = \frac{Z_i(s) - R_a}{s} \tag{E.8}$$

Using equation E.1 yields the following:

$$\Delta L_i = \sqrt{\left(\frac{\partial}{\partial r}\Big(\frac{Ze^{i\phi} - R_a}{s}\Big)\Delta Z\right)^2 + \left(\frac{\partial}{\partial \phi}\Big(\frac{Ze^{i\phi} - R_a}{s}\Big)\Delta\phi\right)^2} \tag{E.9}$$

$$= \sqrt{\left(\frac{e^{i\phi}}{s}\Delta Z\right)^2 + \left(\frac{iZe^{i\phi}}{s}\Delta\phi\right)^2} \tag{E.10}$$

$$= \sqrt{\left(\frac{\Delta Z^2 - Z^2\Delta\phi^2}{s^2}\right)e^{i2\phi}} \tag{E.11}$$

$$= \underline{\frac{\sqrt{\Delta Z^2 - Z^2\Delta\phi^2}}{s}\Big(\cos(\phi) + i\sin(\phi)\Big)} \tag{E.12}$$

The complex quantity, L_i, can then be expressed as $Re\{L_i\} + Im\{L_i\} \pm Re\{\Delta L_i\} \pm Im\{\Delta L_i\}$. Note that $\Delta\phi$ in the expressions above must be in radians.

Appendix F

Preliminary test measurement data

Table F.1: Measurement data for the base test for $Z_d(s)$.

Va (mV)	**Ia (mA)**	**Phase (°)**	**Frequency(Hz)**
114.4	144.7	81.5	1000
100	155.63	81.9	800
85.8	164.5	82.4	640
73.1	171.4	82.6	512
61	177.4	82.9	410
50.2	182.3	83.3	328
40.7	185.3	83.5	262
33.6	187.3	82.7	210
27.4	189.2	82.2	168
22.3	190.2	81.3	134
16.8	190.8	79.5	100
13.6	191	77.5	80
10.9	190.2	75.9	64
8.9	189.2	72.5	51
7.3	188.2	68.2	41
6.1	186.3	63.9	33
5	184.3	59	26
4.2	180.3	54.3	21
3.6	175.4	49.4	17
3	165.5	43.2	13
2.5	152.7	37.7	10
2.2	138.8	32.6	8.00
1.9	124	29.4	6.40
1.6	107.7	26	5.12
1.3	91.4	23.7	4.10
1	76.6	20.7	3.28
0.87	63	21.3	2.62
0.7	51.6	19	2.10
0.52	41.8	18.3	1.68
0.42	33.8	18	1.34

Table F.2: Measurement data for the constant current test for $Z_d(s)$.

Va (mV)	**Ia (mA)**	**Phase (°)**	**Frequency(Hz)**
119.570	153.160	81.5	1000
107.710	168.970	82.1	800
92.095	176.500	82.4	640
68.340	161.340	82.5	512
51.779	152.670	82.8	410
40.119	147.430	83.2	328
35.970	164.860	83.2	262
27.964	157.610	82.9	210
23.850	167.570	82.3	168
18.020	156.620	81.0	134
13.880	161.560	79.4	100
10.710	154.640	77.6	80
9.430	168.480	75.4	64
7.430	163.400	72.2	51
5.820	154.840	69.0	41
4.950	158.800	64.9	33
4.050	158.600	60.1	26
3.610	162.530	54.9	21
3.130	160.570	49.9	17
2.670	155.340	42.7	13
2.450	157.710	36.9	10
2.240	153.750	32.1	8.00
2.200	160.870	28.2	6.40
1.890	146.570	25.7	5.12
1.980	157.710	22.6	4.10
1.620	136.350	21.1	3.28
1.840	159.290	19.2	2.62
1.670	153.750	19.1	2.10
1.700	152.960	17.6	1.68
1.560	151.380	14.8	1.34
1.590	157.110	14.2	1.00
1.380	141.200	12.4	0.80
1.450	149.210	10.6	0.64
1.540	161.480	9.6	0.51
1.410	150.800	7.3	0.41
1.360	146.450	6.9	0.33
1.470	157.260	4.8	0.26
1.390	151.680	3.7	0.21
1.380	152.700	3.2	0.17
1.070	117.090	2.0	0.13

Table F.3: Measurement data for the high current test for $Z_d(s)$.

Va (mV)	**Ia (mA)**	**Phase (°)**	**Frequency(Hz)**
200.110	251.980	81.3	1000
168.480	259.880	81.7	800
135.960	259.880	82.2	640
104.160	245.990	82.5	512
88.430	255.930	82.7	410
71.620	259.880	82.9	328
56.818	255.930	82.8	262
44.860	253.950	82.7	210
36.067	255.930	81.9	168
28.162	253.700	82.1	134
21.890	253.860	80.3	100
17.885	255.930	78.1	80
14.140	251.980	76.1	64
11.550	252.800	72.9	51
9.780	257.910	69.8	41
8.020	257.910	66.0	33
6.818	261.860	60.9	26
5.968	263.830	55.6	21
5.010	255.430	50.6	17
4.387	256.400	43.9	13
4.010	261.860	38.1	10
3.610	255.930	33.1	8.00
3.250	238.380	28.3	6.40
3.240	250.000	24.7	5.12
3.300	263.830	21.7	4.10
3.040	252.020	19.8	3.28
3.004	257.910	17.4	2.62
2.869	253.950	16.0	2.10
2.690	250.000	14.8	1.68
2.645	249.100	13.5	1.34
2.562	250.000	12.1	1.00
2.490	250.000	10.6	0.80
2.450	251.980	9.6	0.64
2.360	250.090	8.8	0.51
2.350	251.980	7.8	0.41
2.480	269.370	6.5	0.33
1.390	151.080	5.2	0.26
1.240	136.360	4.0	0.21
1.010	111.660	3.8	0.17
0.816	87.950	2.8	0.13

Table F.4: Measurement data for the base test for $Z_q(s)$.

Va (mV)	**Ia (mA)**	**Phase (°)**	**Frequency(Hz)**
140.810	113.440	76.6	1000
129.690	126.880	77.8	800
116.130	139.550	79.2	640
104.730	152.150	80.1	512
90.614	162.450	81.1	410
77.069	171.150	81.9	328
65.214	178.260	82.2	262
53.921	183.000	83.0	210
44.451	186.890	83.2	168
36.234	189.330	83.2	134
27.620	191.700	82.7	100
22.360	192.490	81.9	80
18.155	192.490	80.5	64
14.560	191.710	78.8	51
11.910	190.910	77.1	41
9.650	189.340	74.9	33
7.816	186.620	70.3	26
6.390	183.000	67.1	21
5.220	177.500	63.7	17
4.020	168.100	59.6	13
3.110	155.340	55.3	10
2.500	141.900	49.8	8.00
1.960	126.090	45.6	6.40
1.490	105.700	41.5	5.12
1.200	91.897	36.3	4.10
0.882	76.887	34.2	3.28
0.734	63.439	27.9	2.62
0.571	51.976	25.0	2.10
0.434	42.194	20.9	1.68
0.386	33.805	16.4	1.34
0.294	25.490	14.5	1.00
0.222	20.356	17.3	0.80

Table F.5: Measurement data for the constant current test for $Z_q(s)$.

Va (mV)	**Ia (mA)**	**Phase (°)**	**Frequency(Hz)**
196.150	152.700	75.9	1000
161.560	153.660	77.4	800
131.600	154.210	78.6	640
108.130	156.130	79.7	512
84.783	152.170	80.6	410
69.330	154.550	81.2	328
56.640	156.770	81.7	262
44.565	153.750	81.9	210
36.130	154.720	81.8	168
28.780	154.550	81.7	134
21.420	152.960	80.8	100
17.560	155.160	79.7	80
14.050	154.550	78.7	64
11.250	154.550	77.4	51
9.340	156.130	75.4	41
7.770	157.710	72.5	33
6.290	154.550	69.5	26
5.410	158.500	66.6	21
4.520	156.920	63.3	17
3.620	152.170	58.8	13
3.060	154.550	54.3	10
2.730	156.920	50.0	8.00
2.440	157.710	46.6	6.40
2.110	152.960	41.9	5.12
1.907	152.600	37.1	4.10
1.730	152.960	33.1	3.28
1.650	152.960	27.9	2.62
1.630	159.290	23.8	2.10
1.490	149.800	19.9	1.68
1.510	156.900	16.3	1.34
1.460	156.130	12.2	1.00
1.390	151.980	10.3	0.80
1.380	153.750	8.5	0.64
1.380	152.960	7.0	0.51
1.400	154.570	5.1	0.41
1.340	149.060	5.2	0.33
1.380	153.240	3.1	0.26
1.390	154.550	2.4	0.21

Appendix G

SSFR-test measurement data

Table G.1: Measurement data for the armature to field transfer impedance $Z_{afo}(s)$.

Vf (mV)	**Ia (mA)**	**Phase (°)**	**Frequency(Hz)**
1094.900	151.680	54.6	1000
928.850	152.670	57.3	800
796.440	145.550	59.4	640
650.200	149.230	61.2	512
563.240	153.750	62.9	410
456.520	149.010	64.2	328
412.060	158.500	65.4	262
327.080	151.200	66.3	210
281.620	155.340	66.8	168
230.730	153.710	67.3	134
187.3	156.920	67.3	100
152.670	153.750	67.3	80
126.980	152.960	67.1	64
107.910	154.550	66.6	51
90.514	154.550	66.0	41
76.285	153.750	65.2	33
65.020	155.800	64.4	26
57.115	158.500	63.7	21
48.140	155.340	63.3	17
42.095	160.870	63.1	13
35.474	159.290	63.7	10
30.490	158.500	64.8	8.00
26.186	157.710	66.5	6.40
21.838	153.750	68.5	5.12
18.478	152.170	70.6	4.10
15.620	151.380	72.2	3.28
13.192	152.350	74.2	2.62
11.206	153.750	75.2	2.10
9.216	151.380	76.3	1.68
7.747	152.170	77.3	1.34
5.990	149.010	78.0	1.00
5.290	154.550	77.5	0.80
4.320	152.500	77.6	0.64
3.600	152.960	76.8	0.51
2.740	155.340	77.6	0.41
1.947	160.080	75.6	0.33
1.860	156.920	76.2	0.26
1.400	151.860	77.0	0.21

Table G.2: Measurement data for the d-axis operational impedance $Z_d(s)$.

Va (mA)	**Stdev. Va(μV)**	**Ia (mA)**	**Stdev. Ia (μA)**	**Phase (°)**	**Stdev. Phase (°)**	**Frequency(Hz)**
121.340	150.000	153.63	132.000	81.600	0.080	1000
101.570	92.000	157.61	0.000	82.000	0.080	800
81.000	127.000	155.63	36.000	82.500	0.100	640
65.200	0.000	153.66	0.000	82.600	0.100	512
52.600	35.000	154.64	0.000	83.300	0.100	410
42.300	80.000	154.71	250.000	83.400	0.200	328
34.400	114.000	156.65	370.000	83.600	0.200	262
27.500	100.000	155.34	0.000	83.300	0.200	210
22.200	80.000	156.16	160.000	82.700	0.300	168
17.700	75.000	156.12	50.000	81.700	0.300	134
13.200	78.000	155.33	78.000	80.200	0.400	100
10.800	80.000	157.71	0.000	78.600	0.400	80
8.800	57.000	158.50	0.000	76.200	0.600	64
7.200	11.000	159.26	145.000	73.500	0.100	51
5.760	50.000	155.34	0.000	70.400	0.200	41
4.500	10.000	156.13	0.000	66.600	0.200	33
4.020	17.000	155.37	200.000	61.600	0.300	26
3.430	13.000	155.34	0.000	57.000	0.200	21
3.020	15.000	156.83	200.000	51.800	0.200	17
2.600	30.000	157.71	0.000	45.200	0.800	13
2.300	15.000	155.34	0.000	38.500	0.600	10
2.100	28.000	156.13	0.000	33.800	0.700	8.00
2.060	23.000	156.13	0.000	28.600	0.400	6.40
1.940	22.000	155.34	0.000	24.700	0.600	5.12
1.890	38.000	155.34	0.000	22.700	0.600	4.53
1.880	11.000	155.34	0.000	21.100	0.300	4.05
1.840	10.000	153.75	0.000	19.900	0.400	3.61
1.830	12.000	155.34	0.000	18.700	0.300	3.23
1.800	26.000	155.23	300.000	17.400	0.300	2.88
1.800	10.000	155.99	300.000	16.600	0.300	2.57
1.760	10.000	154.84	380.000	15.700	0.300	2.30
1.710	17.000	154.55	0.000	15.500	0.600	2.05
1.700	10.000	153.75	0.000	14.200	0.300	1.83
1.650	22.000	154.55	0.000	14.000	0.300	1.63
1.650	16.000	154.10	550.000	13.400	0.500	1.46
1.630	11.000	154.55	0.000	12.900	0.500	1.30
1.640	10.000	156.13	0.000	12.400	0.500	1.16
1.590	7.000	153.57	336.000	10.900	0.100	1.00
1.560	13.000	154.30	970.000	10.200	0.200	0.89
1.590	16.000	159.00	410.000	0.400	0.400	0.80
1.500	10.000	154.55	0.000	10.000	0.450	0.71
1.460	14.000	150.59	0.000	9.700	0.500	0.64
1.480	8.000	153.75	0.000	9.200	0.200	0.57
1.430	10.000	149.00	620.000	7.900	0.300	0.51
1.450	8.000	152.96	0.000	7.600	0.400	0.45
1.440	10.000	152.80	1013.000	7.000	0.200	0.40
1.490	0.000	157.71	0.000	6.200	0.200	0.36
1.430	6.000	152.17	0.000	5.900	0.200	0.32
1.410	10.000	151.38	0.000	5.600	0.200	0.29
1.450	10.000	155.81	400.000	4.400	0.400	0.23
1.120	9.000	121.34	0.000	3.000	0.600	0.18
0.931	10.000	100.80	0.000	3.470	0.600	0.15
0.753	10.000	81.03	0.000	1.510	1.500	0.12
0.637	11.000	67.00	0.000	0.510	0.650	0.10

Table G.3: Measurement data for the q-axis operational impedance $Z_q(s)$.

Va (mA)	**Stdev. Va(μV)**	**Ia (mA)**	**Stdev. Ia (μA)**	**Phase (°)**	**Stdev. Phase (°)**	**Frequency(Hz)**
199.940	320.000	156.09	170.000	75.900	0.100	1000
163.540	160.000	156.13	0.000	77.300	0.100	800
130.920	120.000	153.89	300.000	78.500	0.130	640
107.210	38.000	155.33	40.000	79.600	0.070	512
88.142	30.000	156.12	46.000	80.500	0.090	410
72.332	0.000	158.49	57.000	80.700	0.090	328
56.522	0.000	155.97	306.000	81.400	0.200	262
45.720	160.000	156.46	392.000	81.800	0.150	210
36.810	88.000	156.10	150.000	81.700	0.190	168
29.560	70.000	156.21	220.000	81.300	0.210	134
22.320	100.000	157.02	300.000	80.500	0.260	100
17.890	57.000	156.87	165.000	79.500	0.290	80
14.260	57.000	155.23	245.000	78.300	0.370	64
11.470	86.000	154.55	0.000	76.800	0.510	51
9.380	55.000	155.34	0.000	75.000	0.390	41
7.800	60.000	155.34	0.000	72.300	0.560	33
6.460	21.000	156.92	0.000	69.300	0.180	26
5.420	21.000	156.89	146.000	66.500	0.190	21
4.500	11.800	157.69	96.000	63.500	0.270	17
3.760	10.600	156.13	0.000	58.800	0.320	13
3.170	24.000	156.90	118.000	54.500	0.600	10
2.760	11.000	156.92	0.000	50.500	0.290	8.00
2.420	10.000	156.13	0.000	46.100	0.360	6.40
2.140	10.000	156.13	0.000	41.900	0.360	5.12
2.040	36.000	156.92	0.000	39.700	0.520	4.53
1.950	10.000	156.92	0.000	37.200	0.220	4.05
1.850	10.000	155.34	0.000	34.400	0.150	3.61
1.790	10.000	156.13	0.000	32.000	0.260	3.23
1.710	17.000	155.71	400.000	29.900	0.440	2.88
1.690	9.000	156.13	0.000	27.500	0.500	2.57
1.580	14.000	150.59	0.000	25.300	0.450	2.30
1.610	7.000	156.13	0.000	22.800	0.260	2.05
1.590	19.000	156.13	0.000	20.900	0.520	1.83
1.520	44.000	156.13	0.000	19.500	1.400	1.63
1.500	32.000	156.92	200.000	17.900	0.800	1.46
1.490	8.000	156.13	0.000	15.900	0.300	1.30
1.470	8.000	154.49	600.000	14.200	0.700	1.16
1.460	12.000	155.34	0.000	13.100	0.710	1.01
1.440	25.000	155.34	0.000	11.700	0.520	0.90
1.430	11.000	156.92	0.000	11.000	0.630	0.81
1.410	19.000	156.13	0.000	9.600	0.550	0.72
1.420	15.000	155.07	427.000	8.100	0.470	0.64
1.410	16.000	153.36	1635.000	7.490	0.520	0.57
1.415	9.000	155.34	0.000	6.600	0.580	0.51
1.400	10.000	155.59	180.000	6.100	0.360	0.46
1.380	10.000	155.34	0.000	6.000	0.280	0.41
1.390	17.000	154.55	0.000	4.100	0.430	0.36
1.390	0.000	155.34	0.000	4.300	0.150	0.33
1.380	10.000	154.55	0.000	3.500	0.330	0.29
1.390	6.000	155.34	0.000	2.700	0.220	0.26
1.360	11.000	154.55	0.000	2.500	0.270	0.23

Table G.4: Additional test measurement data for the q-axis operational impedance $Z_q(s)$.

Va (mA)	**Stdev. Va(μV)**	**Ia (mA)**	**Stdev. Ia (μA)**	**Phase (°)**	**Stdev. Phase (°)**	**Frequency(Hz)**
197.130	0.000	153.57	262.000	76.000	0.150	1000
165.510	0.000	156.60	150.000	77.300	0.140	800
132.910	0.000	154.62	170.000	78.600	0.140	640
108.200	0.000	155.63	0.000	79.700	0.140	512
88.930	0.000	158.32	300.000	80.600	0.170	410
71.540	0.000	156.92	0.000	80.900	0.130	328
57.115	0.000	156.92	0.000	81.500	0.130	262
45.650	0.000	156.13	0.000	81.800	0.130	210
36.960	0.000	156.13	0.000	81.500	0.130	168
29.550	0.000	156.13	0.000	81.400	0.140	134
22.230	0.000	156.13	0.000	80.600	0.180	100
17.800	39.000	155.34	0.000	79.700	0.170	80
14.476	0.000	156.13	0.000	78.300	0.220	64
11.610	19.000	156.13	0.000	76.700	0.110	51
9.540	0.000	156.92	0.000	74.700	0.140	41
7.810	50.000	155.38	165.000	72.300	0.360	33
6.470	11.000	156.92	0.000	69.800	0.200	26
5.400	14.000	156.13	0.000	66.800	0.190	21
4.610	12.000	156.92	0.000	63.700	0.230	17
3.810	0.000	156.92	0.000	59.500	0.300	13
3.170	16.000	156.13	0.000	55.100	0.700	10
2.770	9.000	156.13	0.000	50.200	0.600	8.00
2.470	10.000	156.92	0.000	46.400	0.200	6.40
2.230	15.000	156.92	0.000	41.600	0.500	5.12
2.080	33.000	156.60	400.000	39.300	0.400	4.53
1.980	12.000	155.34	0.000	36.900	0.300	4.05
1.870	16.000	155.34	0.000	34.300	0.430	3.61
1.820	13.000	156.13	0.000	32.200	0.400	3.23
1.760	10.000	156.13	0.000	29.700	0.170	2.88
1.700	9.000	156.13	0.000	27.500	0.310	2.57
1.660	10.000	156.49	400.000	25.500	0.360	2.30
1.610	14.000	155.72	401.000	23.200	0.370	2.05
1.570	15.000	156.92	0.000	21.900	0.700	1.83
1.520	19.000	156.13	0.000	19.200	0.600	1.63
1.518	11.000	156.92	0.000	17.500	0.380	1.46
1.510	8.000	156.13	0.000	15.600	0.400	1.30
1.480	12.000	155.34	0.000	14.100	0.620	1.16
1.460	14.000	157.70	0.000	12.900	0.770	1.01
1.460	10.000	156.92	0.000	12.100	0.760	0.90
1.470	13.000	155.35	0.000	10.100	0.580	0.81
1.440	35.000	156.13	0.000	9.100	0.640	0.72
1.410	8.000	154.55	0.000	7.900	0.370	0.64
1.400	8.000	154.55	0.000	7.400	0.560	0.57
1.430	15.000	156.13	0.000	6.500	0.360	0.51
1.410	14.000	154.55	0.000	5.100	0.490	0.46
1.400	8.000	156.92	0.000	5.400	0.620	0.41
1.380	16.000	154.55	0.000	4.430	0.340	0.36
1.390	0.000	156.92	0.000	4.600	0.220	0.33
1.410	10.000	156.92	0.000	3.500	0.200	0.29
1.360	10.000	156.13	0.000	3.000	0.200	0.26
1.350	13.000	154.55	0.000	2.700	0.340	0.23

Table G.5: Measurement data for $sG(s)$.

Ia (mA)	**Stdev. Ia (mA)**	**Ifd (mA)**	**Stdev. Ifd (μA)**	**Phase (°)**	**Stdev. Phase (°)**	**Frequency(Hz)**
154.700	0.900	6.75	31.00	-0.200	0.600	1000
158.100	1.400	6.89	8.00	0.500	0.600	800
155.500	1.200	6.82	6.00	1.200	0.500	640
160.900	1.100	6.97	12.00	1.900	0.500	512
156.600	1.700	6.75	17.00	2.500	0.600	410
156.300	1.000	6.66	7.00	4.000	0.900	328
156.300	0.800	6.80	12.00	4.400	0.300	262
155.500	0.700	6.46	16.00	5.500	0.400	210
151.800	0.800	6.28	19.00	6.700	0.400	168
158.500	1.100	6.43	17.00	7.600	0.400	134
158.500	0.600	6.30	15.00	9.100	0.300	100
155.200	0.500	6.02	19.00	11.200	0.160	80
153.400	0.500	5.76	17.00	13.500	0.200	64
160.300	0.400	5.85	19.00	15.200	0.200	51
154.600	0.600	5.45	19.00	17.800	0.250	41
157.900	0.800	5.37	20.00	20.300	0.230	33
158.100	1.200	5.00	17.00	23.600	0.440	26
159.500	0.400	4.86	17.00	25.500	0.200	21
157.700	0.400	4.45	12.00	29.100	0.200	17
159.500	0.500	4.21	11.00	31.800	0.200	13
158.600	0.250	3.77	9.00	35.600	0.200	10
156.700	0.300	3.39	13.00	39.100	0.140	8.00
155.100	0.500	3.00	15.00	42.900	0.130	6.40
155.200	0.400	2.68	13.00	46.400	0.130	5.12
129.850	0.350	2.18	38.00	49.100	0.300	4.10
125.700	0.550	1.77	0.00	53.700	0.200	3.28
126.700	0.350	1.60	9.00	57.400	0.300	2.62
119.700	0.400	1.28	18.00	62.500	0.340	2.10
93.600	0.200	0.83	9.00	66.100	0.500	1.68
89.000	0.300	0.66	10.00	70.100	0.600	1.34
85.200	0.400	0.51	9.00	72.400	0.600	1.00
82.100	0.400	0.42	15.00	75.000	1.300	0.80
80.650	0.272	0.35	6.00	75.800	1.800	0.64
83.500	0.200	0.31	8.00	75.500	0.600	0.51
72.300	0.500	0.27	22.00	74.400	2.400	0.41
69.460	0.400	0.22	16.00	73.300	2.400	0.33
67.300	0.180	0.19	17.00	78.000	3.700	0.26